

Evolution of {001} Texture in Non Heat Treatable  
Wrought Aluminum Alloys by Hot Working

(非熱処理型展伸用アルミニウム合金の高温加工による  
{001}集合組織の付与)

March 2011

Yokohama National University  
Department of Solid State Materials and Engineering

**Hyeon-Mook JEONG**

# CONTENTS

## Chapter 1 Introduction

1.1 Background and motivation .....	2
1.2 Deformation mechanisms of Al–Mg alloys at high temperatures .....	4
1.3 Texture formation in binary Al–Mg alloys by high-temperature deformation .....	7
1.4 Objectives and outline .....	11
References .....	13

## Chapter 2 Experimental Procedure

2.1 Materials and heat treatment .....	16
2.2 High temperature deformation .....	16
2.2.1 Uniaxial compression .....	16
2.2.2 Plane strain compression .....	17
2.3 Microstructure observation and texture measurement .....	18
2.4 Crystal orientation measurement by EBSD technique .....	20
2.5 Evaluation of bendability .....	21
Reference .....	21

## Chapter 3 Texture Evolution of AA5182 Alloy during High Temperature Deformation

3.1 Introduction .....	23
3.2 Experimental procedure .....	24
3.3 Results .....	24
3.3.1 Initial microstructures .....	24
3.3.2 Stress–strain curves .....	25
3.3.3 Characteristics of texture .....	27
3.3.4 Grain structure maps .....	39
3.4 Discussion .....	33
3.4.1 Comparison of the textures formed in Al–5mass%Mg and AA5182 .....	33
3.4.2 Effect of deformation conditions on texture formation .....	35
3.4.3 {001} texture map .....	36
3.4.4 Deformation mechanism at high temperatures .....	38
3.5 Conclusions .....	40
References .....	41

## Chapter 4 Texture Formation in AA5052 Alloy under Uniaxial Compression at High Temperatures

4.1 Introduction .....	43
4.2 Experimental procedure .....	43
4.3 Results .....	46
4.3.1 Stress–strain curves .....	46
4.3.2 Texture formation .....	46
4.3.3 Grain structures .....	51
4.4 Discussion .....	55
4.4.1 Texture formation process in AA5052 alloys .....	55
4.4.2 Development of {001} texture .....	56
4.4.3 {001} texture maps of AA5052 and AA5182 alloys .....	57
4.5 Conclusions .....	60
References .....	61

Chapter 5	Effect of Texture on the Bending Workability of AA5182 Alloy	
5.1	Introduction	63
5.2	Experimental procedure	63
5.3	Results	64
5.3.1	Stress–strain curves	64
5.3.2	Texture formation	65
5.3.3	Grain structure maps	68
5.3.4	Microstructures of the bent surfaces	72
5.4	Discussion	75
5.4.1	Relationship between texture and bend workability	75
5.4.2	Effect of grain structure on bendability	76
5.5	Conclusions	77
	References	78
Chapter 6	Conclusions	80
	References	82
Appendix A:	Classification of commercial Aluminum Alloys	84
Acknowledgements		89

## Abstract

In this work, methods of controlling the texture in commercial aluminum alloys were experimentally investigated by compressive deformation at high temperatures. The non heat treatable wrought commercial aluminum alloys AA5052 and AA5182 were examined at high temperatures under various deformation conditions. On the basis of the results, the thesis discusses ways of improving the bending workability by controlling the texture.

# Chapter 1

## Introduction

### 1.1 Background and motivation

Although it costs 10 times as much to prepare primary aluminum as it does to prepare iron, aluminum-based materials are the second most widely used metallic materials. For structural applications in mechanical engineering, aluminum alloys offer an excellent combination of intrinsically good corrosion and oxidation resistance and high specific strength compared with stainless steels. However, the workability of aluminum alloy sheets must be improved because they have lower  $r$  values and ductility than cold rolled steel sheets.

Aluminum alloys are divided roughly into two groups: casting alloys and wrought alloys. Aluminum wrought alloy products are formed by hot and cold deformation. The typical deformation processes are hot and cold rolling, drawing, forging, and extrusion. Commercial wrought aluminum alloys are identified by four-digit numbers, 2xxx – 8xxx, where the last two digits are the alloy identifier. The classification and characteristics of commercial wrought aluminum alloys are described in appendix A.

Commercial aluminum alloys have recently attracted interest in the automotive industry for car body sheet applications. Consequently, the microstructural changes that occur in these alloys during thermomechanical processing are of increasing commercial and academic interest. Among the commercial wrought aluminum alloys, the 5xxx series, in which Mg is the major alloying element, have been used for inner components of automobiles and ships that require high strength and corrosion resistance [1]. The strength of 5xxx series alloys is controlled primarily by a combination of solid solution hardening caused by Mg atoms and grain size strengthening. Figure 1.1 shows the effect of Mg in solution on the tensile properties of annealed high purity aluminum sheets [2]. Both yield strength and ultimate tensile strength increase with increasing Mg concentration, whereas the elongation drops sharply with even small Mg additions. Similar behavior with increasing Mg concentration is observed in the tensile properties of commercial alloys.

# 1. Introduction

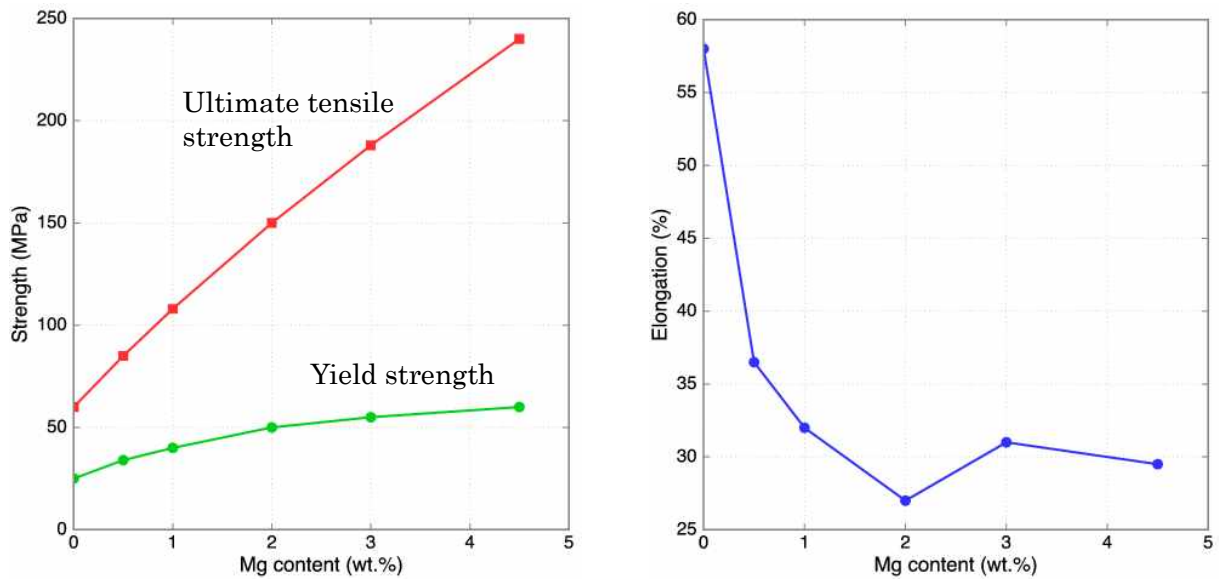


Fig. 1.1 Effect of Mg in solution on tensile properties of annealed Al–Mg binary alloys [2].

The Mg concentration in commercial 5xxx alloys ranges from 0.5 to about 6 wt%. Alloys with low Mg concentrations are used where formability or surface finishing are critical. The good formability of Al–Mg alloys is attributable to the high strain hardening rate, which contributes to the high forming strains achieved with these alloys. Higher-Mg alloys are used in structural applications where strength, fracture and fatigue resistance, and welding ability are important.

More bendable aluminum sheets have recently become desirable for automotive body sheets and/or inner parts. Improving the plastic workability of aluminum sheets is a key issue for promoting the application of aluminum alloys in a wide range of fields. The effect of texture has been widely discussed in terms of the plastic workability of aluminum alloys [3].

Texture is a structure consisting of crystal grains with preferred orientations. Plastic deformation, recrystallization, and phase transformation frequently cause texture to form. Formable aluminum alloys are obtained by controlling the texture by choosing appropriate production



## 1. Introduction

---

processes. For example,  $\{111\}$  texture improves the deep drawability of sheets [4], and the formation of  $\{001\}$  texture should be suppressed to avoid earing during deep drawing [5,6]. Earing of sheet material is well known and is possibly the most significant type of defect. It has been suggested that the development of cube texture on the surface of a sheet might increase the limit angle for bending [7]. Therefore, the control of texture is important for practical application of aluminum alloys.

This thesis discusses two aspects of AA5052 and AA5182 commercial aluminum alloys: the control of texture during high temperature deformation and the effect of texture on the bendability. To understand the formation of texture by high temperature deformation of commercial AA5052 and AA5182 aluminum alloys, it is necessary to investigate the behavior of texture formation in binary Al–Mg alloys. Moreover, understanding the mechanism of texture formation can also facilitate the development of processes for texture control. Hence, the mechanism of texture formation for binary Al–Mg alloys is described in the next section.

### 1.2 Deformation mechanisms of Al–Mg alloys at high temperatures

The first detailed studies of the high temperature deformation mechanism in Al–Mg alloys were conducted by Horiuchi et al. [8-10]. They observed a high temperature yielding phenomenon with certain strain rates for binary Al–Mg alloys (Mg content = 1.1, 3.3, and 5.5 at%). They discussed the high temperature deformation mechanism in solid solution alloys using creep experiments.

In solid solution hardening-type alloys, dislocations are also known to move with the Cottrell atmosphere in a certain range of high temperature deformation conditions, a phenomenon called atmosphere dragging [24]. That is, the deformation mechanism depends on the deformation conditions. As a result, the deformation texture changes depending on the strain. The deformation texture will be discussed in section 1.3.

The creep rate at constant stress usually increases exponentially with temperature [12,13]; therefore, it is convenient to plot  $\ln \dot{\epsilon}$  against  $1/T$ , thus fitting the creep rate to an Arrhenius-type law,

## 1. Introduction

---

$$\dot{\epsilon} \propto \exp\left(-\frac{Q}{RT}\right) \quad (1.1)$$

where  $Q$ , which is proportional to the slope of the  $\ln \dot{\epsilon}$  versus  $1/T$  relationship, is the apparent activation energy of creep. The creep rate increases with an increase in applied stress  $\sigma$ , and  $\ln \dot{\epsilon}$  is typically plotted against  $\ln \sigma$  in the hope of obtaining a straight line by using the log scale plot. When this happens, which it usually does if the stress interval is small enough, the creep rate depends on the stress by a power law  $\dot{\epsilon} \approx \sigma^n$ ;  $n$  is the stress exponent. The empirical equation of state can then be written:

$$\dot{\epsilon} = \dot{\epsilon}_0 \sigma^n \exp\left(-\frac{Q}{RT}\right) \quad (1.2)$$

Dorn [14] proposed equation (1.2) for creep.

The deformation mechanisms in binary Al–Mg alloys vary with the deformation temperature ( $T$ ) and strain rate ( $\dot{\epsilon}$ ) in addition to the strain ( $\epsilon$ ). The strain rate and deformation temperature are often incorporated into a single parameter, the Zener–Hollomon parameter ( $Z$ ).

Zener and Hollomon [15] suggested the parameter

$$Z = \dot{\epsilon} \exp\left(-\frac{Q}{RT}\right) \quad (1.3)$$

to investigate the strain rate dependence of the stress in constant strain rate tensile experiments;  $Z$  has been widely used to investigate the stress dependence of the creep rate in experiments at various temperatures. It is well established experimentally that two distinct types of creep behavior occur in metallic solid solution alloys.

The first type is similar to the creep behavior of pure metals (hereafter referred to as class II). The second type is never observed in pure metals and has distinct, identifiable characteristics associated only with solid solution alloys (class I). Sherby and Burke [16] and Cannon and Sherby [17] proposed dividing the creep behavior of solid solution alloys at high temperatures into two categories on the basis of certain characteristic behaviors.

## 1. Introduction

- Class I alloys exhibit:
  - a power-law dependence on stress with  $n \approx 3$ ,
  - little or no primary creep,
  - no dependence on the stacking fault energy, and
  - little or no formation of subgrains during creep.
- Class II alloys exhibit:
  - a power-law dependence on stress with  $n \approx 5$ ,
  - normal primary creep,
  - a dependence on the stacking fault energy, and
  - creep polygonization.

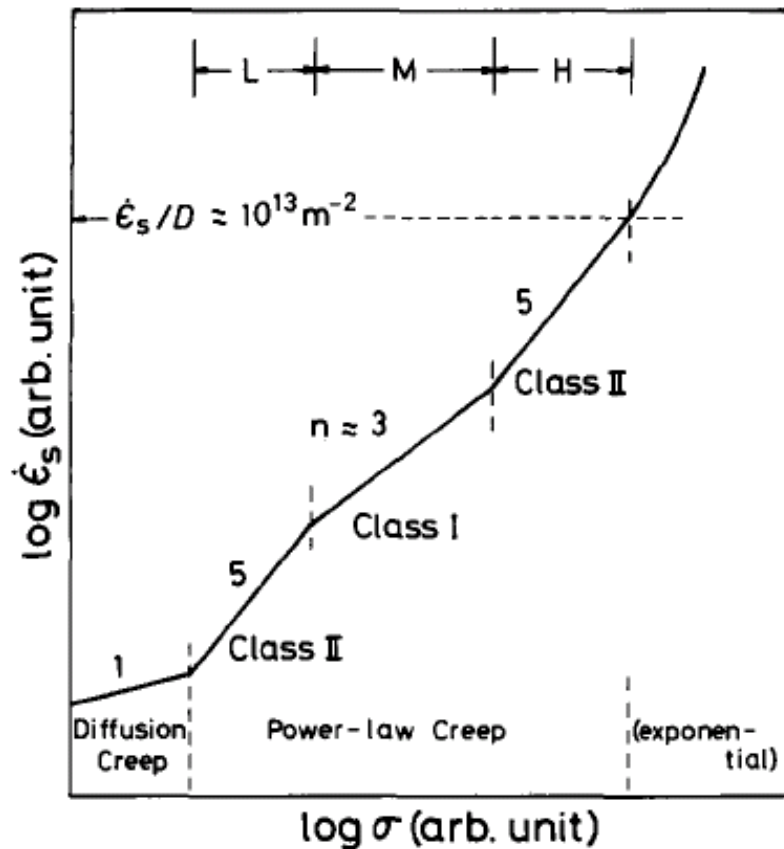


Fig. 1.2 Schematic illustration of the relationship between steady state creep rate  $\dot{\epsilon}$  and stress  $\sigma$  in solid solution alloys [19].

## 1. Introduction

---

These deformation mechanisms are also discussed by Yavari et al. on the basis of studies of Al–5%Mg solid solution alloy at high temperatures [18]. Figure 1.2 shows a schematic view of the change in stress exponential [19]. They summarized the behavior of the alloy as follows: At very low stress levels, diffusional creep may dominate; in the low-stress range (region L in the figure),  $n = 5$ , and class II creep dominates; in the intermediate stress range (region M),  $n = 3$  and class I creep dominates; in the high stress range (region H),  $n = 5$  and class II creep dominates again; in the extremely high stress range, the power law breaks down, and  $\dot{\epsilon}$  changes as an exponential function of the stress. When the steady-state creep rate  $\dot{\epsilon}$  is analyzed as a power function of the applied stress  $\sigma$ , the stress exponent  $n$  is close to 3 in class I behavior, in which the rate-controlling process is the viscous glide of dislocations accompanied by the solute atmosphere. In class II behavior,  $n$  is about 5, and the rate-controlling process is a recovery process, including climbing of edge dislocations or jogs [20]. These behaviors of class I or II creep depend on the creep conditions [21].

The next section discusses the relationship between deformation conditions and texture formation in binary Al–Mg alloys at high temperatures.

### 1.3 Texture formation in binary Al–Mg alloys by high temperature deformation

Aluminum alloys are a crystalline material with a rather high stacking fault energy (SFE, 170 mJ/m<sup>2</sup>) [22], so their plastic deformation occurs mainly by dislocation slips in the lattice structure. Under the critical resolved shear stress (CRSS,  $7.9 \times 10^5$  N/m<sup>2</sup>) [23] on a definite crystallographic plane (slip plane), dislocation slip will begin. A slip system consists of a slip plane and a slip direction; in aluminum and its alloys, the slip plane is the  $\{111\}$  plane, and the slip direction is the  $\langle 011 \rangle$  direction.

Different slip systems on several slip planes are very often activated simultaneously during cold deformation, which results in multi-slip

## 1. Introduction

---

dislocations. The deformation-induced increase in the density of vacancies, dislocations, and grain boundaries provides obstacles to further movement of dislocations and leads to work hardening of deformed aluminum alloys.

For rate-independent materials, the single-crystal yield surfaces reveal sharp corners where two or more slip systems are activated simultaneously. For most materials, the rate sensitivity ( $m$ ) is not zero, so the yield surfaces become rounded [28]. The dependence of the resulting polycrystal plasticity on the actual rate sensitivity is quite insignificant if  $m$  is small (less than about 0.05). However, in high rate sensitivity materials, the yield surfaces become so rounded that slip will be much more equally partitioned between the slip systems, and the lattice rotations differ [29]. In these circumstances, texture development favoring one component may be obtained [30], and the effect of rate sensitivity may not appear. However, for rolling or tension, more texture components are observed. Thus, if the rate sensitivity is high, one component may develop sooner and become stronger than the others.

The strain rate sensitivity generally increases with increasing temperature. However, it is low ( $m < 0.03$ ) for most pure metals and alloys, except for some alloys in which solute drag dominates the deformation kinetics, where  $m > 0.2$ . Experimental results reported by Horiuchi et al. [9-11] for Al-Mg alloys indicate that the stress exponent  $n$  is equal to 3; that is, this alloy has high rate sensitivity. Furthermore, in their tensile tests of Al-Mg single crystals at elevated temperature, they found that the lattice rotation did not agree with predictions based on the assumption of single slip. Figure 1.3 shows an analysis of Al-3at%Mg single crystals elongated at 632 K [27]. The orientation of the tensile axis was measured at various strains. The results of room temperature tests agreed with the lattice rotation calculated assuming single slip. In contrast, in high temperature tests, the orientation of the tensile axis rotated in accordance with predictions assuming multiple slip.

The {001} plane, which is the stable orientation of binary Al-Mg alloys, was reported by Horiuchi and Otsuka [10] in 1972 for specimens with various orientations in tensile creep tests where the viscous motion of dislocations dominated the deformation.

# 1. Introduction

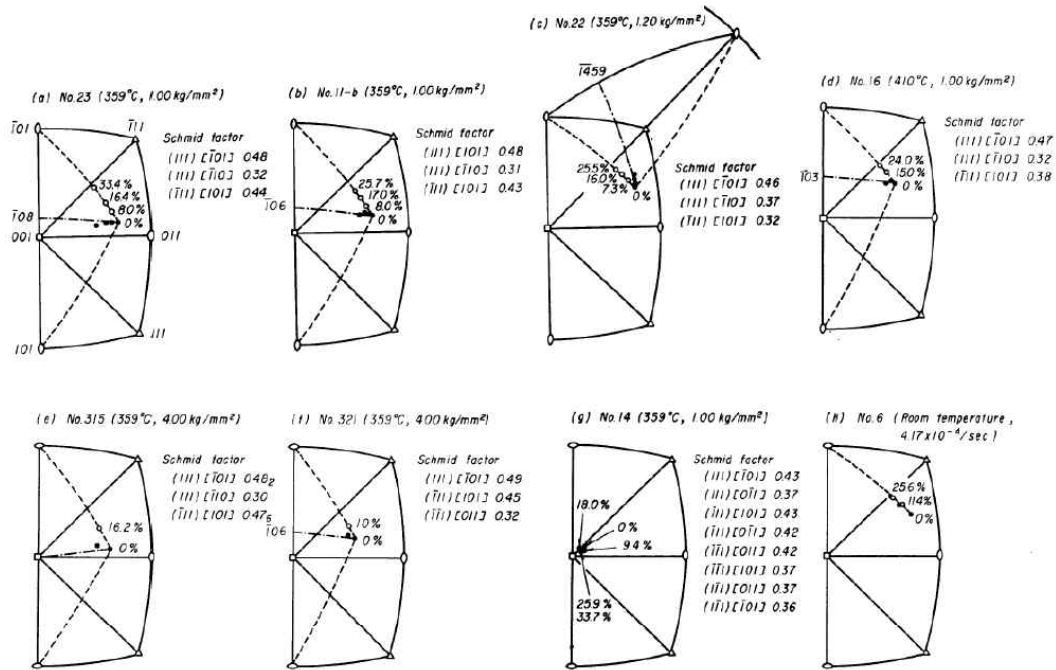


Fig. 1.3 Stereographic projections showing rotation of tension axis in Al-3at%Mg alloys (solid circles, measured at the stated amount of extension; open circles, calculation based on a single slip; direction of tension axis rotation estimated assuming double glide) [27].

Okayasu and Fukutomi [25,26] investigated the behavior of compression deformation and texture formation in an Al-3mass%Mg solid solution at high temperatures. Texture measurement revealed that the main component of the fiber texture changed from {011} (the compression plane) to {011} + {001} and to {001} with increasing strain when the viscous motion of dislocations was the dominant deformation mechanism. These results suggest that grain boundary migration contributes to the formation of {001} fiber texture.

Okayasu and Fukutomi [25] also investigated lattice rotation in Al-3mol%Mg single crystals by compression tests in which the viscous motion of dislocations was the dominant deformation mechanism. In single crystals with initial orientations far from {001}, the amount of lattice rotation was larger than that for orientations close to {001}. The direction of

## 1. Introduction

the lattice rotation coincided with expectation based on single slip of the  $\{111\}\langle 110 \rangle$  system. The amount of lattice rotation was quite small when the initial orientations were close to  $\{001\}$ , which coincides with the result found by Otsuka and Horiuchi [27]. These findings suggest that the  $\{001\}$  orientation is stable against uniaxial deformation.

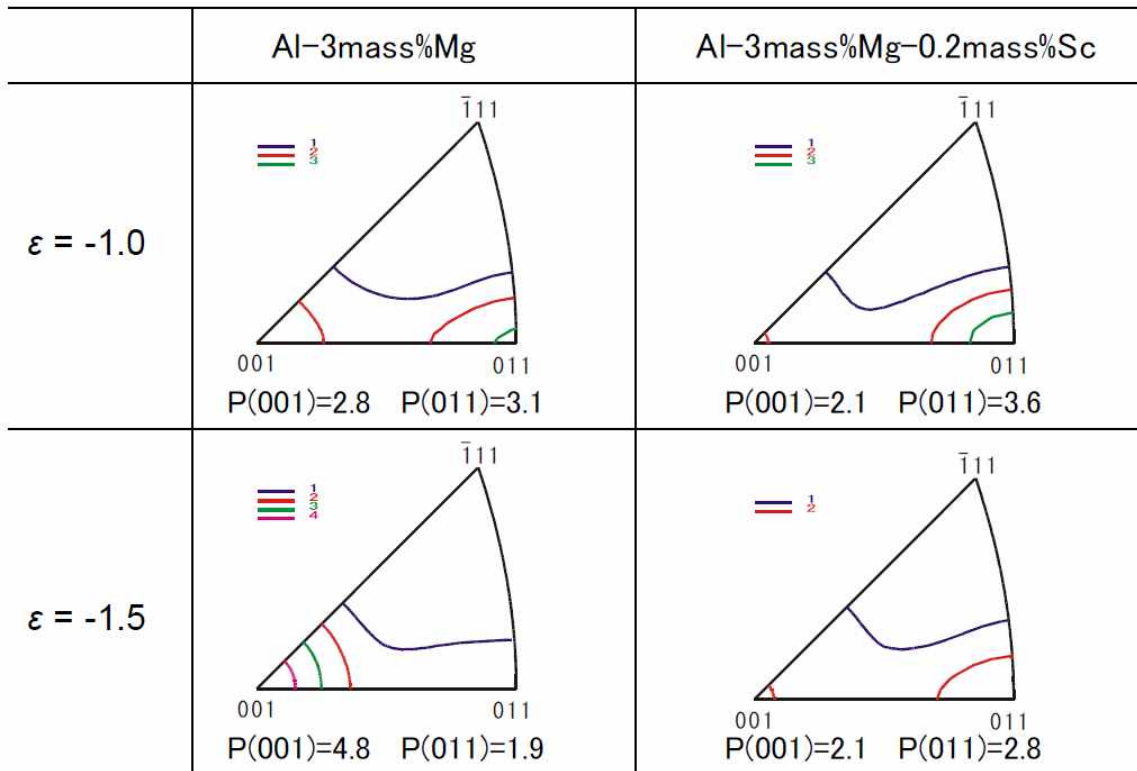


Fig. 1.4 Inverse pole figures for specimens compressed at 723 K up to a true strain of  $-1.0$  and  $-1.5$  under a strain rate of  $5.0 \times 10^{-4} \text{ s}^{-1}$ . Contour lines represent intervals in units of average pole density.  $P(001)$  and  $P(011)$  are the pole densities at  $(001)$  and  $(011)$ , respectively.

Figure 1.4 shows the inverse pole figures for specimens deformed at 723 K up to strains of  $-1.0$  and  $-1.5$  under a strain rate of  $5.0 \times 10^{-4} \text{ s}^{-1}$ . Figures on the left and right show the results for Al-3Mg and Al-3Mg-0.2Sc, respectively. Compared to the pole densities at  $(001)$  and  $(011)$ , the  $\{001\}$  pole

## 1. Introduction

---

density for Al–3Mg–0.2Sc alloy decreases and that of Al–3Mg alloy increases with increasing strain. A weak but obvious peak in the pole density at (001) of Al–3Mg–0.2Sc also appears, suggesting that grains with {001} orientations remained after a large amount of deformation owing to their stability.

On the basis of these results, this thesis attempts to clarify the deformation mechanism of {001} texture in practical aluminum alloys. The predicted grain boundary migration suppression in 5xxx series aluminum alloys compared to that in binary Al–Mg alloy has been experimentally investigated by examining the development of {001} texture over a wide range of temperatures and strain rates. The effect of texture on bend workability is also investigated using the AA5182 aluminum alloy.

### 1.4 Objectives and outline

The present research has two main targets. One is to understand texture formation in commercial aluminum alloys during high temperature deformation. The other is to clarify the effect of texture on the bending workability of the alloys.

Texture-formation during high temperature deformation of non-heat-treatable wrought aluminum alloys (AA5052 and AA5182) is described in chapters 3 and 4. The relationship between the cube texture and bendability of AA5182 alloy is presented in chapter 5.

The chapters are outlined in more detail below.

In chapter 2, “Experimental procedure,” the experimental method is described. The procedures for specimen preparation and high temperature compressive deformation tests are explained. Methods of evaluating the texture are also explained in detail.

In chapter 3, “Texture evolution of AA5182 alloy during high temperature deformation,” texture formation under uniaxial compressive deformation of AA5182 alloy at high temperatures is described. To clarify the relationship between the high temperature deformation conditions and texture



## 1. Introduction

---

development, an  $\{001\}$  texture map is constructed that illustrates the effects of deformation temperature and strain rate on the development of the  $\{001\}$  component.

In chapter 4, “Texture formation of AA5052 alloy under uniaxial compression at high temperatures,” the relationship between the solute concentration and texture formation in commercial aluminum alloys is investigated at high temperatures. The characteristics of texture formation are also represented in the  $\{001\}$  texture map.

In chapter 5, “Effect of texture on the bending workability of AA5182 alloy,” the effect of texture on the bendability of AA5182 aluminum alloy is experimentally investigated.

Finally, the main results are summarized in chapter 6, “Conclusions.”

### References

- [1] T. Uno: *Sumitomo Light Metal Technical Reports*, **42** (2001) p. 100.
- [2] R. E. Sanders, Jr., S. F. Baumann and H. C. Stumpf: “Wrought Non-Heat-Treatable Aluminum Alloys,” *Treatise on Materials Science and Technology, Academic Press* **31** (1989) pp. 65–105.
- [3] S. Ikawa, M. Asano and S. Hirano: *Abstracts of the 116th Annual Meeting of the Japan Institute of Light Metals* (2009) pp. 301–302.
- [4] N. Yoshinaga, N. Sugiura, S. Hiwatashi, K. Ushioda and O. Kada: *ISIJ Int.* **48** (2008) pp. 667–670.
- [5] C-Y. Chen, J-C. Kuo, H-L. Chen and W-S. Hwang: *Mater. Trans.* **47** (2006) pp. 2434–2443.
- [6] H. Inoue and T. Takasugi: *Mater. Trans.* **48** (2007) pp. 2014–2022.
- [7] H. Takeda, A. Hibino and K. Takata: *Mater. Trans.* **51** (2010) pp. 614–619.
- [8] R. Horiuchi, H. Yoshinaga and S. Hama: *Trans. Japan Inst. Metals* **6** (1965) pp. 123–130.
- [9] R. Horiuchi and H. Yoshinaga: *Trans. Japan Inst. Metals* **6** (1965) pp. 131–139.
- [10] R. Horiuchi and M. Otsuka: *Trans. Japan Inst. Metals* **13** (1972) pp. 284–293.
- [11] R. Horiuchi: *Proc. First Korea-Japan Joint Symp. on Recent Adv. Mater. Sci. Engng.*, Seoul (Korea) (1978) pp. 143–165.
- [12] E. N. da C. Andrade: “On the viscous flow in metals and allied phenomena,” *Proc. Roy. Soc. London*, **A.84** (1910) pp. 1–12.
- [13] E. N. da C. Andrade: “The flow of metals under large constant stresses,” *Proc. Roy. Soc. London*, **A.90** (1914) pp. 329–342.
- [14] J. E. Dorn: “Some fundamental experiments on high temperature creep and fracture of metals at high temperatures,” *NPL Symposium*, HMSO, London, (1954) pp. 89–138.
- [15] C. Zener and J. H. Hollomon: “Effect of strain rate upon plastic flow of steel,” *J. Appl. Phys.* **15** (1944) pp. 22–32.
- [16] O. D. Sherby and P. M. Burke: “Mechanical behavior of crystalline solid at elevated temperature,” *Prog. Mater. Sci.* **13** (1968) pp. 325–390.

## 1. Introduction

---

- [17] W. R. Cannon and O. D. Sherby: "High temperature creep behaviour of class I and class II solid solution alloys," *Metall. Trans.* **1** (1970a) pp. 1030–1032.
- [18] P. Yavari, F. A. Mohamed and T. G. Langdon: "Creep and substructure formation in an Al-5%Mg solid solution alloy," *Acta Metall.* **29** (1981) pp. 1495–1507.
- [19] P. Yavari and T. G. Langdon: "An examination of the breakdown in creep by viscous glide in solid solution alloys at high stress levels," *Acta Metall.* **30** (1982) pp. 2181–2196.
- [20] S. Karashima: "Recent studies on mechanisms of high temperature creep of metals," *Tetsu to Hagane* **65** (1979) pp. 820–830.
- [21] F. A. Mohamed and T. G. Langdon: "The transition from dislocation climb to viscous glide in creep of solid solution alloys," *Acta Metall.* **22** (1974) pp. 779–788.
- [22] E. Hornbogen and H. Warlimont: *Metallkunde*, Springer Verlag, Berlin (1991) pp. 60–62.
- [23] J. D. Verhoeven: *Fundamentals of Physical Metallurgy*, John Wiley and Sons Inc., New York (1975) pp. 60–74 and 325–329.
- [24] A. H. Cottrell and M. A. Jaswon: *Proc. Roy. Soc. A.* **199** (1949) pp. 104–114.
- [25] K. Okayasu and H. Fukutomi: *Mater. Sci. Forum* **495–497** (2005) pp. 579–584.
- [26] K. Okayasu and H. Fukutomi: *J. Japan Inst. Metals* **70** (2006) pp. 562–567.
- [27] M. Otsuka and R. Horiuchi: *J. Japan Inst. Metals* **36** (1972) pp. 809–817.
- [28] U. F. Kocks: "Constitutive behavior based on crystal plasticity," *Unified Constitutive Equations for Creep and Plasticity* (edited by A. K. Miller), Elsevier, (1987) pp. 1–88.
- [29] G. R. Canova, C. Fressengeas, A. Molinari and U. F. Kocks: "Effect of rate sensitivity on slip system activity and lattice rotation," *Acta Metall.* **36** (1988) pp. 1961–1970.
- [30] C. S. Barret and L. H. Levenson: "The structure of aluminum after compression," *Trans. Am. Inst. Min. Engrs.* **137** (1940) pp. 112–127.

## Chapter 2

### Experimental Procedure

## 2. Experimental Procedure

---

### 2.1 Materials and heat treatment

AA5182 and AA5052 aluminum alloys were provided by Furukawa-Sky Aluminum Corp. and Nippon Light Metal Co., Ltd., respectively. AA5182 alloy was obtained in the form of 70% hot rolled plate 20 mm thick. AA5052 alloy was also supplied as hot rolled plate 20 mm thick. The chemical compositions of both alloys are given in Table 2.1.

The AA5052 alloy was annealed at 853 K for 10 min and 100 min in air. The AA5182 alloy was annealed at temperatures of 823–843 K for 10 min, 100 min, or 1000 min. In all cases, to keep the elements in solid solution, the specimens were quenched in water from the solution treatment temperature after annealing.

Table 2.1 Chemical composition of AA5052 and AA5182 aluminum alloys in the present study (mass%).

	Mg	Fe	Cr	Mn	Si	Cu	Zn	Ti	Al
AA5052	2.58	0.28	0.18	0.01	0.08	0.01	0.01	0.02	bal.
AA5182	4.54	0.30	0.04	0.45	0.12	0.09	—	0.04	bal.

### 2.2 High temperature deformation

#### 2.2.1 Uniaxial compression

Cylindrical specimens were prepared by spark erosion machining for compression testing. The aspect ratio of the specimens was maintained at 1.5 for all specimen sizes. Uniaxial compression tests were conducted by an Autograph DCS-2000 device with a loading capacity of 2000 kg. A schematic view of the uniaxial compression test is shown in Fig. 2.1. The tests were conducted under a constant cross-head speed in air at temperatures of 673K, 723K, 773K, and 823K and strain rates of  $5.0 \times 10^{-4}$ ,  $5.0 \times 10^{-3}$ , and  $5.0 \times$

## 2. Experimental Procedure

---

$10^{-2}\text{s}^{-1}$ . The final strain was evaluated on the basis of the cross-head speed and specimen height. An infrared ray furnace was used for heating. Specimens were kept for 1 h at the test temperature before deformation to decrease the effect of thermal expansion during deformation. After deformation, the furnace was immediately opened and the power supply was simultaneously switched off, and then the specimens were quenched in water to prevent changes in microstructure after the high-temperature compression test.

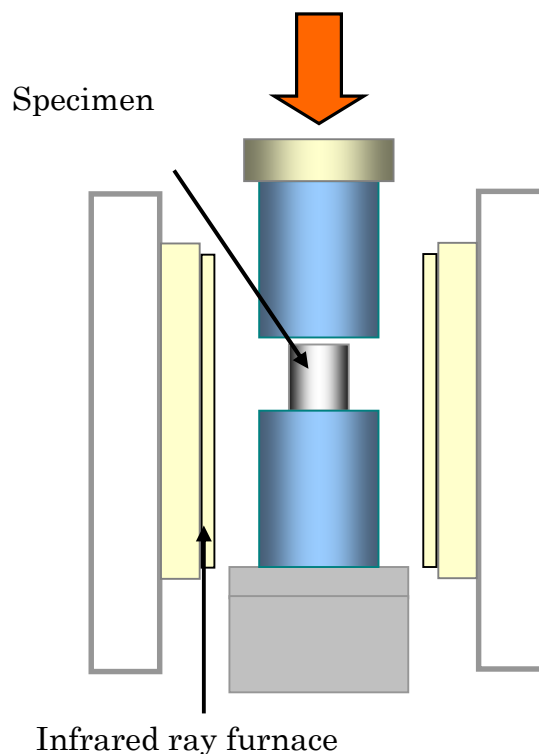


Fig. 2.1 Schematic view of testing device for uniaxial compression test.

### 2.2.2 Plane strain compression

Rectangular specimens with dimensions of  $15 \times 15 \times 10$  mm for use in plane compression tests were produced by spark erosion machining. Plane strain compression tests were conducted under a constant cross-head speed at 823 K in air up to true strains of  $-0.6$ ,  $-1.0$ , and  $-1.3$ . The strain rates

## 2. Experimental Procedure

---

were  $5.0 \times 10^{-3} \text{ s}^{-1}$  and  $5.0 \times 10^{-4} \text{ s}^{-1}$ . An infrared ray furnace was used for heating. Immediately after deformation, the infrared ray furnace was opened, and the power supply was simultaneously switched off. Then, the specimens were quickly quenched in water to avoid changes in microstructure after deformation.

### 2.3 Microstructure observation and texture measurement

Specimens for microstructure examination were mechanically polished using emery paper. To remove greasy contaminants on the aluminum surfaces, electrolytic polishing was performed under the conditions given in Table 2.2.

Table 2.2 Electrolytic polishing conditions for microstructure examination of aluminum alloys.

	Polishing solution	Procedure
AA5052 AA5182	methanol:ethylene glycol : $\text{HClO}_4 = 7:2:1$	Immerse specimen for 10 min, rinse in cold water, dry. $0^\circ\text{C}$ , 2 A

The texture on the compression plane was measured by the Schulz reflection method using nickel-filtered Cu K $\alpha$  radiation. The other measurement conditions are summarized in Table 2.3. Three pole figures were constructed for each measurement, using the diffracted X-ray intensities measured on the 111, 200, and 220 reflections. The diffraction intensity, except for that at the middle point, changes in strength with a change in the  $\alpha$  angle, since the length of the X-ray route varies except at the middle point. To correct the diffraction intensity, the collection factor of pure aluminum, as shown in Table 2.4, was applied.

Based on the {001}, {011}, and {111} pole figures, the orientation distribution function (ODF) was calculated by the Dahms–Bunge method [1]. The main component and sharpness of the texture were evaluated by examining inverse pole figures derived from the ODF calculation.

## 2. Experimental Procedure

---

Table 2.3 Conditions for texture measurement in aluminum

X-ray detector	Scintillation counter
X-rays	Cu K $\alpha$
Accelerating voltage, current	40 kV, 20 mA
$\alpha$ angle, step	0–75°, 5°
$\beta$ angle, step	0–355°, 5°
$\gamma$ oscillation	0 mm
Fixed time	4 s: 111, 200, 220
Divergence slit	1°
Scattering slit	8 mm + Ni filter
Receiving slit	7 mm
Schulz slit	1 mm

Table 2.4 Correction factor for each pole figure (pure aluminum).

$\alpha$ / deg.	111	200	220
15	1.831	1.774	1.455
20	1.403	1.468	1.192
25	1.166	1.297	1.091
30	1.078	1.233	1.078
35	1.049	1.181	1.068
40	1.037	1.161	1.050
45	1.024	1.146	1.050
50	1.000	1.113	1.050
55	1.000	1.100	1.050
60	1.000	1.050	1.020
65	1.000	1.000	1.000
70	1.000	1.000	1.000
75	1.000	1.000	1.000
80	1.000	1.000	1.000
85	1.000	1.000	1.000
90	1.000	1.000	1.000



## 2. Experimental Procedure

### 2.4 Crystal orientation measurement by EBSD technique

To confirm the local crystal orientation of both alloys, grain structure maps were constructed by the electron back-scattered diffraction (EBSD) technique. The local crystal orientations were measured by a JEOL JSM-5600 scanning electron microscope equipped with an EBSD system. A schematic view of the EBSD system is shown in Fig. 2.2. Regions were scanned using the beam control option with a scan step of 4  $\mu\text{m}$ . When the minimum rotation angle  $\theta$  between neighboring measurement points was larger than  $15^\circ$ , high-angle grain boundaries were indicated by black lines.

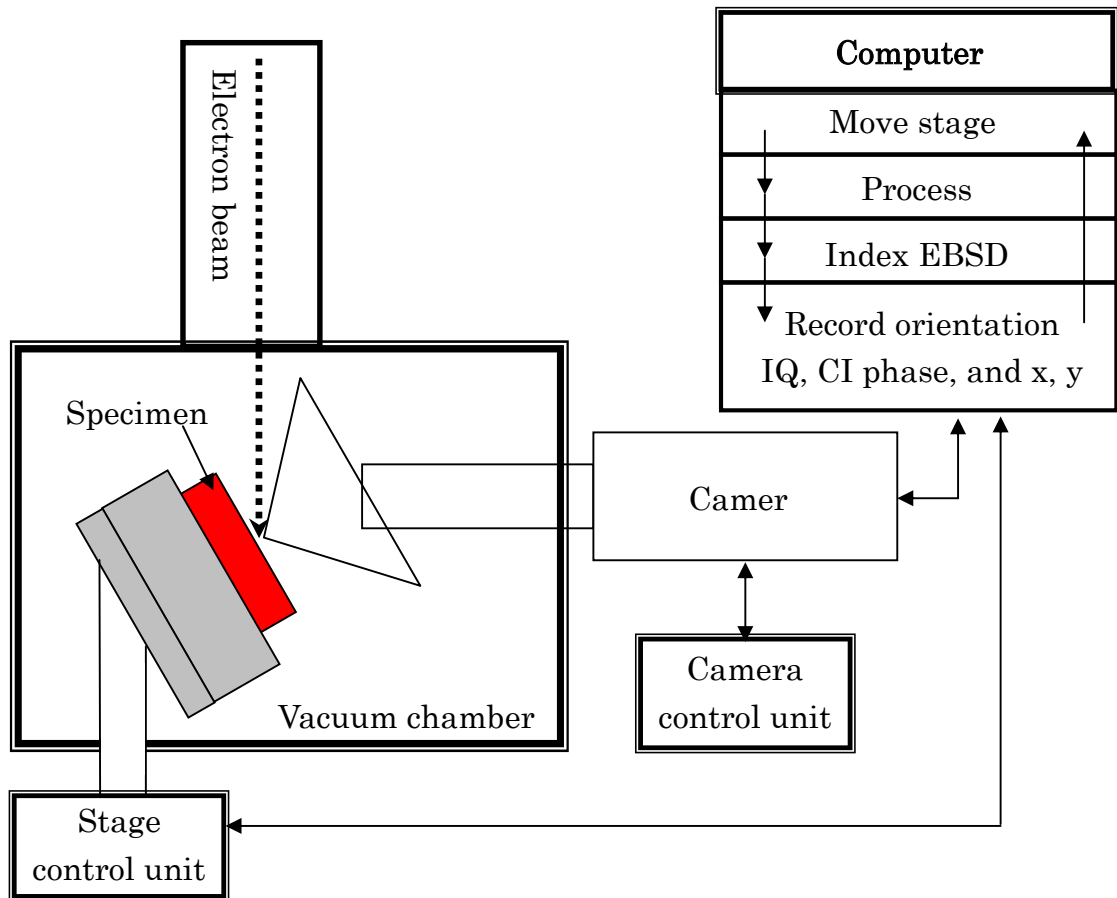


Fig. 2.2 Schematic view of EBSD system.

## 2. Experimental Procedure

---

### 2.5 Evaluation of bendability

The V-block method was used to evaluate the bendability of the processed material. Specimens of AA5182 with dimensions of  $6 \times 15 \times 1.5$  mm (width  $\times$  length  $\times$  thickness) were prepared by spark erosion machining for the bending test. Figure 2.3 shows a schematic view of the V-block method. The bending angle ( $\theta$ ) shown in Fig. 2.3 was set to certain values such as  $90^\circ$  and  $120^\circ$  for each experiment. The cross-head moved with a constant speed of 5 mm/min, and the radius  $r$  was 0.5 mm. After the bending test, the bending workability was evaluated by scanning electron microscopy (SEM) and EBSD measurements of the bent surface.

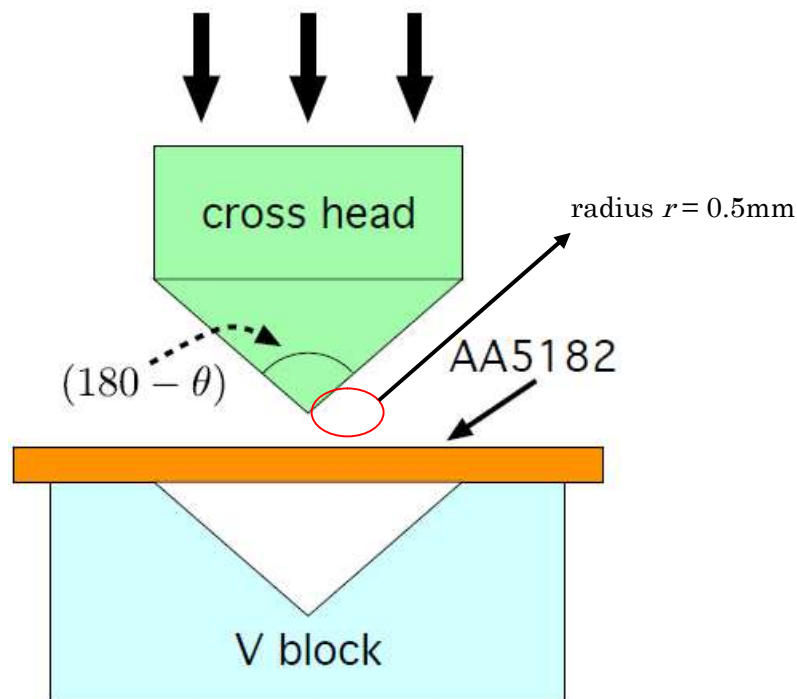


Fig. 2.3 Schematic view of V-block method.

## References

- [1] M. Dahms and H. J. Bunge : *J. Appl. Crystallogr.*, vol.22 (1989) pp.439~447.

## Chapter 3

# Texture Evolution of AA5182 Alloy during High Temperature Deformation

### 3. Texture Evolution of AA5182 Alloy during High Temperature Deformation

#### 3.1 Introduction

As described in chapter 1, texture is well known to strongly affect plastic workability [1-3]. Thus, controlling the texture is important for practical application of aluminum alloys. Moreover, understanding the mechanisms of texture formation is important because it can facilitate the development of processes for texture control.

Various textures appear in metals and alloys depending on the deformation modes, deformation mechanisms, and recrystallization mechanisms. Okayasu et al. investigated the relationship between texture development and deformation mechanisms by high-temperature uniaxial compression of Al–Mg binary alloys in a single phase state [4-7]. They found that {011} (compression plane) and {001} textures appeared depending on the temperature, strain rate, and amount of strain. They concluded that the texture transition from {011} to {001} with increasing strain should be attributed to grain boundary migration during deformation [4,5]. In this case, the formation of {011} texture in the initial stage of deformation has two physical meanings; lattice rotation toward the stable orientation against deformation and an increase in stored energy in crystal grains. Grain boundary migration is triggered at a certain degree of deformation, and then a texture transition from {011} to {001} occurs. They concluded that the {001} orientation could be understood as being stable against deformation and having lower stored energy because of its low Taylor factor. Since the stable orientation against deformation and the preferred orientation for grain boundary migration vary depending on the deformation mode [6], these results suggest that texture in binary Al–Mg alloys can be controlled by changing the deformation modes, such as rolling and extrusion, at high temperatures.

Experimental results on Al–Mg binary alloys [7,8] suggest the evolution of the {001} texture with high-temperature uniaxial compression in commercial AA5182 alloy bearing Mg as the primary alloy element, which implies the potential for texture control by hot working, as described above. However, alloy elements other than Mg in AA5182 may retard grain boundary migration, changing the texture development, as reported for an Al–Mg alloy with Al<sub>3</sub>Sc precipitates [6]. Thus, texture formation in AA5182 alloy is experimentally examined in this study.

### 3. Texture Evolution of AA5182 Alloy during High Temperature Deformation

---

#### 3.2 Experimental procedure

Cylindrical AA5182 specimens were prepared by spark erosion machining for compression tests. An aspect ratio of 1.5 was used for all specimen sizes. The chemical composition of AA5182 alloy is given in Table 2.1. The specimens were annealed at 843 K for 1000 min in air followed by further annealing at 773 K for 50 min before water quenching. Since the quench from 843 K resulted in small deformations in some cases, further annealing at 773 K was performed. EBSD measurement and texture measurement by an X-ray diffraction technique were conducted.

Uniaxial compression tests were conducted under a constant cross-head speed in air at temperatures of 673 K, 723 K, 773 K, and 823 K and strain rates of  $5.0 \times 10^{-4} \text{ s}^{-1}$ ,  $5.0 \times 10^{-3} \text{ s}^{-1}$ , and  $5.0 \times 10^{-2} \text{ s}^{-1}$ . Unless otherwise specified, all results reported below were obtained under these conditions.

#### 3.3 Results

##### 3.3.1 Initial microstructures

Figure 3.1 shows a grain structure map of the annealed AA5182 before compression. The map is based on EBSD measurements from the transverse direction (TD).

For the EBSD measurements, the mid-plane sections of the deformed specimens were prepared by mechanical and electrolytic polishing. These regions were scanned using the beam control option with a scan step of 4  $\mu\text{m}$ . When the minimum rotation angle  $\theta$  between neighboring measurement points was larger than  $15^\circ$ , high-angle grain boundaries were indicated by black lines. The method of measuring the size of equiaxed grains is described in ASTM E 112 [9]. The results show that the crystal grains are equiaxed with an average diameter of 112  $\mu\text{m}$ .

### 3. Texture Evolution of AA5182 Alloy during High Temperature Deformation

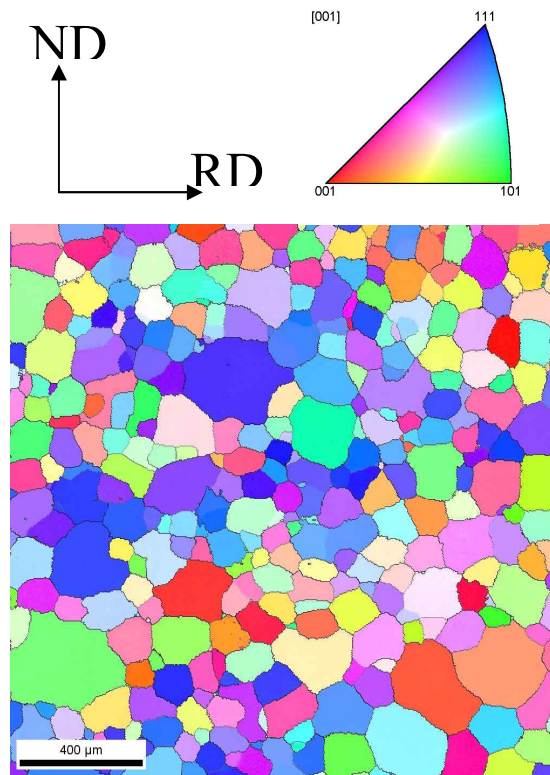


Fig. 3.1 Map of grain structure of AA5182 before compression based on EBSD measurements. Colors correspond to the orientations of the compression plane given above the map.

#### 3.3.2 Stress – strain curves

Figure 3.2 shows the true stress–true strain curves for deformation up to a strain of  $-1.0$ . The flow stresses increase with increasing strain rate at all temperatures and increase with decreasing temperature at the same strain rate. For example, the flow stress at 823 K at a strain rate of  $5.0 \times 10^{-3} \text{ s}^{-1}$  is close to 16 MPa. When the temperature decreases from 823 K to 673 K, the flow stress increases from 16 MPa to 59.4 MPa. This tendency is also observed at the other strain rates.

So-called high-temperature yielding is observed as the deformation in (a)–(c). These behaviors are similar to those of Al–5.0mass%Mg alloy. This indicates that solute atmosphere dragging is the dominant deformation mechanism under these deformation conditions [11]. However, high-temperature yielding does not appear at 823 K and a strain rate of  $5.0 \times 10^{-2} \text{ s}^{-1}$ . This suggests that the dominant deformation mechanism varies with the deformation conditions.

### 3. Texture Evolution of AA5182 Alloy during High Temperature Deformation

The flow stresses of Al–5mass%Mg with almost the same grain size are, however, much lower than those for AA5182 alloy [7]. The dislocation density of AA5182 is expected to be higher than that of binary Al–5mass%Mg alloy.

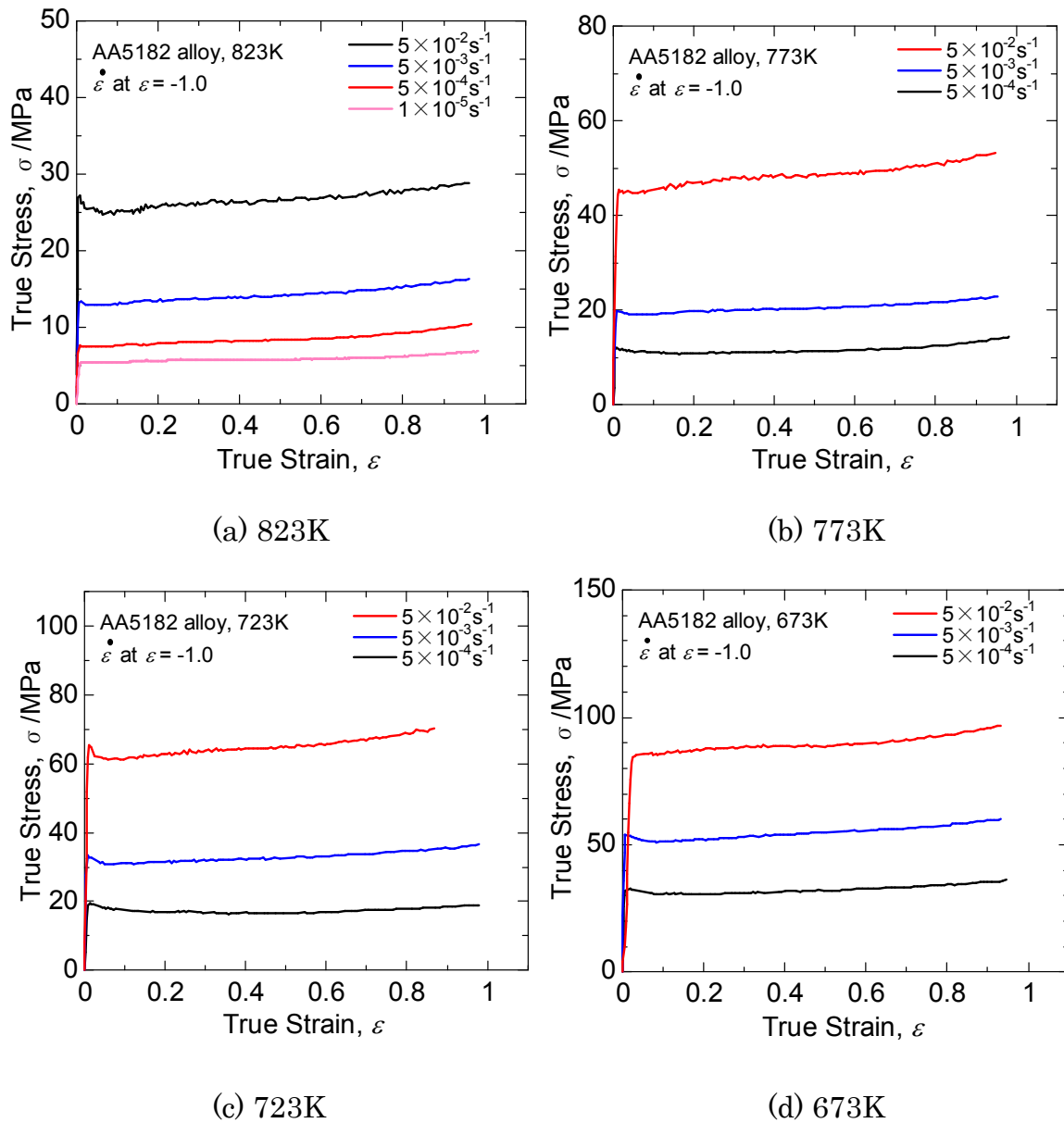


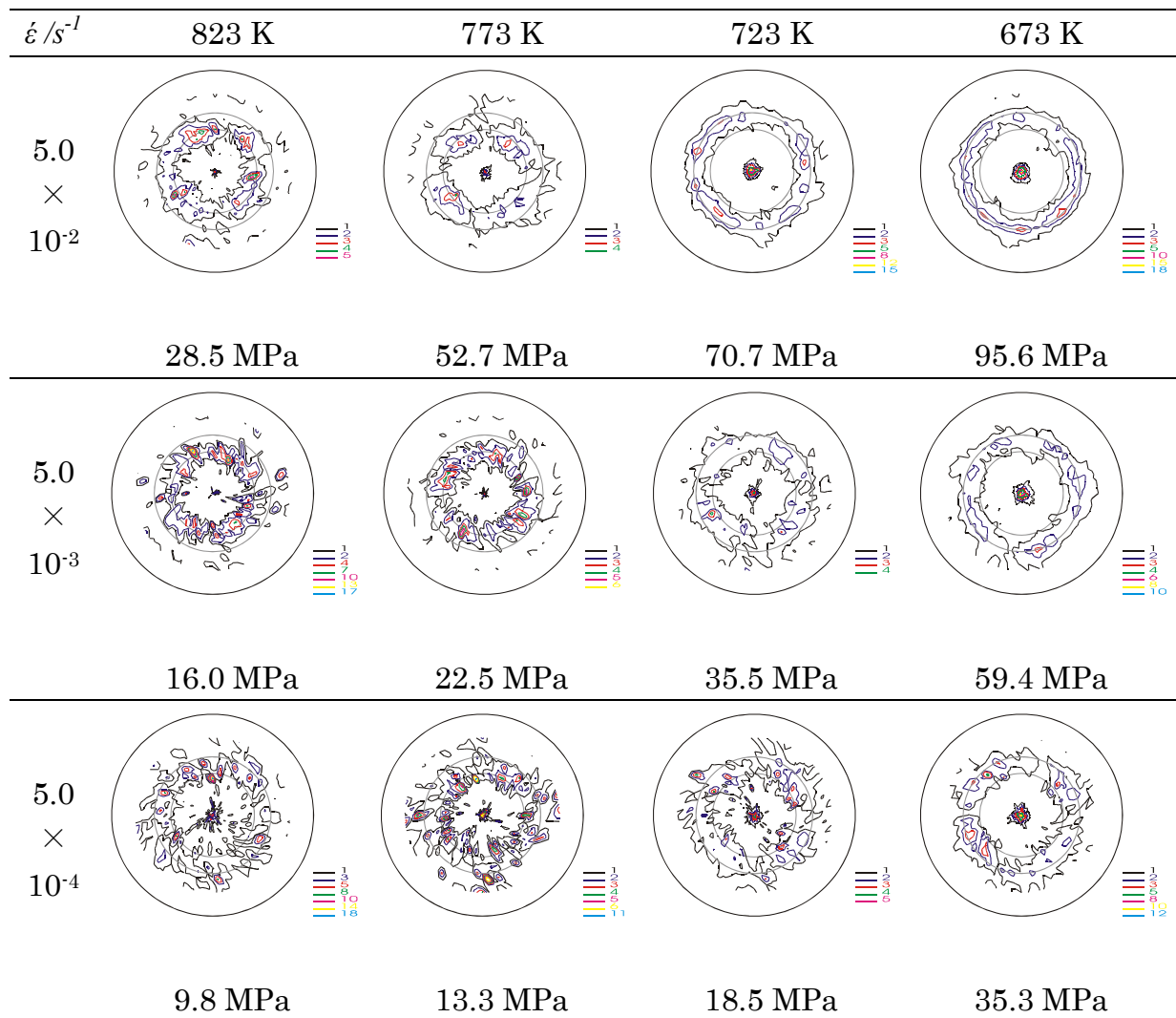
Fig. 3.2 True stress–true strain curves of AA5182 obtained by compression testing up to a true strain of  $-1.0$  at various strain rates and at deformation temperatures of (a) 823 K, (b) 773 K, (c) 723 K, and (d) 673 K, respectively.

#### 3.3.3 Characteristics of texture

### 3. Texture Evolution of AA5182 Alloy during High Temperature Deformation

Table 3.1 shows  $\{011\}$  pole figures for the samples after deformation up to a strain of  $-1.0$  for all deformation conditions. The pole densities are projected onto the compression plane. The average pole density is used as a unit. Two gray circles appear in the figures; the inner and outer circles show the poles  $45^\circ$  and  $60^\circ$  away from the center, respectively.

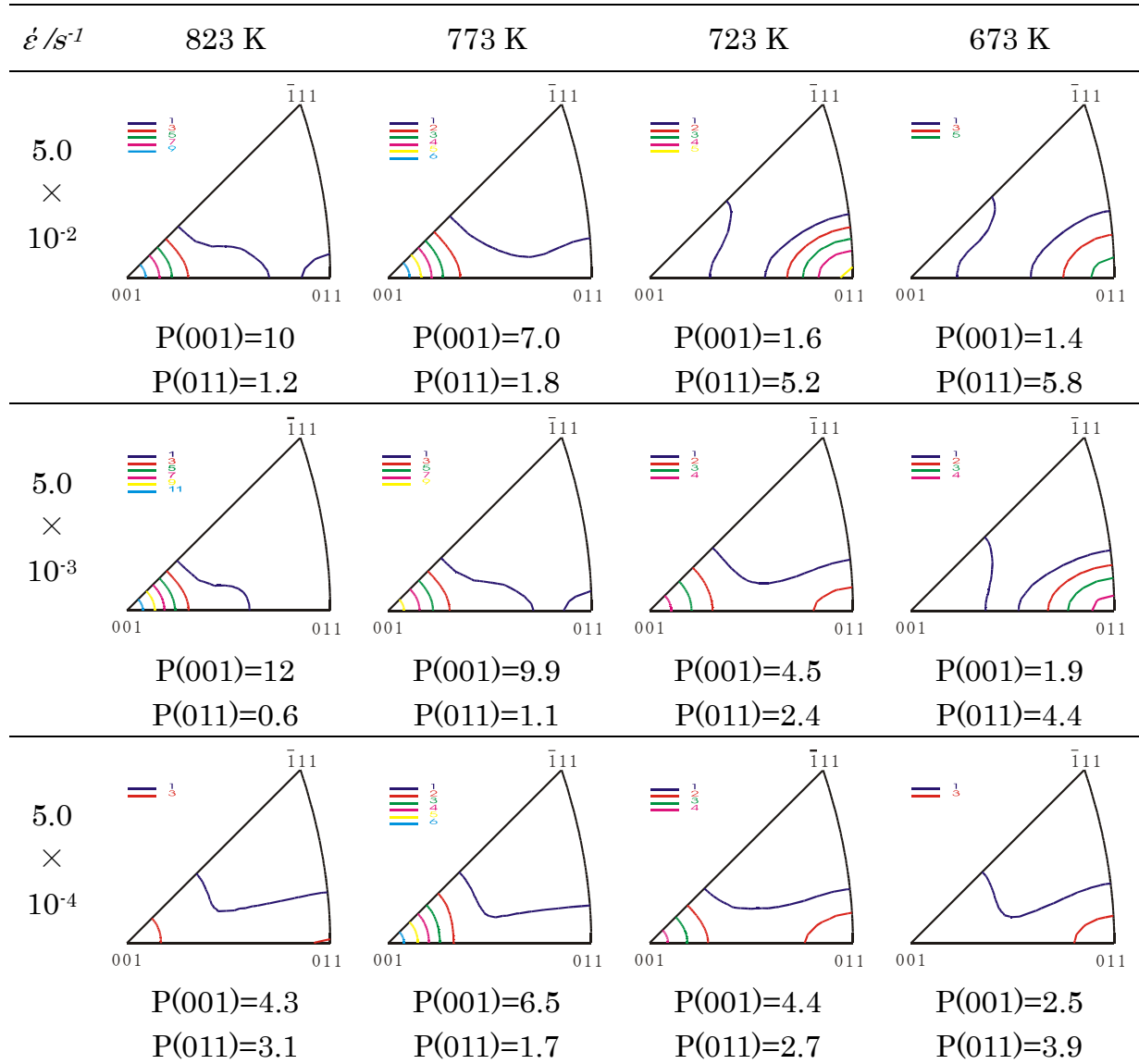
Table 3.1  $\{011\}$  pole figures after deformation up to a true strain of  $-1.0$  at various temperatures and strain rates. Pole density is projected onto the compression plane. Contours represent intervals in units of average pole density. Numerical values beneath the figures represent flow stresses.





### 3. Texture Evolution of AA5182 Alloy during High Temperature Deformation

Table 3.2 Inverse pole figures for compression planes of AA5182 under a true strain of  $-1.0$ . The average pole density is used as a unit for drawing the contour lines.



The pole densities are distributed in concentric circles in all cases. The concentric circular distribution of the pole densities appears under all deformation conditions, indicating the formation of fiber textures.

The distribution of high pole density depends on the deformation conditions in all cases. For example, at a strain rate of  $5.0 \times 10^{-2} s^{-1}$ , the area of high pole density at 823 K appears about  $45^\circ$  away from the center, but with increasing temperature, the area of high pole density changes gradually. Finally, at 673 K, it appears at the center and  $60^\circ$  away from the center. This tendency also

### 3. Texture Evolution of AA5182 Alloy during High Temperature Deformation

---

appears at strain rates of  $5.0 \times 10^{-3} \text{ s}^{-1}$  and  $5.0 \times 10^{-4} \text{ s}^{-1}$ . This indicates that the main component of the texture depends on the deformation conditions.

Next, the main component of the fiber texture in all specimens was examined on the basis of the ODF. Table 3.2 shows the inverse pole figures showing the spatial distribution of poles for the compression planes of specimens deformed at various temperatures and strain rates up to a strain of  $-1.0$ . The contour lines represent intervals of the average pole density. Some general trends appear; for example, the  $\{001\}$  component evolves and the  $\{011\}$  component weakens with increasing temperature at the same strain rate. However, both texture components and their sharpness vary in a complex manner depending on the temperature and strain rate.

#### 3.3.4 Grain structure maps

Figure 3.3 shows the grain structure maps of specimens after deformation up to a true strain of  $-1.0$ . The deformation conditions and flow stress are shown beneath the figures. Observations were conducted on the compression plane, and the orientation of the compression axis is given. Grain colors correspond to the orientations given above the map. Equiaxed grain structures were constructed for all cases. The grain structure varies with the deformation conditions. The microstructure in Fig. 3.3(a) consists of large equiaxed grains, and no texture development appears in this case. This coincides with the results given in Table 3.2, where the pole densities at (001) and (011) are 4.3 and 3.1, respectively. Figure 3.4 shows the corresponding grain structure maps of samples deformed at 823 K at a strain rate of  $5.0 \times 10^{-4} \text{ s}^{-1}$  up to true strains of  $-0.6$ ,  $-1.0$ , and  $-1.5$ . The  $\{001\}$  component increases and the  $\{011\}$  component decreases with increasing strain from  $-0.6$  [Fig. 3.4(a)] to  $-1.0$  [Fig. 3.4(b)] and then to  $-1.5$  [Fig. 3.4(c)].

The microstructure in Fig. 3.3(b) consists of a mixture of large  $\{001\}$  grains and small grains. To clarify the formation process of  $\{001\}$  texture, grain structure maps of specimens deformed at 773 K at a strain rate of  $5.0 \times 10^{-3} \text{ s}^{-1}$  up to strains of  $-0.6$ ,  $-0.8$ , and  $-1.0$  are presented in Fig. 3-5(a), 3-5(b), and 3-5(c), respectively. The maps were measured on the mid-plane section, and equiaxed grain structures were constructed. The inverse pole figure for Fig. 3.5(c) is given in Table 3.2, which shows that the pole density at (001) is 9.9 times the random level. The area fraction of  $\{001\}$  increases with increasing

### 3. Texture Evolution of AA5182 Alloy during High Temperature Deformation

---

strain, whereas that for  $\{011\}$  decreases. The  $\{001\}$ -oriented grains seem to be larger than those with other orientations.

Figure 3.3(c) shows the microstructure after deformation at 673 K at a strain rate of  $5.0 \times 10^{-2} \text{ s}^{-1}$  up to a strain of  $-1.0$ . As shown in Table 3.2, the pole density at  $(001)$  under these conditions is 1.4, whereas that at  $(011)$  is 5.8; the texture transition from  $\{011\}$  to  $\{001\}$  is not seen in this case. Grains with the  $\{011\}$  orientation are much larger than before deformation. Figure 3.6 shows grain structure maps of specimens deformed at 673 K at a strain rate of  $5.0 \times 10^{-2} \text{ s}^{-1}$  up to true strains of  $-0.6$ ,  $-0.8$ , and  $-1.0$ . In Fig. 3.6(a), where the true strain is  $-0.6$ , the microstructure consists of large  $\{001\}$  and  $\{011\}$  grains with some small grains. As the strain increases to  $-0.8$  [Fig. 3.6(b)] and then  $-1.0$  [Fig. 3.6(c)], the area of the  $\{011\}$  component increases, and that of the  $\{001\}$  component decreases. Unlike the results shown in Fig. 3.3(b), many small grains are generated along the grain boundaries. This suggests that large grains with the  $\{011\}$  orientation are formed by compression deformation with crystal rotation by  $\{111\}\langle 110 \rangle$  slip.

### 3. Texture Evolution of AA5182 Alloy during High Temperature Deformation

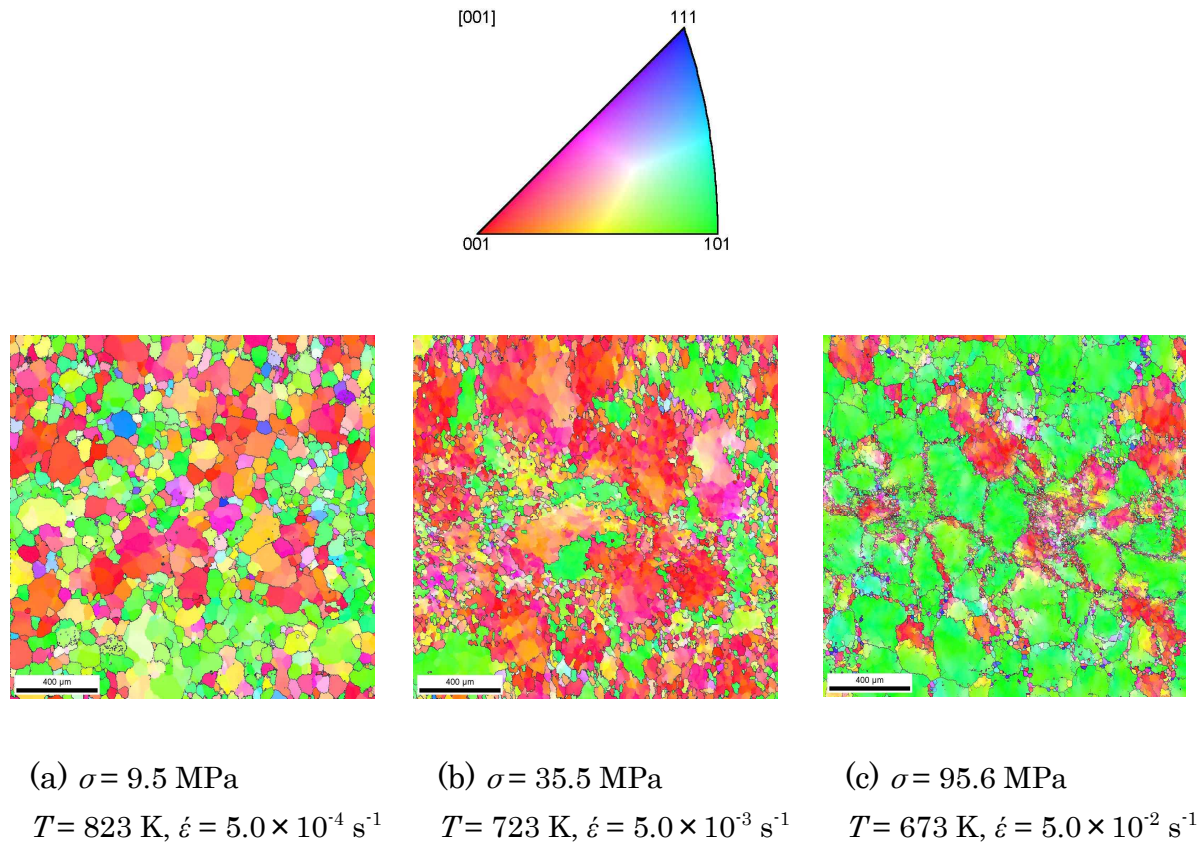


Fig. 3.3 Grain structure maps derived from EBSD measurement of AA5182 compressed at various temperatures and strain rates of  $5.0 \times 10^{-4}$  s $^{-1}$ ,  $5.0 \times 10^{-3}$  s $^{-1}$ , and  $5.0 \times 10^{-2}$  s $^{-1}$  up to a true strain of  $-1.0$ . Black lines represent high-angle grain boundaries with misorientation angles ( $\theta$ ) of greater than  $15^\circ$ .

### 3. Texture Evolution of AA5182 Alloy during High Temperature Deformation

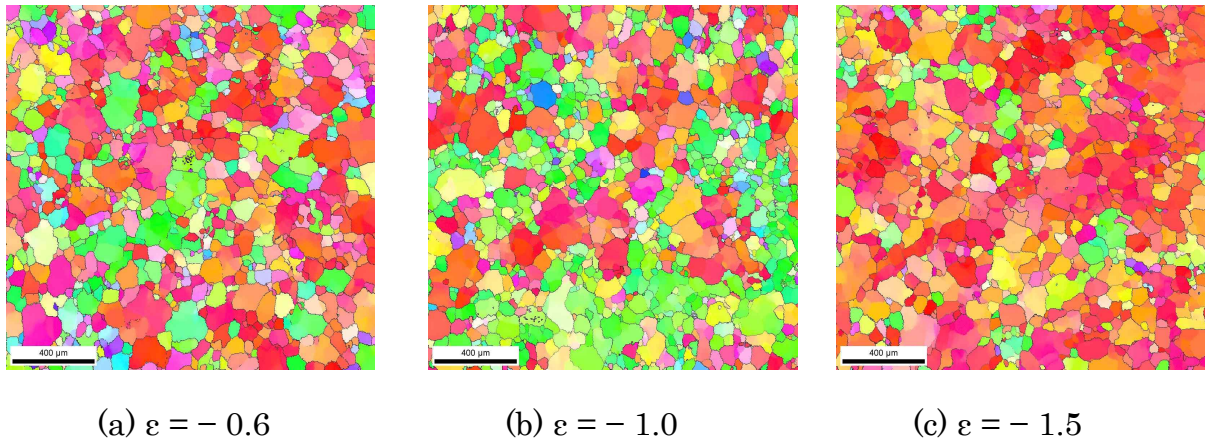


Fig. 3.4 Grain structure maps derived from EBSD measurements of AA5182 compressed at 823 K at a strain rate of  $5.0 \times 10^{-4} \text{ s}^{-1}$  up to a true strain of (a)  $-0.6$ , (b)  $-1.0$ , and (c)  $-1.5$ . Black lines represent high-angle grain boundaries with misorientation angles ( $\theta$ ) of greater than  $15^\circ$ .

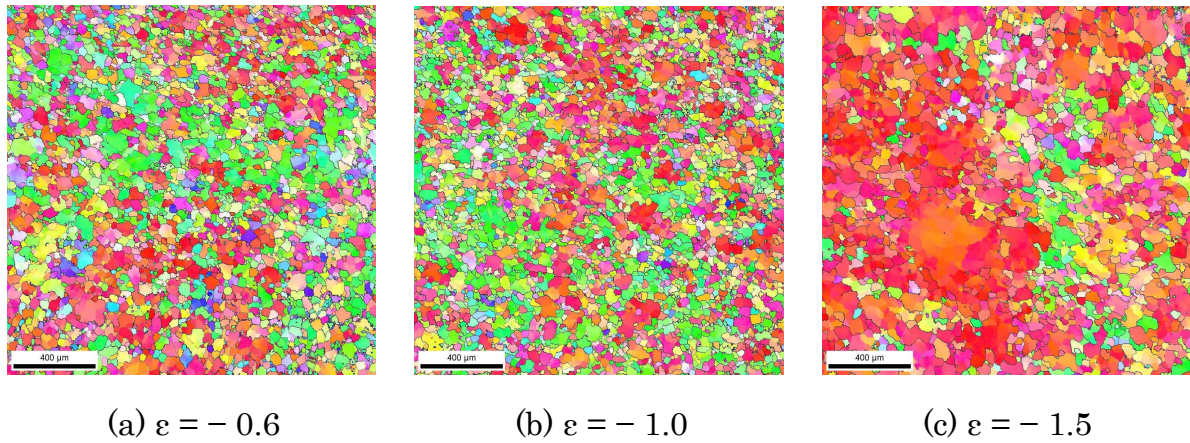


Fig. 3.5 Grain structure maps derived from EBSD measurement of AA5182 compressed at 773 K at a strain rate of  $5.0 \times 10^{-3} \text{ s}^{-1}$  up to a true strain of (a)  $-0.6$ , (b)  $-1.0$ , and (c)  $-1.5$ , respectively. Black lines represent high-angle grain boundaries with misorientation angles ( $\theta$ ) of greater than  $15^\circ$ .

### 3. Texture Evolution of AA5182 Alloy during High Temperature Deformation

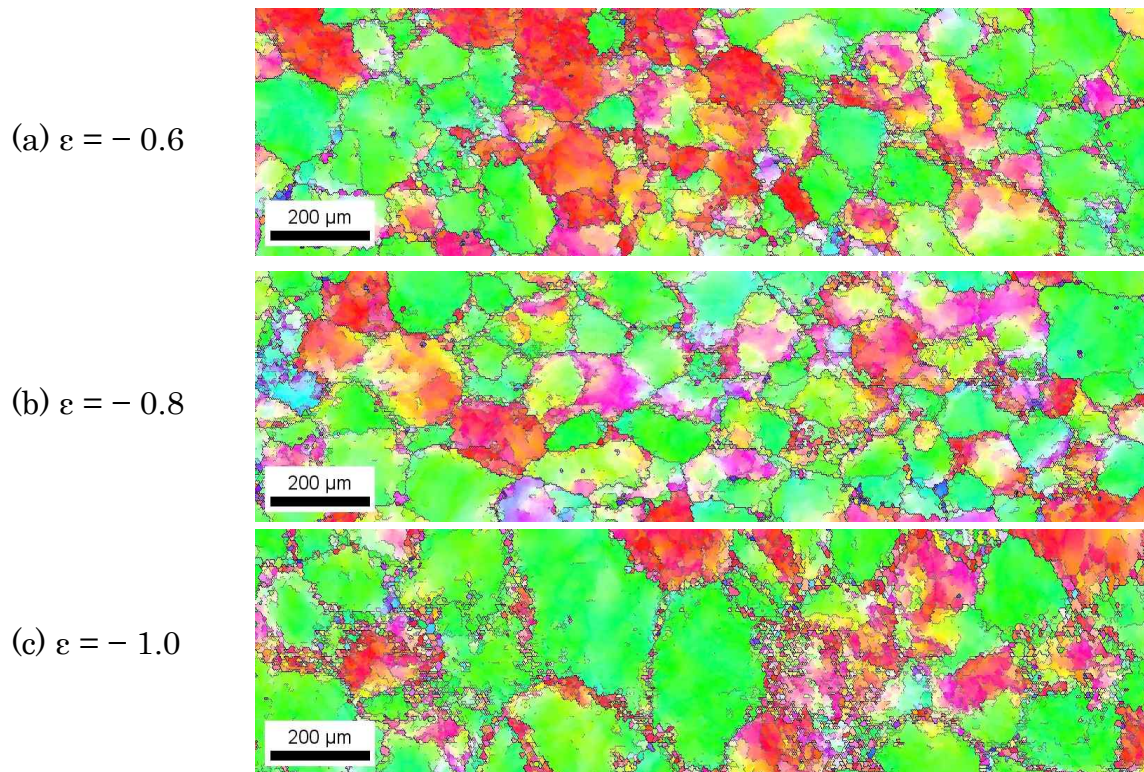


Fig. 3.6 Grain structure maps derived from EBSD measurements of AA5182 compressed at 673 K at a strain rate of  $5.0 \times 10^{-2} \text{ s}^{-1}$  up to a true strain of (a)  $-0.6$ , (b)  $-0.8$ , and (c)  $-1.0$ . Black lines represent high-angle grain boundaries with misorientation angles ( $\theta$ ) of greater than  $15^\circ$ .

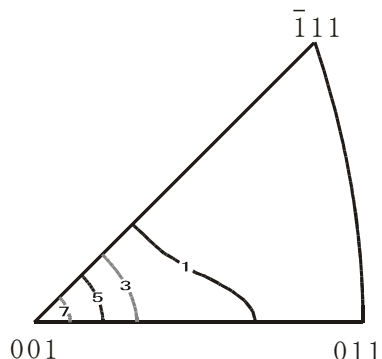
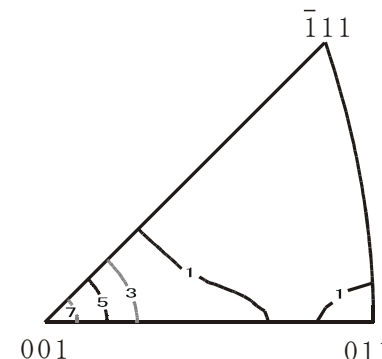
#### 3.4 Discussion

##### 3.4.1 Comparison of the textures formed in Al-5mass%Mg and AA5182

As shown in Table 2.1, AA5182 is an aluminum alloy containing about 4.5mass% of Mg. Okayasu and Fukutomi [7] investigated the textures developed under high-temperature uniaxial compression of Al-5mass%Mg alloy at various temperatures and strain rates. They found that  $\{001\}$  texture became sharpest after deformation at 673 K and 723 K with a strain rate of  $5.0 \times 10^{-4} \text{ s}^{-1}$  and a strain of  $-1.0$ . The textures produced under these two deformation conditions are shown in Table 3.3.

### 3. Texture Evolution of AA5182 Alloy during High Temperature Deformation

Table 3.3 Inverse pole figures for compression planes of Al–5mass%Mg deformed at a strain rate of  $5.0 \times 10^{-4} \text{ s}^{-1}$  up to a true strain of  $-1.0$  [7]. Contour lines represent intervals in units of average pole density.  $P(001)$  and  $P(011)$  are the pole densities at (001) and (011), respectively. Flow stress is given below each figure.

	723 K	673 K
Al–5mass%Mg	 <p><math>P(001)=8.1, P(011)=0.6, 13\text{MPa}</math></p>	 <p><math>P(001)=8.1, P(011)=1.1, 20\text{MPa}</math></p>

A comparison of Table 3.3 with the results for AA5182 under the same deformation conditions (Table 3.2) reveals that the pole densities at (001) of AA5182 are much lower than those for Al–5mass%Mg; the pole densities of Al–5mass%Mg are greater than 8, whereas those for AA5182 are less than 5. Furthermore, the main component of AA5182 is {011} after deformation at 673 K; that is, the development of {001} is suppressed in AA5182. Okayasu et al. [5] investigated texture formation in Al–3Mg alloys with  $\text{Al}_3\text{Sc}$  precipitates and found that the formation of the {001} component was remarkably retarded. This suggests that grain boundary migration enhances the development of the {001} component.

According to Table 3.3, the flow stresses of Al–5mass%Mg at 673 K and 723 K are 20 MPa and 13 MPa, respectively. The stresses for AA5182 under the same deformation conditions are much higher: 35 MPa and 19 MPa. Because the Mg concentration is 4.5mass% in AA5182, the difference in the flow stress between the binary alloys and AA5182 cannot be attributed to a difference in Mg content. However, AA5182 contains other solute elements, such as Mn and Cu. Furthermore, any particles that are present might increase the flow stress, although their existence was not confirmed in this study. High-temperature

### 3. Texture Evolution of AA5182 Alloy during High Temperature Deformation

yielding was seen in the deformation of AA5182. This indicates that solute atmosphere dragging is the dominant deformation mechanism. Hence, the higher flow stresses of AA5182 are believed to correspond to higher dislocation densities [11], which drive grain boundary migration. Because no great difference in shear modulus is expected between the binary alloys and AA5182, the difference in flow stress indicates that the driving force for grain boundary migration in AA5182 might be higher than that for the binary alloys. However, the {001} component does not evolve. Thus, elements other than Al and Mg in AA5182 can be said to suppress grain boundary migration, resulting in weak development of the {001} component.

As shown in Table 3.2, the {001} texture is sharpest at 823 K; the maximum pole density is as much as 12 times the random level. This indicates that the higher mobility of grain boundaries is important in the formation of {001} texture in AA5182. The effects of temperature and strain rate on the development of {001} texture are discussed in detail in sections 3.4.2 and 3.4.3.

#### 3.4.2 Effect of deformation conditions on texture formation

As mentioned in section 3.2, the formation of fiber texture is confirmed under all the deformation conditions examined here. Table 3.2 shows that the area of high pole density appears in (001) and/or (011). The pole densities vary depending on both the deformation temperature and the strain rate. Moreover, the pole densities between the two areas of high pole density are quite low; that is, the pole densities are not continuous between the two areas. This is a manifestation of the transition mechanism from {011} to {001}. If slip deformation generates a texture change, the pole densities should be continuously distributed from (011) toward (001).

The pole densities at (001) decrease monotonically with decreasing temperature at a strain rate of  $5.0 \times 10^{-2} \text{ s}^{-1}$ . In contrast, the pole densities at (011) increase with decreasing temperature. This tendency, however, is not seen at a strain rate of  $5.0 \times 10^{-4} \text{ s}^{-1}$ . The effect of the strain rate on the pole densities at (001) and (011) also seems to be complicated. For example, the pole density at (001) increases with a decrease in the strain rate from  $5.0 \times 10^{-2} \text{ s}^{-1}$  to  $5.0 \times 10^{-3} \text{ s}^{-1}$ . However, a further decrease in strain rate to  $5.0 \times 10^{-4} \text{ s}^{-1}$  decreases the pole density, except for samples treated at 673 K. These results indicate that several factors affect the development of the pole density at (001), and the predominant factor varies with both the temperature and the strain rate.



### 3. Texture Evolution of AA5182 Alloy during High Temperature Deformation

Figure 3.7 shows the relationship between the flow stress at a strain of  $-1.0$  and the mean grain sizes of  $\{001\}$  grains and all grains under deformation conditions yielding pole densities at  $(001)$  of more than 4 times the random level. EBSD measurements were used with a scan step of  $4\ \mu\text{m}$ . In the evaluation of grain size, grains smaller than  $10\ \mu\text{m}$  were omitted in order to use only reliable data for mean grain sizes for  $\{001\}$  grains and all grains. In all cases, the mean grain size for  $\{001\}$  is larger than that for all grains. Since the latter includes grains with the  $\{001\}$  orientation, grains with other orientations are much smaller than those with the  $\{001\}$  orientation. This indicates that the preferential growth of  $\{001\}$  grains by grain boundary migration drives the development of  $\{001\}$  texture.

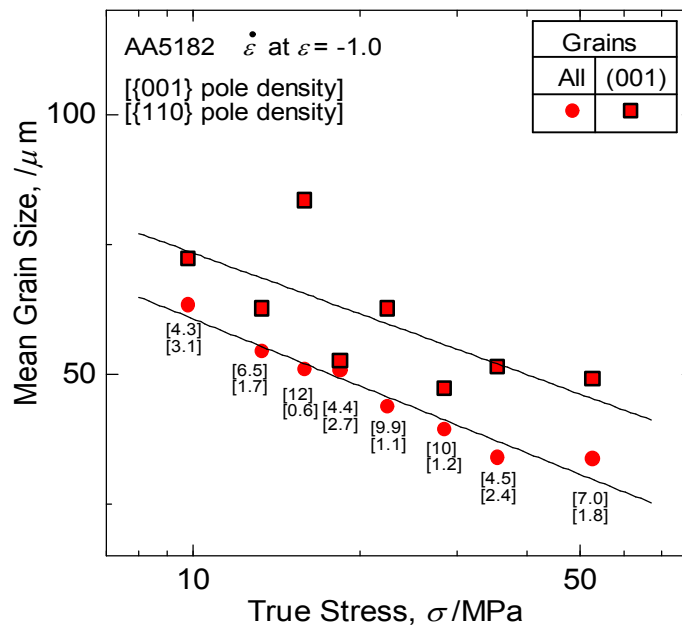


Fig. 3.7 Relationship between flow stress at a true strain of  $-1.0$  and mean grain size for  $\{001\}$  grains and for all grains.

#### 3.4.3 $\{001\}$ texture map

The  $\{001\}$  texture has both negative and positive effects on the plastic workability of aluminum alloys. Thus, it is important to clarify the deformation conditions for the development of the  $\{001\}$  component. As discussed in section 3.4.2, grain boundary migration is the key process for the development of  $\{001\}$  texture. This is examined in the  $\{001\}$  texture map in Fig. 3.8, in which texture

### 3. Texture Evolution of AA5182 Alloy during High Temperature Deformation

sharpness is plotted against flow stress (stored energy) and deformation temperature (grain boundary mobility). The vertical and horizontal axes are the strain rate and reciprocal of the absolute temperature, respectively.

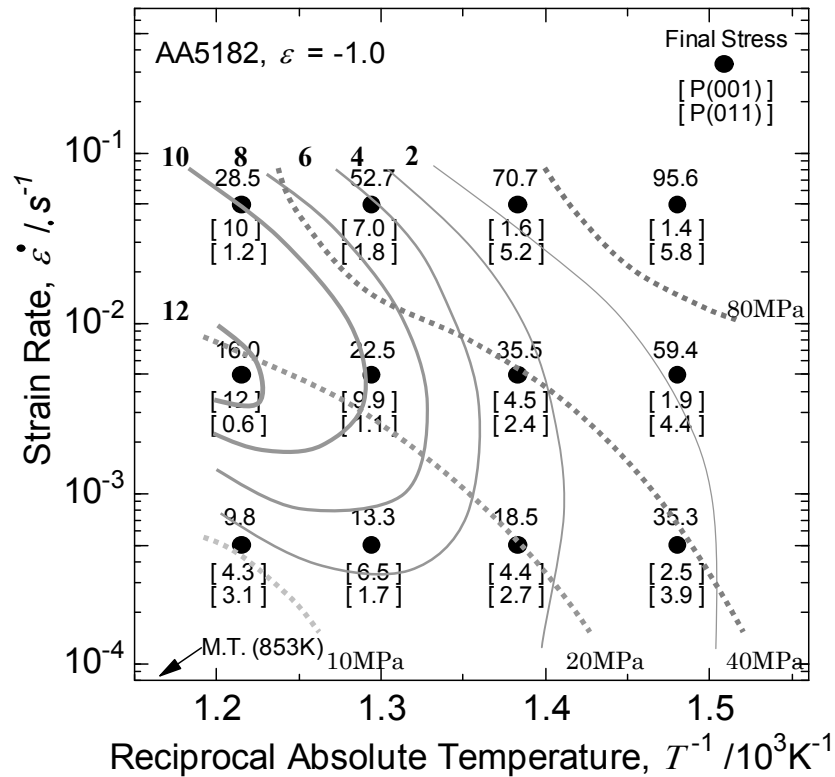


Fig. 3.8 {001} texture map of AA5182 at a true strain of  $-1.0$  showing the effect of strain rate and temperature on the development of {001} texture. Broken lines represent constant flow stress contours. Numerical values beneath the closed circles are the pole densities at (001) and (011) from the inverse pole figures in Table 3.2. Solid gray lines indicate contour lines for pole densities of 2, 4, 6, 8, 10, and 12.

Examination of the pole densities for (001) along the same flow stress elucidates important aspects of {001} formation. For example, the pole densities for 20 MPa increase from 4.4 to 9.9 and then to 12. Thus, if the stored energy level is the same, a higher temperature results in sharper {001} texture. The same trend also appears for 40 MPa. For higher stresses such as 80 MPa, this feature is not seen because the deformation mechanism changes, as suggested by the grain structure map in Fig. 3.6. When the flow stress is lower than 10 MPa, the {001} texture weakens. As discussed in section 3.4.1, the development of {001} is believed to be

### 3. Texture Evolution of AA5182 Alloy during High Temperature Deformation

attributable to grain boundary mobility and the strength of the driving force. Thus, the weakening of the texture might be understood as the result of a decrease in the driving force.

#### 3.4.4 Deformation mechanism at high temperatures

To understand the relationship between the pole density, temperature, and strain rate on the development of  $\{001\}$  texture, the effect of the deformation mechanism should be considered.

Changes in the deformation mechanism with the stress level have been discussed on the basis of results for binary Al–Mg alloys [13,14]. For AA5182 alloy, the grain structure map in Fig. 3.3 also suggests that the deformation mechanism at high temperatures depends on the deformation conditions. As shown in section 3.4.3, the dominant mechanisms of texture formation appear to depend on the deformation conditions. The dislocation structure is known to depend on the deformation mechanism [11].

At high temperatures, various deformation mechanisms appear in solid solution alloys depending on the temperature and strain rate. As shown in Fig. 3.2, work softening appears under most of the deformation conditions examined in the present study. This suggests that atmosphere dragging dominates the slip deformation of this alloy. Horiuchi and Otsuka [11] reported that solute atmosphere dragging generates a homogeneous distribution of dislocations, whereas the other two mechanisms form subgrain structure. The orientation dependence of the stored energy is considered to be enhanced by the homogeneous dislocation distribution because the strain fields of individual dislocations are less relaxed than when subgrains are formed.

To elucidate the deformation mechanism, the relationship between the true strain rate and true stress at a true strain of  $-0.5$  is examined in Fig. 3.9.

The double logarithmic plot shows a linear relationship between the strain rates and flow stresses at the four temperatures examined here. The slopes of these lines (the stress exponents) are 3.1, 3.4, or 4.5, depending on the temperature.

Chapter 1 explained the meaning of the stress exponent  $n$  for binary Al alloys at high temperatures. Oikawa et al. [12] investigated the deformation mechanism of Al–2.2mol%Mg by creep tests with stresses from 4 to 50 MPa and found stress exponents of 5.0, 3.0, and 6.0 for low-stress, medium-stress, and high-stress conditions, respectively. Yavari and Langdon [13] also showed the same change in the stress exponent in high-temperature deformation of

### 3. Texture Evolution of AA5182 Alloy during High Temperature Deformation

Al–3.3mol%Mg and Al–5.6mol%Mg. They concluded that these changes in stress exponent originate from three different deformation mechanisms: free flight motion, viscous motion of dislocations dragged by the solute atmosphere, and the breakaway of dislocations from the solute atmosphere [14]. The change in stress exponents observed in the present study is the same as in the results described above, suggesting that high-temperature deformation of AA5182 is dominated by the same mechanisms reported for Al–Mg binary alloys [16].

When the dominant deformation mechanism is the motion of dislocations dragged by the solute atmosphere, {001} texture develops at high temperatures. However, the microstructure deformed at 673 K and a strain rate of  $5.0 \times 10^{-2}$  up to true strain of  $-1.0$  consists of large {011} grains and many small grains, as shown in Fig. 3.6. The formation of {011} can be attributed to the activation of {111}<110> slip.

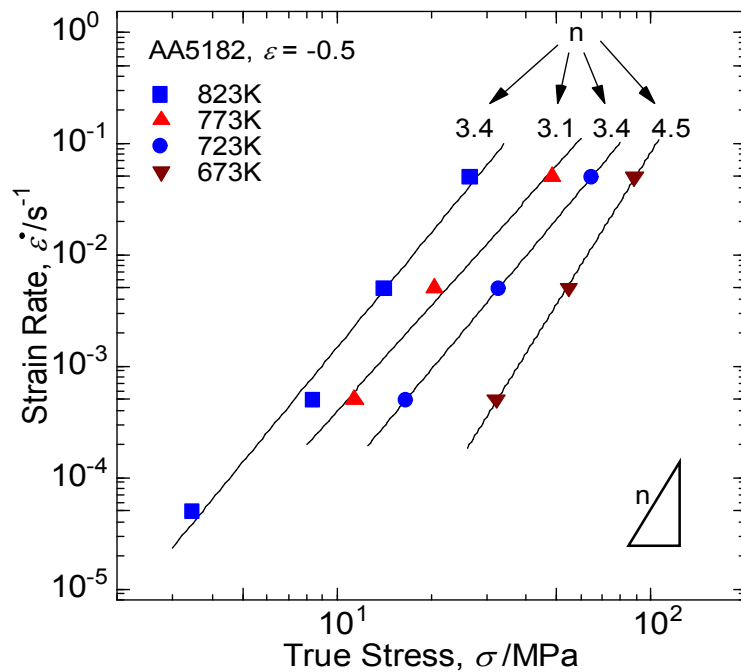


Fig. 3.9 True stress vs. true strain rate for the compression of AA5182 up to a true strain of  $-0.5$  at various temperatures. Squares, triangles, circles, and inverted triangles represent temperatures of 823 K, 773 K, 723 K, and 673 K, respectively.

### 3. Texture Evolution of AA5182 Alloy during High Temperature Deformation

#### 3.5 Conclusions

The formation of {001} (compression plane) texture by high-temperature uniaxial compression of AA5182 was studied and compared with previous results for Al–Mg binary alloys. The major results are as follows.

- (1) A change in texture from {011} (compression plane) to {001} with increasing strain occurs in AA5182 as well as in the binary alloys. The texture in AA5182, however, is much weaker than that for binary alloys with similar Mg content under the same deformation conditions.
- (2) The {001} grains are much larger than other grains under the deformation conditions that produce sharp {001} texture. This indicates that the formation of {001} texture after a large amount of strain should be attributed to grain boundary migration.
- (3) The sharpness of the {001} component cannot be simply given as a function of temperature or strain rate. To understand the texture formation process, an {001} texture map is proposed in which the texture sharpness for the {001} component is presented by contours within the temperature–strain rate field with additional contours for flow stresses. The texture map helps to identify the process conditions for texture control.
- (4) Examination of the {001} texture map reveals that higher temperatures yield a sharper {001} texture for the same flow stress. This also suggests a key role for grain boundary migration in the development of {001} texture.

#### References

### 3. Texture Evolution of AA5182 Alloy during High Temperature Deformation

- [1] H. Inoue and T. Takasugi: *Mater. Trans.* **48** (2007) pp. 2014–2022.
- [2] H. Murakami and T. Senuma: *ISIJ Int.* **38** (1998) pp. 653–660.
- [3] S. Ikawa, M. Asano and S. Hirano: *Abstracts of the 116th Annual Meeting of the Japan Institute of Light Metals* (2009) pp. 301–302.
- [4] K. Okayasu and H. Fukutomi: *J. Japan Inst. Metals* **70** (2006) pp. 562–567.
- [5] K. Okayasu, H. Takekoshi and H. Fukutomi: *Mater. Trans.* **48** (2007) pp. 2002–2007.
- [6] K. Okayasu, M. Sakakibara and H. Fukutomi: *Materials Processing and Texture: Ceramic Transactions* **200** (2008) pp. 679–685.
- [7] K. Okayasu and H. Fukutomi: *J. Japan Inst. Metals* **73** (2009) pp. 58–63.
- [8] M. Otsuka and R. Horiuchi: *J. Japan Inst. Metals* **36** (1972) pp. 809–817.
- [9] “Standard Methods for Estimating the Average Grain Size of Metals,” E 112, *Annual Book of ASTM Standards*, Vol. 03.03, ASTM, Philadelphia (1984) pp. 120–152.
- [10] M. Dahms and H. J. Bunge: *J. Appl. Crystallogr.* **22** (1989) pp. 439–447.
- [11] R. Horiuchi and M. Otsuka: *Trans. Japan Inst. Metals* **13** (1972) pp. 284–293.
- [12] H. Oikawa, K. Sugawara and S. Karashima: *Trans. Japan Inst. Metals* **19** (1978) pp. 611–616.
- [13] P. Yavari and Terence. G. Langdon: *Acta. Metall.* **30** (1982) pp. 2181–2196.
- [14] H. Oikawa, H. Sato and K. Maruyama: *Mater. Sci. Eng.* **75** (1985) pp. 21–28.
- [15] S. Kikuchi, Y. Motoyama and M. Adachi: *J. Japan Inst. Light Metals* **30** (1980) pp. 449–455.
- [16] H. Oikawa, K. Honda and S. Ito: *Mater. Sci. Eng.* **64** (1984) pp. 237–245.

## Chapter 4

# Texture Formation in AA5052 Alloy under Uniaxial Compression at High Temperatures

## 4. Texture Formation in AA5052 Alloy under Uniaxial Compression at High Temperatures

### 4.1 Introduction

AA5182 aluminum alloy is used in the automotive industry because of its light weight, high strength, and high corrosion resistance. However, to promote further application, the workability must be improved by controlling the texture.

Among 5xxx series commercial alloys, AA5052 aluminum alloy is the basic material used in not only the automotive industry but also other applications such as ship parts. Reducing vehicle weight through the use of excellent materials such as commercial aluminum alloys has become important because it improves fuel economy. Hence, improvements in the workability of AA5052 alloy by texture control are crucial for its application in various industries.

Chapter 3 describes experimental investigations into texture formation by high-temperature deformation of AA5182 aluminum alloy. The Mg concentration, which affects the development of {001} texture in binary Al–Mg alloys [1], is lower in AA5052 alloy than in AA5182 alloy. The {001} orientation develops by deformation when dislocations are distributed uniformly owing to the effect of the solute atmosphere [2]. Thus, the sharpness of the {001} texture is expected to depend on the Mg concentration.

However, few studies have reported on texture formation and sharpness after high-temperature deformation of commercial aluminum alloys despite this topic's importance for practical application of the findings for Al–Mg binary alloys. In this chapter, texture formation by uniaxial compression deformation at high temperatures in AA5052 alloy is experimentally investigated, and the results are compared with previous results for binary Al–Mg alloys. Finally, {001} texture maps that show the relationships among temperature, strain rate, and flow stress are established on the basis of the experimental results.

### 4.2 Experimental procedure

Cylindrical specimens were prepared for compression tests by spark



#### 4. Texture Formation in AA5052 Alloy under Uniaxial Compression at High Temperatures

erosion machining. The specimens were annealed at 853 K for 1–100 min in air and were quenched in water after the annealing. To obtain equiaxed grains, the annealing conditions were chosen on the basis of Vickers hardness measurements. The effect of annealing on the hardness restoration was examined. The Vickers hardness values were obtained under a load of 200 g and a holding time of 5 s.

Figure 4.1 shows the relationship between Vickers hardness and annealing times at 853 K of up to 100 min. The hardness of the as-received AA5052 alloy is 55 Hv. After annealing for 100 min, the Vickers hardness was 47 Hv. Hence, an annealing condition of 100 min at 853 K was chosen.

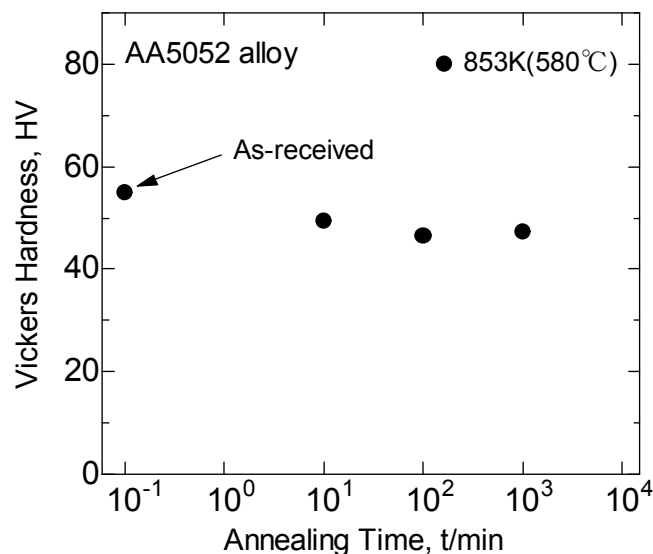


Fig. 4.1 Vickers hardness vs. annealing time for AA5052 alloy. Annealing was conducted at 853 K.

Figure 4.2 shows the grain structure map of AA5052 alloy after annealing at 853 K for 100 min. The map was constructed on the basis of EBSD measurements from the normal direction (ND).

Uniaxial compression tests were conducted under a constant cross head speed in air at temperatures of 673 K, 723 K, 773 K, and 823 K and strain rates of  $5.0 \times 10^{-4} \text{ s}^{-1}$ ,  $5.0 \times 10^{-3} \text{ s}^{-1}$ , and  $5.0 \times 10^{-2} \text{ s}^{-1}$ . The final strain rate was evaluated at a strain of  $-1.0$  on the basis of the cross head speed and

#### 4. Texture Formation in AA5052 Alloy under Uniaxial Compression at High Temperatures

specimen height. Unless otherwise specified, the results reported below were obtained under these conditions.

EBSD measurements and texture measurements by an X-ray diffraction technique were conducted for mid-plane sections of the deformed specimens. The  $\{001\}$ ,  $\{011\}$ , and  $\{111\}$  pole figures were constructed using diffracted X-ray intensities measured on the 111, 200, and 220 reflections, respectively. By using these three pole figures, the ODF was calculated by the Dahms–Bunge method [3]. Textures were evaluated on the basis of pole figures and inverse pole figures derived from the ODF.

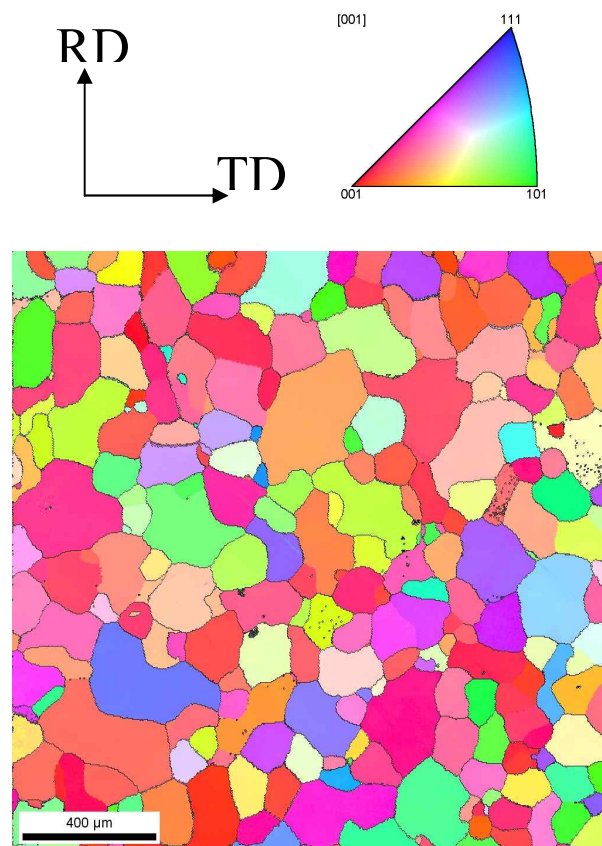


Fig. 4.2 Grain structure map derived from EBSD measurements of AA5052 before compression. Colors correspond to the orientations shown above the map.

## 4. Texture Formation in AA5052 Alloy under Uniaxial Compression at High Temperatures

### 4.3 Results

#### 4.3.1 Stress – strain curves

Figure 4.3 shows the true stress–true strain curves for the deformation of AA5052 alloy under the conditions described in section 4.2. High-temperature yielding phenomena are observed in all cases, and the flow stresses increased with decreasing temperature and increasing strain rate. In Fig. 4.3(c), the cyan dotted line shows the results for binary Al–3mass%Mg deformed at 723 K and  $5.0 \times 10^{-4} \text{ s}^{-1}$  [4]. As shown in Table 2.1, the Mg concentration of AA5052 alloy is close to 2.6mass%. The flow stress of AA5052 alloy is higher than that of Al–3mass%Mg alloy under the same deformation conditions.

#### 4.3.2 Texture formation

Figure 4.4 shows  $\{011\}$  pole figures after deformation at 823 K and 773 K. The pole density is projected onto the compression plane. The pole density shows a concentric circular distribution in all cases, indicating the formation of fiber textures. For all cases, higher pole densities appear in the center and the area about  $45^\circ$  from the center. However, the intensity of the pole density and its distribution vary with the deformation conditions. Figure 4.5 shows  $\{011\}$  pole figures after deformation at 673 K and 723 K. The pole density shows a concentric circular distribution in all cases except Fig. 4.5(a). High pole density appears in the center and in the area about  $60^\circ$  away from the center in all cases except Fig. 4.5(a).

The area of higher pole density in Fig. 4.4(a) appears at about 35 degrees away from the center, whereas that in Fig. 4.5(b) appears at the center and about 60 degrees away from the center. Thus, the texture is different in AA5052 alloy when it was deformed at the same strain rate but different temperatures. To clarify the texture component for all cases, the main component of the fiber texture was examined on the basis of the ODF.

#### 4. Texture Formation in AA5052 Alloy under Uniaxial Compression at High Temperatures

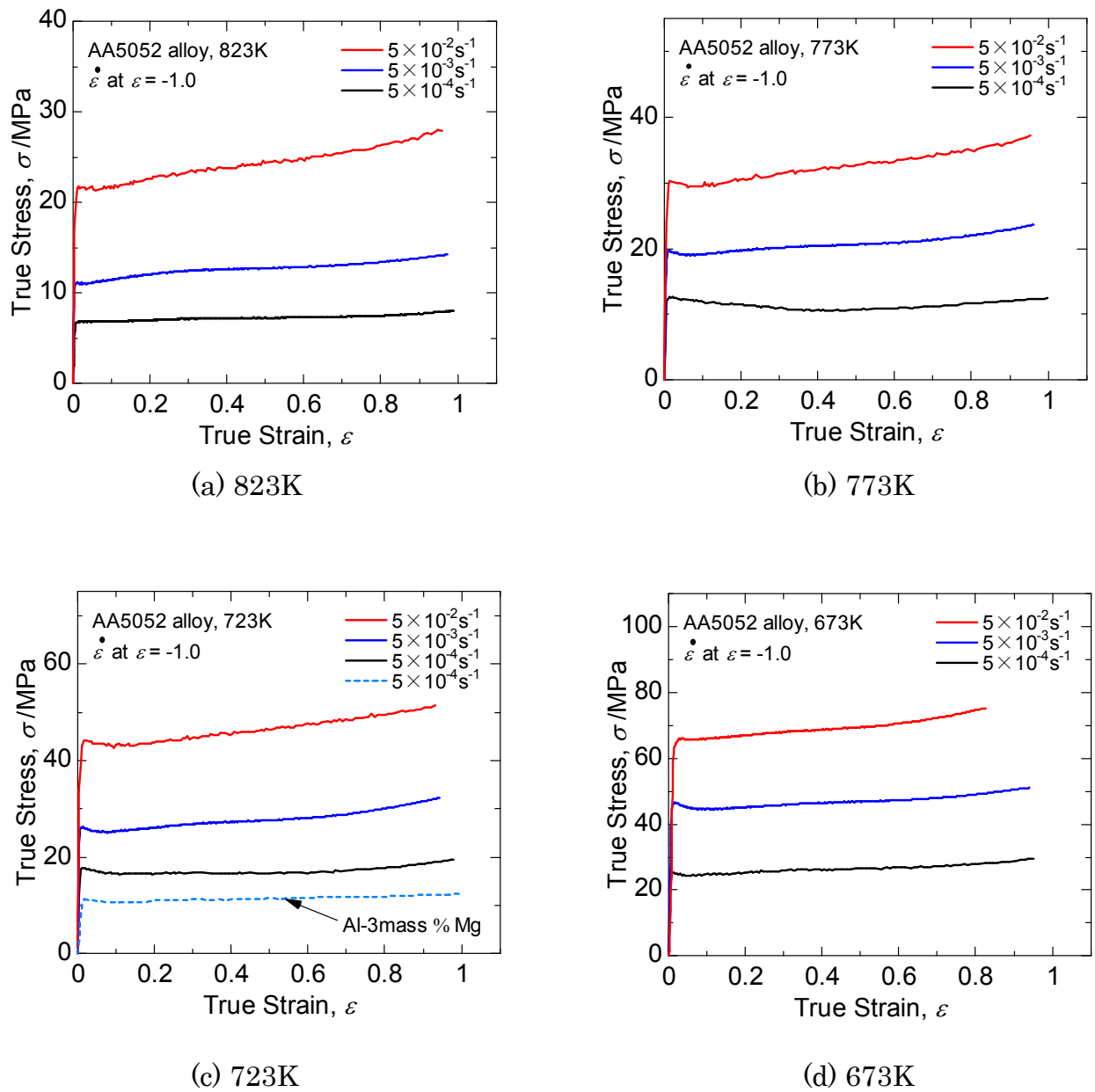


Fig. 4.3 True stress–true strain curves of AA5052 alloy obtained by compression tests up to a true strain of  $-1.0$  at various strain rates. Deformation temperatures are (a) 823 K, (b) 773 K, (c) 723 K, and (d) 673 K. Results for Al-3mass%Mg deformed at 723 K and  $5.0 \times 10^{-4} \text{ s}^{-1}$  [4] are also shown in (c).

#### 4. Texture Formation in AA5052 Alloy under Uniaxial Compression at High Temperatures

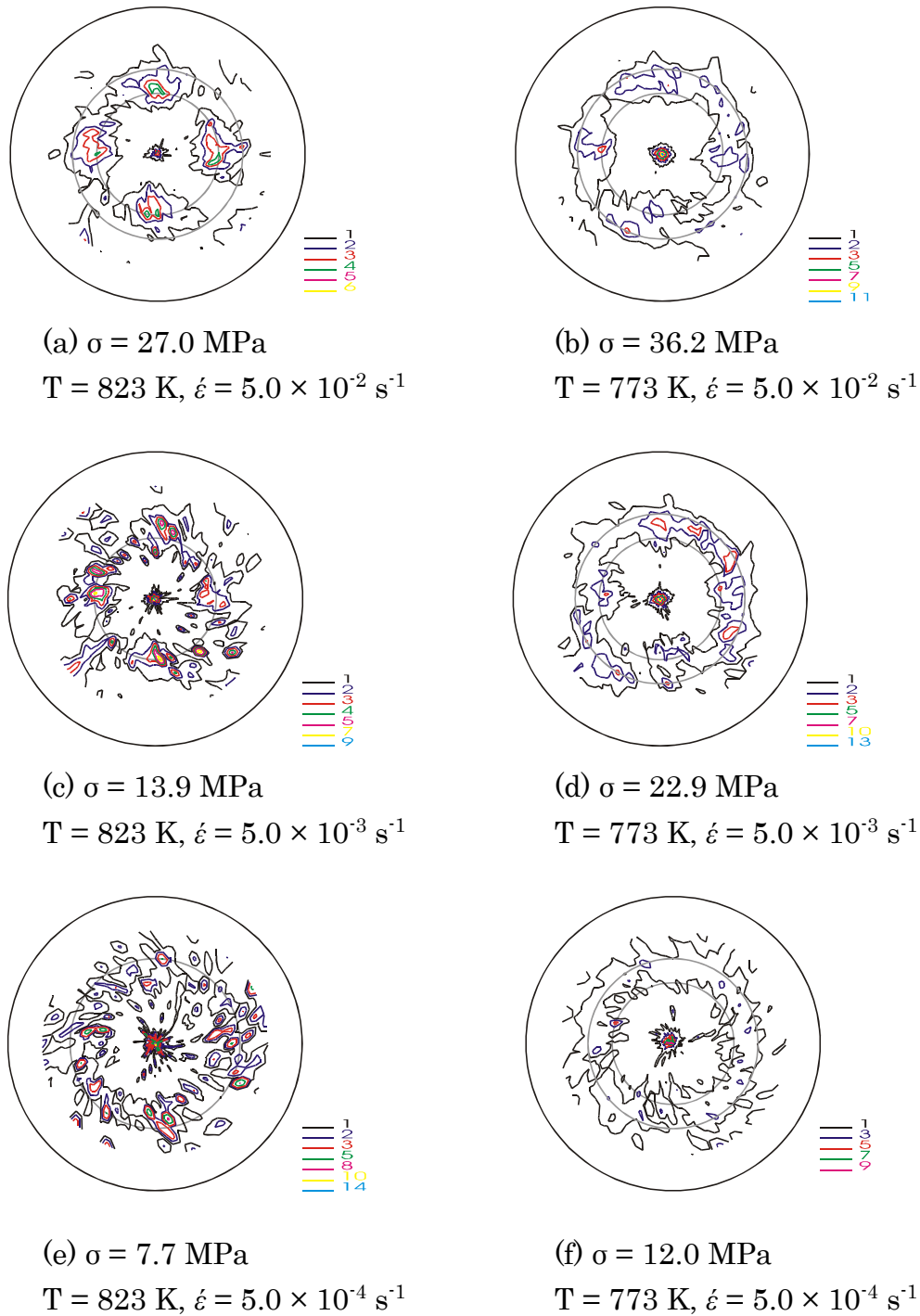


Fig. 4.4  $\{011\}$  pole figures after deformation at 823 K and 773 K at various strain rates up to a true strain of  $-1.0$ . Pole density is projected onto the compression plane. Contour lines represent intervals in units of average pole density. Gray circles correspond to  $45^\circ$  and  $60^\circ$  from the center.

#### 4. Texture Formation in AA5052 Alloy under Uniaxial Compression at High Temperatures

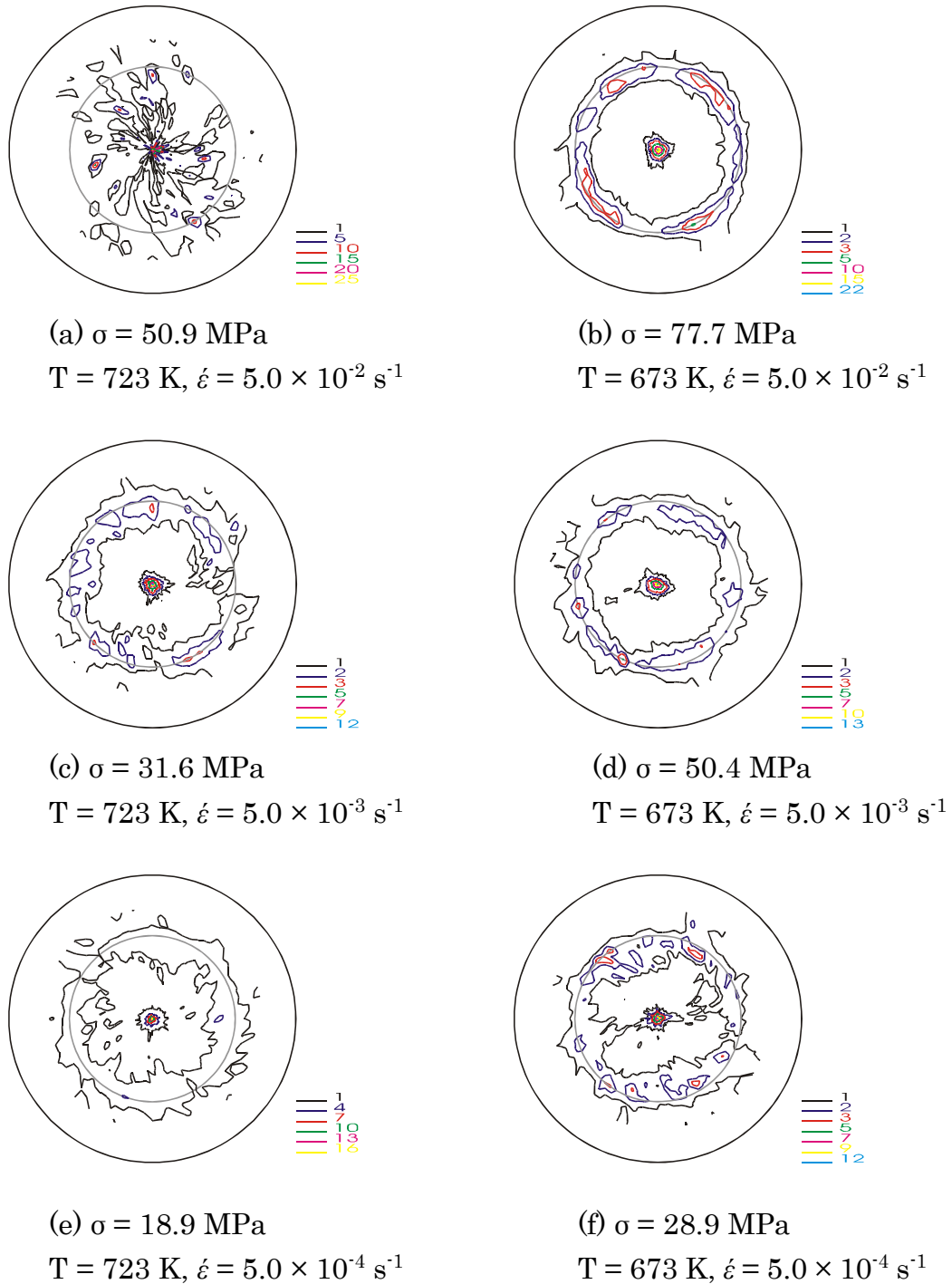
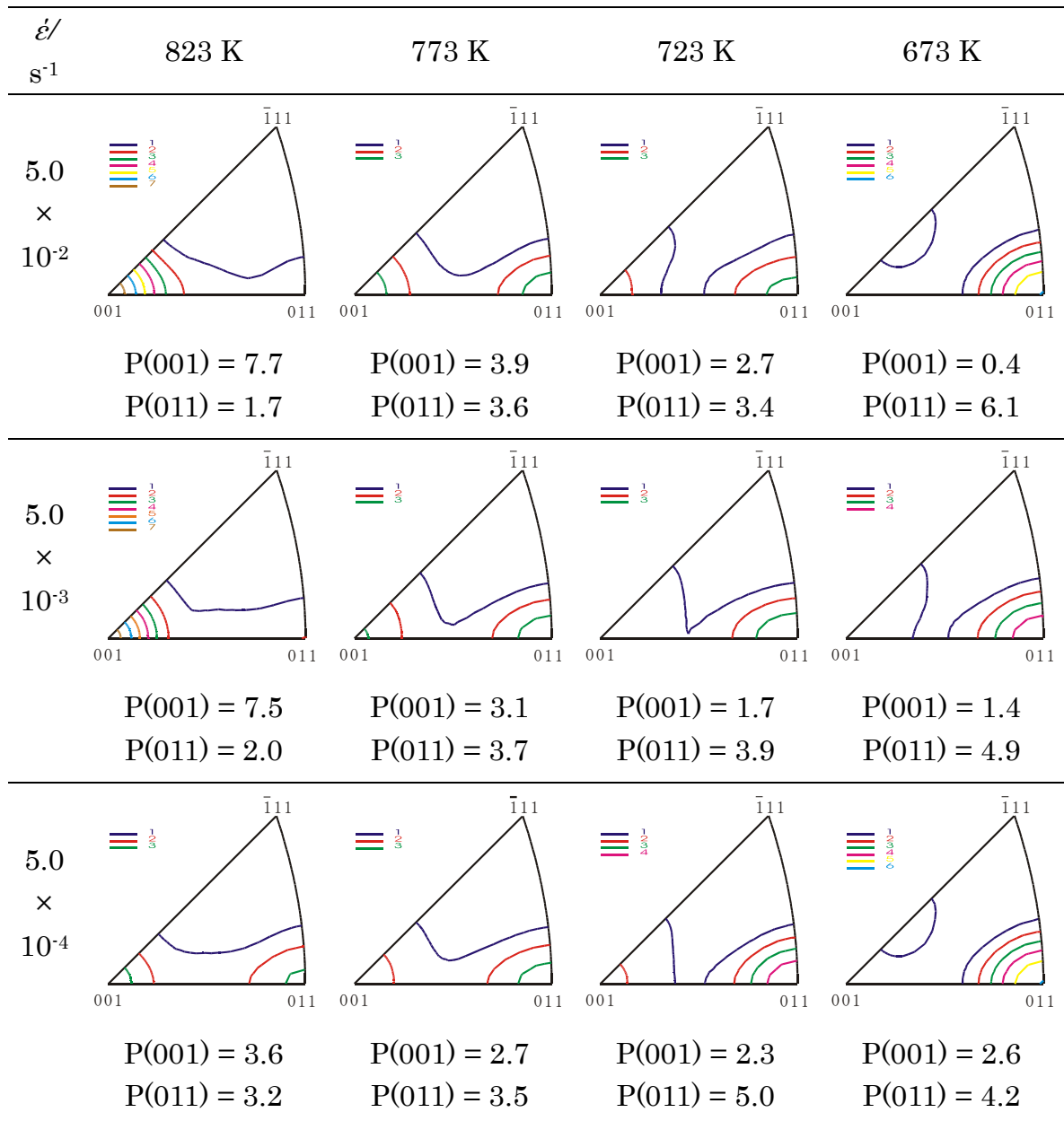


Fig. 4.5  $\{011\}$  pole figures after deformation at 723 K and 673 K and various strain rates up to a true strain of  $-1.0$ . Pole density is projected onto the compression plane. Contour lines represent intervals in units of average pole density.

#### 4. Texture Formation in AA5052 Alloy under Uniaxial Compression at High Temperatures

Table 4.1 Inverse pole figures for specimens compressed at various temperatures and strain rates up to a true strain of  $-1.0$ . Contour lines represent intervals of average pole density.  $P(001)$  and  $P(011)$  are the pole densities at (001) and (011), respectively.



#### 4. Texture Formation in AA5052 Alloy under Uniaxial Compression at High Temperatures

Table 4.1 shows inverse pole figures for the specimens after compression. The main texture component changes from  $\{011\}$  to  $\{001\}$  with increasing temperature at the same strain rate. At a strain rate of  $5.0 \times 10^{-2} \text{ s}^{-1}$ , for example, the pole density at (001) increases from 0.4 to 7.7 when the temperature increases from 673 K to 823 K. This tendency is also seen at the other strain rates. This means that the main texture component and the sharpness of the  $\{001\}$  texture vary with the temperature.

##### 4.3.3 Grain structures

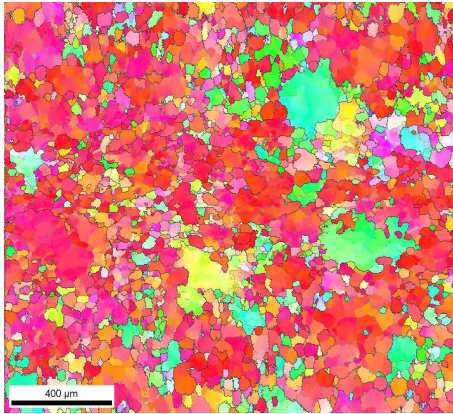
Figures 4.6–4.8 show grain structure maps of the compression plane of the specimens after compression. The maps were constructed using EBSD measurements on the mid-plane section. Where the minimum rotation angle between neighboring points of measurements is larger than  $15^\circ$ , grain boundaries are shown by black lines. Low-angle grain boundaries (misorientation angles between  $5^\circ$  and  $15^\circ$ ) are shown by thin gray lines.

Figure 4.6 shows grain structure maps of specimens deformed at various temperatures and a strain rate of  $5.0 \times 10^{-2} \text{ s}^{-1}$ . In Fig. 4.6(a), the microstructure consists of large grains of  $\{001\}$  orientation and small  $\{011\}$  grains. This is consistent with the fact that the pole density at (001) is 7.7 times the random level, as shown in Table 4.1. As the temperature decreases, the area fraction of grains with the  $\{001\}$  orientation decreases, and  $\{011\}$  grains develop [Fig. 4.6(a)–(d)]. In Fig. 4.6(d), the grains with the  $\{011\}$  orientation are much larger than those with other orientations.

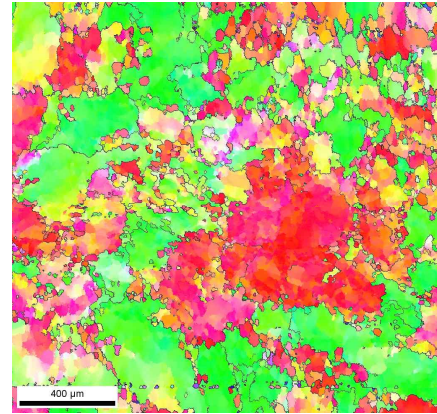
Figure 4.7 shows grain structure maps of specimens compressed at various temperatures and a strain rate of  $5.0 \times 10^{-3} \text{ s}^{-1}$ . A transition of the main component from  $\{001\}$  to  $\{011\}$  with decreasing temperature is seen here as well. Unlike Figs. 4.6 and 4.7, Fig. 4.8 shows that the microstructure of specimens deformed at various temperatures and a strain rate of  $5.0 \times 10^{-4} \text{ s}^{-1}$  consists of large grains with the  $\{001\}$  and  $\{011\}$  orientations. Figure 4.8(b)–(d) show that the main component did not depend on the temperature.



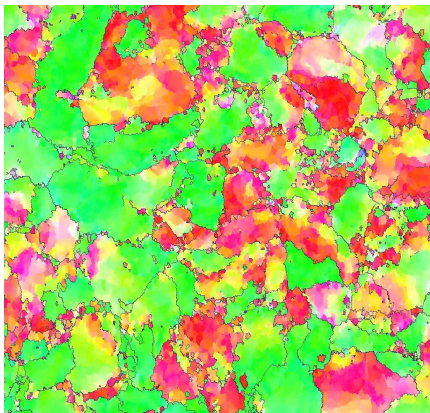
#### 4. Texture Formation in AA5052 Alloy under Uniaxial Compression at High Temperatures



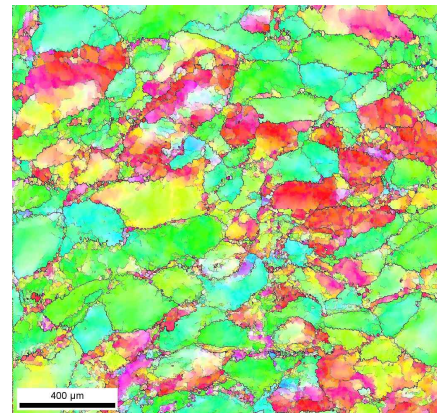
(a)  $T = 823 \text{ K}$ ,  $\dot{\epsilon} = 5.0 \times 10^{-2} \text{ s}^{-1}$



(b)  $T = 773 \text{ K}$ ,  $\dot{\epsilon} = 5.0 \times 10^{-2} \text{ s}^{-1}$



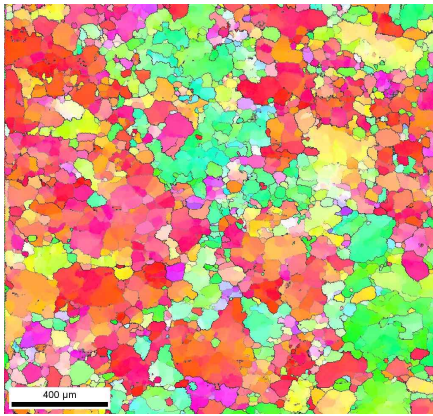
(c)  $T = 723 \text{ K}$ ,  $\dot{\epsilon} = 5.0 \times 10^{-2} \text{ s}^{-1}$



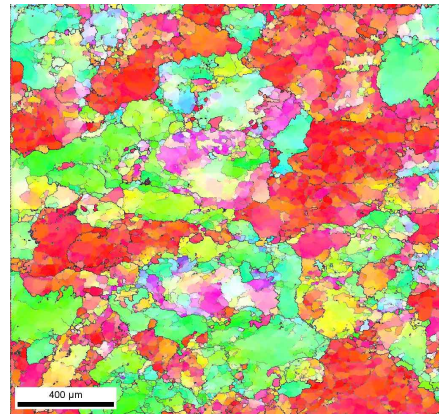
(d)  $T = 673 \text{ K}$ ,  $\dot{\epsilon} = 5.0 \times 10^{-2} \text{ s}^{-1}$

Fig. 4.6 Grain structure maps derived from EBSD measurements of AA5052 compressed at (a) 823 K, (b) 773 K, (c) 723 K, and (d) 673 K at a strain rate of  $5.0 \times 10^{-2} \text{ s}^{-1}$  up to a true strain of  $-1.0$ . Grain colors correspond to the orientations given in Fig. 4.1. Black lines represent high-angle grain boundaries with misorientation angles ( $\theta$ ) greater than  $15^\circ$ . Thin gray lines represent low-angle grain boundaries with  $\theta$  between  $5^\circ$  and  $15^\circ$ .

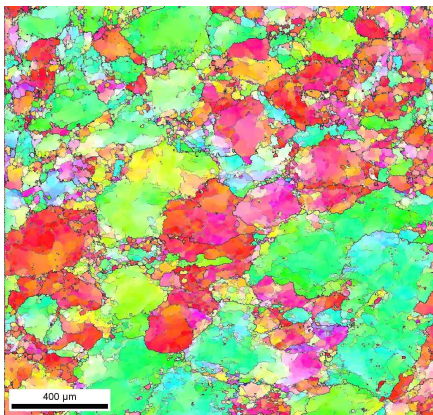
#### 4. Texture Formation in AA5052 Alloy under Uniaxial Compression at High Temperatures



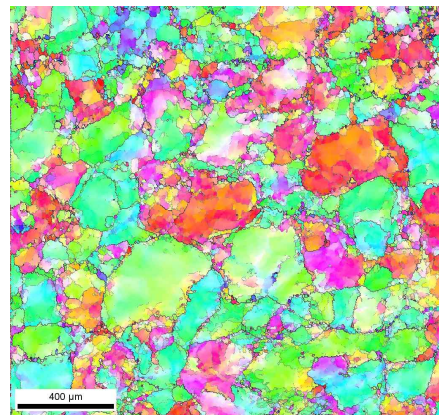
(a)  $T = 823 \text{ K}$ ,  $\dot{\epsilon} = 5.0 \times 10^{-3} \text{ s}^{-1}$



(b)  $T = 773 \text{ K}$ ,  $\dot{\epsilon} = 5.0 \times 10^{-3} \text{ s}^{-1}$



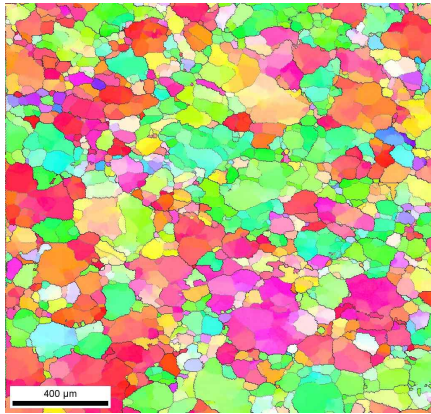
(c)  $T = 723 \text{ K}$ ,  $\dot{\epsilon} = 5.0 \times 10^{-3} \text{ s}^{-1}$



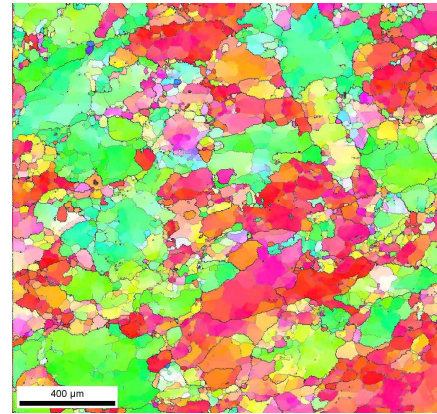
(d)  $T = 673 \text{ K}$ ,  $\dot{\epsilon} = 5.0 \times 10^{-3} \text{ s}^{-1}$

Fig. 4.7 Grain structure maps derived from EBSD measurements of AA5052 compressed at (a) 823 K, (b) 773 K, (c) 723 K and (d) 673 K at a strain rate of  $5.0 \times 10^{-3} \text{ s}^{-1}$  up to a true strain of  $-1.0$ . Grain colors correspond to the orientations given in Fig. 4.1. Black lines represent high-angle grain boundaries with misorientation angles ( $\theta$ ) greater than  $15^\circ$ . Thin gray lines represent low-angle grain boundaries with  $\theta$  between  $5^\circ$  and  $15^\circ$ .

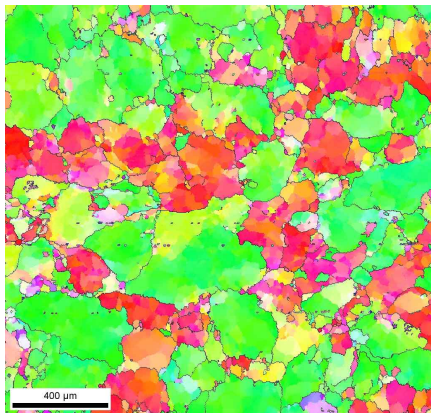
#### 4. Texture Formation in AA5052 Alloy under Uniaxial Compression at High Temperatures



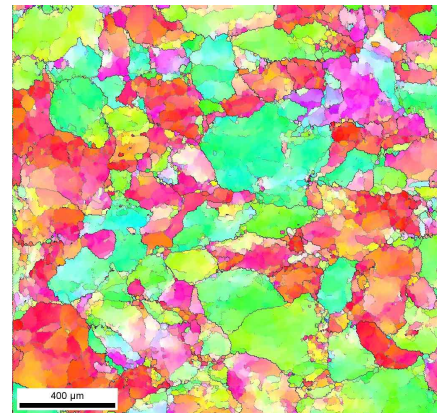
(a)  $T = 823 \text{ K}$ ,  $\dot{\epsilon} = 5.0 \times 10^{-4} \text{ s}^{-1}$



(b)  $T = 773 \text{ K}$ ,  $\dot{\epsilon} = 5.0 \times 10^{-4} \text{ s}^{-1}$



(c)  $T = 723 \text{ K}$ ,  $\dot{\epsilon} = 5.0 \times 10^{-4} \text{ s}^{-1}$



(d)  $T = 673 \text{ K}$ ,  $\dot{\epsilon} = 5.0 \times 10^{-4} \text{ s}^{-1}$

Fig. 4.8 Grain structure maps derived from EBSD measurements of AA5052 compressed at (a) 823 K, (b) 773 K, (c) 723 K, and (d) 673 K at a strain rate of  $5.0 \times 10^{-4} \text{ s}^{-1}$  up to a true strain of  $-1.0$ . Grain colors correspond to the orientations given in Fig. 4.1. Black lines represent high-angle grain boundaries with misorientation angles ( $\theta$ ) greater than  $15^\circ$ . Thin gray lines represent low-angle grain boundaries with  $\theta$  between  $5^\circ$  and  $15^\circ$ .

## 4. Texture Formation in AA5052 Alloy under Uniaxial Compression at High Temperatures

### 4.4 Discussion

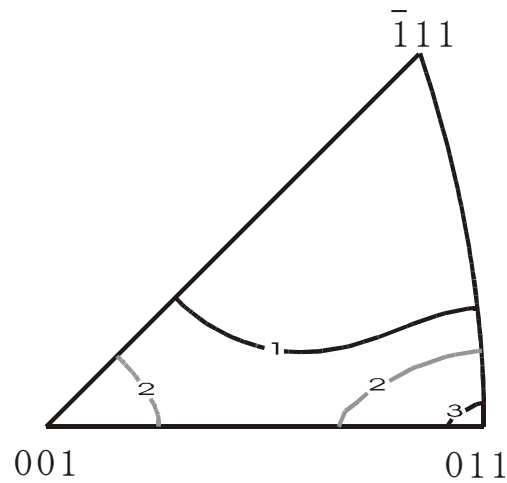
#### 4.4.1 Texture formation process in AA5052 alloys

As explained in chapter 3, the dominant formation mechanism of {001} texture in binary Al–Mg alloys is grain boundary migration under specific deformation conditions at high temperatures. Okayasu and Fukutomi [4] investigated texture formation during high-temperature deformation of Al–3Mg and Al–3Mg–0.2Sc alloys. They found that the formation of {001} texture in Al–3Mg–0.2Sc alloy was remarkably retarded by the presence of Al<sub>3</sub>Sc precipitates. This suggests that grain boundary migration contributes to the development of {001} texture. As shown in Table 4.1, the pole density at {001} increases from 0.4 (673 K) to 7.7 (823 K) times the random level at a strain rate of  $5.0 \times 10^{-2} \text{ s}^{-1}$ . This can be understood if the preferential growth of {001} grains by grain boundary migration drives the development of {001} texture. The microstructures shown in Fig. 4.6(a) and (d) support this supposition: {001} grains grow by consuming {011} grains.

As shown in Table 2.1, AA5052 contains about 2.5mass%Mg. The effect of the elements in 5xxx series alloys on the development of {001} texture was discussed in section 3.4.1 by comparing AA5182 with binary Al–5mass%Mg alloys. Figure 4.9 shows the inverse pole figure for the compression plane of Al–3mass%Mg compressed at 723 K and a strain rate of  $5.0 \times 10^{-4} \text{ s}^{-1}$  up to a true strain of  $-1.0$ . A comparison of Fig. 4.9 with Table 4.1 shows that the pole density at (001) for the commercial AA5052 alloy is lower than that of the binary Al–3Mg alloy. This suggests that alloy elements other than aluminum and magnesium in commercial aluminum alloys may suppress grain boundary migration.

A comparison of Table 3.2 with Table 4.1 shows that the sharpness of {001} texture in AA5182 is enhanced by an increase in the Mg concentration under the same deformation conditions. For example, the pole density of AA5182 deformed at 823 K and a strain rate of  $5.0 \times 10^{-2} \text{ s}^{-1}$  up to a true strain of  $-1.0$  is 12 times the random level, whereas that of AA5052 is 7.5 times the random level under the same deformation conditions. This tendency coincides with the experimental results reported by Okayasu and Fukutomi [1].

#### 4. Texture Formation in AA5052 Alloy under Uniaxial Compression at High Temperatures



Al-3mass%Mg  
723 K,  $5.0 \times 10^{-4} \text{ s}^{-1}$   
 $P(001) = 2.8$ ,  $P(011) = 3.1$

Fig. 4.9 Inverse pole figure for compression plane of Al-3mass%Mg [4] deformed at 723 K at a strain rate of  $5.0 \times 10^{-4} \text{ s}^{-1}$  up to a strain of -1.0. Contour lines represent intervals in units of average pole density.

Nakashima and Yoshinaga [5] investigated the mobility of edge dislocation in Al-Mg solid solution alloys at high temperatures. They reported that the mobility of edge dislocation decreases exponentially in aluminum alloys containing higher solute concentrations. Thus, the solute atoms are believed to retard the formation of subgrains in the crystal grains, enhancing the orientation dependence of the stored energy and accelerating the growth of grains with the {001} orientation.

#### 4.4.2 Development of {001} texture

As shown in Table 4.1, {011} texture develops at 723 K and a strain rate of  $5.0 \times 10^{-3} \text{ s}^{-1}$  in AA5052 alloy. At 823 K, the main texture component is not {011} but {001} at a true strain of -1.0. Therefore, the dominant deformation

#### 4. Texture Formation in AA5052 Alloy under Uniaxial Compression at High Temperatures

mechanism might be different for these two textures.

Otsuka and Horiuchi [6] investigated the stability of crystal orientation using Al–3mol%Mg single crystals at various orientations. They found that the {001} orientation is stable under high-temperature deformation. They also found that the solute atoms inhibited the formation of subgrains owing to the effect of the Cottrell atmosphere [7,8]. In this case, the orientation dependence of stored energy is considered to be enhanced compared with the case in which subgrains formed. Grains having a low Taylor factor may have lower stored energy than those having higher Taylor factors. The Taylor factors for {001}- and {011}-oriented grains were reportedly 2.449 and 3.674, respectively [9]. As a result, the {001} texture can be understood as developing by consuming other texture components by grain boundary migration because of the low stored energy and orientation stability.

To confirm the development of the {001} component by grain boundary migration, the relationship between flow stress and mean grain size was examined, as shown in Fig. 4.10.

The mean grain sizes of two types of grain are investigated: {001} grains and all grains. Grains smaller than 10  $\mu\text{m}$  were omitted from the evaluation of mean grain size. The mean grain sizes for {001} grains and all grains decrease with increasing flow stress. The mean grain size of all grains is smaller than that of {001} grains at all stress levels. These results suggest that the development of {001} texture can be attributed to grain boundary migration.

##### 4.4.3 {001} texture maps of AA5052 and AA5182 alloys

As mentioned in chapter 3 and this chapter, the deformation temperature, strain rate, strain, and solute concentration affect texture formation in AA5052 and AA5182 commercial aluminum alloys. To elucidate the relationship between texture formation and deformation conditions, the pole densities are plotted as a function of strain rate and temperature on the (001) plane of AA5052 and AA5182 alloys in Fig. 4.11. The vertical and horizontal axes are the strain rate and the reciprocal of the absolute temperature, respectively.

#### 4. Texture Formation in AA5052 Alloy under Uniaxial Compression at High Temperatures

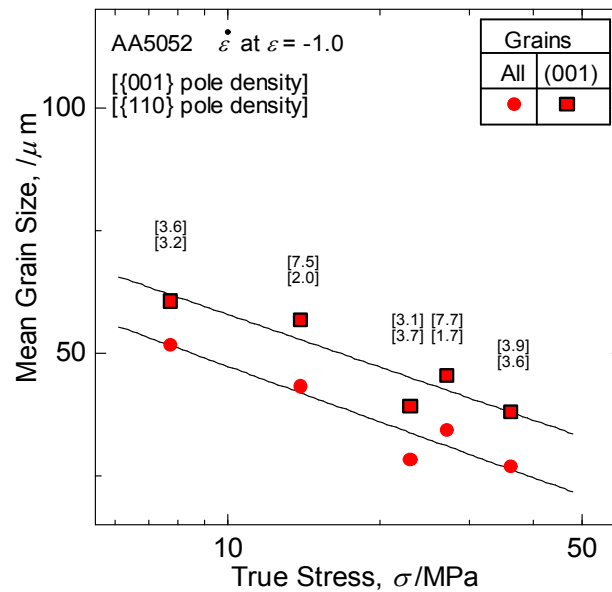


Figure 4.10 Relationship between flow stress at a true strain of  $-1.0$  and mean grain sizes for  $\{001\}$  grains and all grains.

In AA5052 alloy, higher pole densities at  $\{001\}$  appear in the higher strain rate region at 823 K. Under a constant stress of 20 MPa, the  $\{001\}$  pole densities increase from 2.3 to 3.1 and then to 7.5 times the random level. Similarly, at 20 MPa, the  $\{001\}$  pole densities in AA5182 alloy also increased from 4.4 to 9.9 and then to 12 times the random level. The same tendency can be seen at 40 MPa in both alloys. These results demonstrate that if the stress level is the same, a higher temperature yields a sharper  $\{001\}$  texture. Moreover, a higher grain boundary mobility contributes to the development of  $\{001\}$  texture in both alloys. Comparison of these two  $\{001\}$  texture maps shows that the pole densities and sharpnesses at  $\{001\}$  in AA5182 alloy are higher than those for AA5052 alloy. This suggests that the sharpness of  $\{001\}$  texture depends on not only the strain rate and deformation temperature but also the solute concentration.

#### 4. Texture Formation in AA5052 Alloy under Uniaxial Compression at High Temperatures

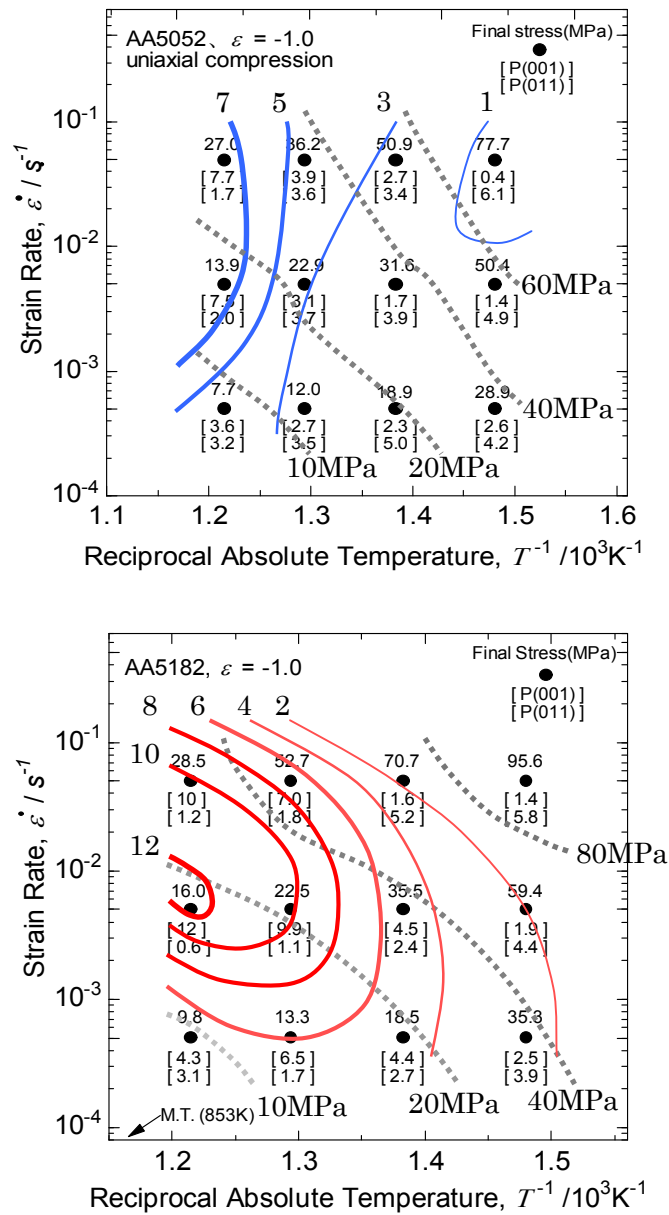


Fig. 4.11  $\{001\}$  texture maps at a true strain of  $-1.0$  for AA5052 (upper) and AA5182 (lower) aluminum alloys showing the effect of strain rate and temperature on the development of  $\{001\}$  texture. Solid circles indicate deformation conditions; numbers below them give the pole density at  $\{001\}$  in the inverse pole figures. Contours for the pole densities at  $\{001\}$  appear as blue or red lines. Broken lines represent deformation conditions under the same flow stress.



#### 4. Texture Formation in AA5052 Alloy under Uniaxial Compression at High Temperatures

##### 4.5 Conclusions

To explore the texture formation process during high-temperature deformation of AA5052 alloy, uniaxial compression deformation was conducted at various temperatures and strain rates. The major results are summarized as follows.

- (1) In AA5052 commercial alloy, the main component of the fiber texture depends on the deformation conditions.
- (2) When {001} texture develops, the mean size of {001} grains is larger than that of all grains in both alloys. This suggests that {001} texture formation is caused by grain boundary migration.
- (3) The pole densities at (001) in AA5052 alloy are much weaker than those in binary alloys with similar solute concentrations under the same deformation conditions. This might be due to the suppression of grain boundary migration.
- (4) For the same deformation conditions, the pole densities at (001) in AA5182 are higher than those in AA5052 alloy.

## References

- [1] K. Okayasu and H. Fukutomi: *J. Japan Inst. Metals* **73** (2009) pp. 58–63.
- [2] R. Horiuchi, H. Yoshinaga and S. Hama: *J. Japan Inst. Metals* **29** (1971) pp. 406–415.
- [3] M. Dahms and H. J. Bunge: *J. Appl. Crystallogr.* **22** (1989) pp. 439–447.
- [4] K. Okayasu and H. Fukutomi: *J. Japan Inst. Metals* **70** (2006) pp. 562–567.
- [5] H. Nakashima and H. Yoshinaga: *J. Japan Inst. Metals* **56** (1992) pp. 254–261.
- [6] M. Otsuka and R. Horiuchi: *J. Japan Inst. Metals* **36** (1972) pp. 809–817.
- [7] A. H. Cottrell and M. A. Jaswon: *Proc. Roy. Soc. A*.**199** (1949) pp. 104–114.
- [8] R. Horiuchi, H. Yoshinaga and S. Hama: *Trans. Japan Inst. Metals* **6** (1965) pp. 123–130.
- [9] G. Y. Chin and W. L. Mammel: *Trans. Metall. AIME* **239** (1967) pp. 1400–1405.

## Chapter 5

# Effect of Texture on the Bending Workability of AA5182 Alloy

### 5.1 Introduction

Reducing the weight of automobiles through the use of commercial aluminum alloys is of great interest owing to concerns about improving fuel economy while maintaining structural strength. Improving the workability of aluminum alloys is crucial to promoting their application in a wide range of fields. As described in chapter 1, controlling the texture is important for practical application of aluminum alloys.

Takeda et al. [1] have reported on the relationship between the crystal orientation and bendability of an Al–Mg–Si alloy. They examined the bending workability of a number of single crystal specimens with various orientations on the surface [1]. They found that material having a cube orientation has the best bend workability. Other studies have discussed the relationship between the bendability and the Taylor factor. The bendability is reportedly also related to the formation of shear bands upon bending [2-4].

The {001} (compression) texture formation process in AA5182 commercial aluminum alloy is described in chapter 3. It was concluded that {001}, {001} + {011}, and/or {011} texture form depending on the temperature, strain, and strain rate. On the basis of the results given in chapter 3, specimens with cube texture were prepared by plane strain compression, and the effect of texture on bendability in AA5182 alloy was experimentally investigated.

### 5.2 Experimental procedure

AA5182 aluminum alloy was produced by Furukawa-Sky Aluminum Corp. in the form of 70% hot rolled plate 20 mm thick. Rectangular specimens with dimensions of 15 × 15 × 10 mm (height × width × length) were prepared by spark erosion machining for plane compression tests. The specimens were annealed at 843 K for 1000 min and at 773 K for 50 min in air before water quenching. Since the quench from 843 K caused small deformations in some cases, further annealing at 773 K was conducted.

Plane strain compression tests were conducted in air under a constant cross-head speed at 823 K and strain rates of  $5.0 \times 10^{-3} \text{ s}^{-1}$  or  $5.0 \times 10^{-4} \text{ s}^{-1}$  up

## 5. Effect of Texture on the Bending Workability of AA5182 Alloy

to true strains of  $-0.6$ ,  $-1.0$ , and  $-1.3$ . Unless otherwise indicated, all results reported below were obtained under these conditions.

As already described in detail in chapter 2, mid-plane sections of the deformed specimens were removed for texture measurements by mechanical and electrolytic polishing. Microstructures were observed using SEM. The bending test for AA5182 alloy was conducted by the V-block method.

### 5.3 Results

#### 5.3.1 Stress – strain curves

Figure 5.1 shows the true stress–true strain curves for plane strain compression of the specimens. The flow stress in Fig. 5.1(b) for a specimen deformed at  $5.0 \times 10^{-3} \text{ s}^{-1}$  is higher than that in Fig. 5.1(a) for a specimen deformed at  $5.0 \times 10^{-4} \text{ s}^{-1}$ . The curve for uniaxial compression shows high-temperature yielding, as shown in Fig. 3.2(a), whereas no obvious decrease in flow stress is seen under plane strain compression.

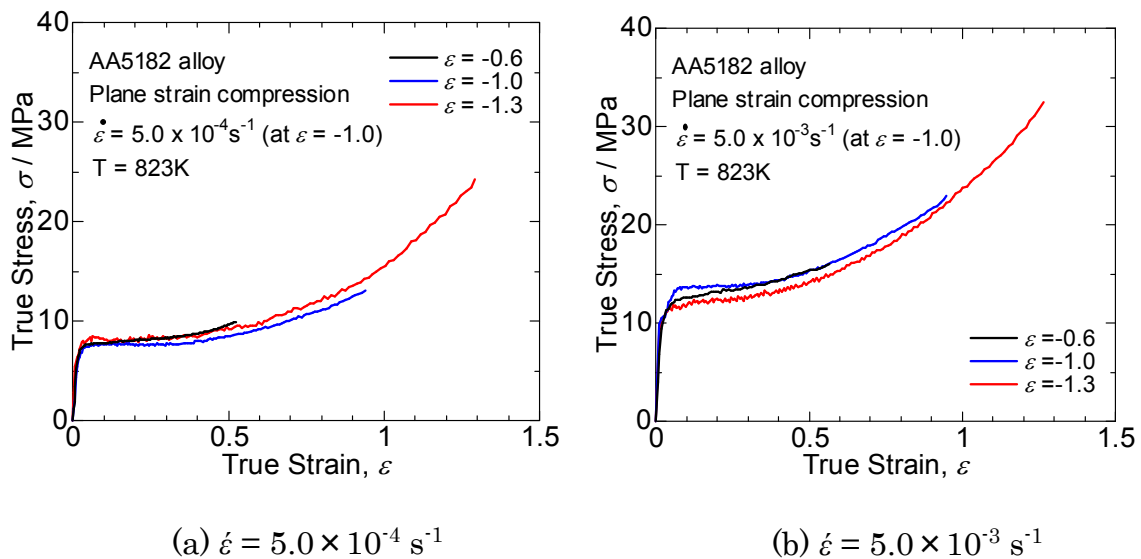


Fig. 5.1 True stress–true strain curves of AA5182 alloy obtained by plane strain compression tests at strain rates of (a)  $5.0 \times 10^{-3} \text{ s}^{-1}$  and (b)  $5.0 \times 10^{-4} \text{ s}^{-1}$  up to true strains of  $-0.6$ ,  $-1.0$ , and  $-1.3$ .

#### 5.3.2 Texture formation

## 5. Effect of Texture on the Bending Workability of AA5182 Alloy

Figure 5.2 shows  $\{111\}$  pole figures obtained after plane strain compression of the specimens up to a true strain of  $-1.3$ . The pole density is projected onto the compression plane. The contours represent intervals in units of average pole density. The high pole densities are distributed symmetrically in both cases. To identify the main component of the texture, inverse pole figures were constructed using the ODF.

Figures 5.3 and 5.4 show inverse pole figures for the compression planes of the specimens after plane strain compression at strain rates of  $5.0 \times 10^{-3} \text{ s}^{-1}$  and  $5.0 \times 10^{-4} \text{ s}^{-1}$ , respectively. In each figure, the true strains in panels (a), (b), and (c) are  $-0.6$ ,  $-1.0$ , and  $-1.3$ , respectively. At a strain rate of  $5.0 \times 10^{-4} \text{ s}^{-1}$  (Fig. 5.4), with increasing strain, the pole density at (001) increases from 1.7 to 7.0 times the random level, whereas that at (011) decreases from 1.6 to 0.3 times the random level. Moreover, at a rate of  $5.0 \times 10^{-3} \text{ s}^{-1}$  (Fig. 5.3), with increasing strain, the pole density at (001) increases from 5.3 to 10.4 times the random level, and that at (011) decreases from 1.1 to 0.3 times the random value.

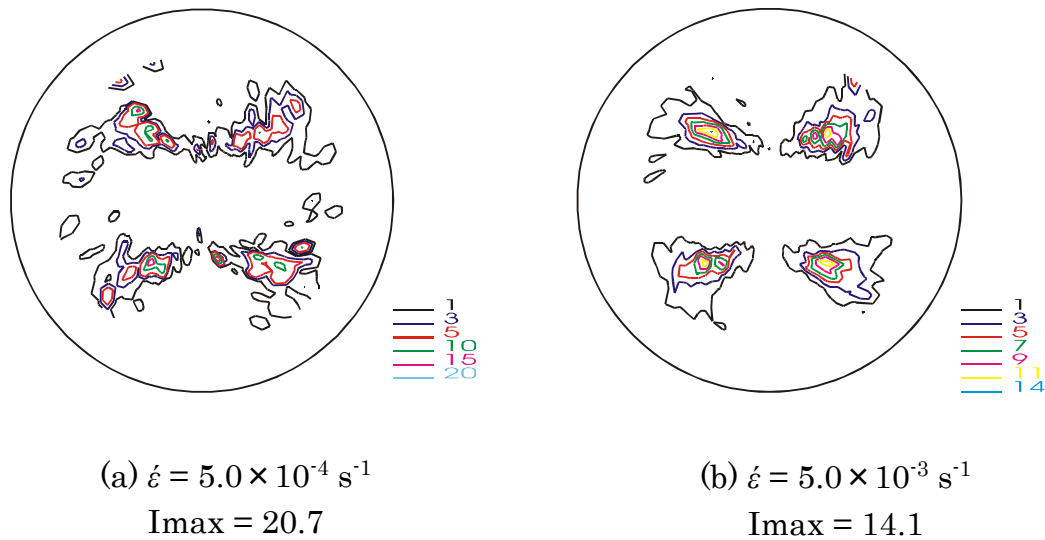


Fig. 5.2  $\{111\}$  pole figures after plane strain compression at 823 K and a strain rate of (a)  $5.0 \times 10^{-4} \text{ s}^{-1}$  and (b)  $5.0 \times 10^{-3} \text{ s}^{-1}$  up to a true strain of  $-1.3$ . Pole density is projected onto the compression plane. Contour lines represent intervals in units of average pole density.

## 5. Effect of Texture on the Bending Workability of AA5182 Alloy

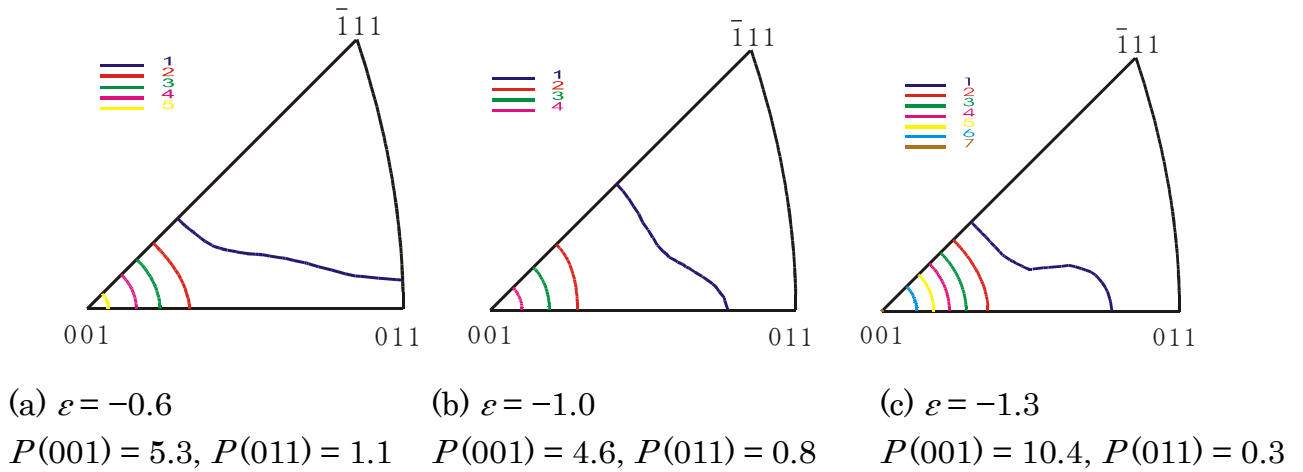


Fig. 5.3 Inverse pole figures for AA5182 after plane strain compression at 823 K and a strain rate of  $5.0 \times 10^{-3} \text{ s}^{-1}$  up to a true strain of (a)  $-0.6$ , (b)  $-1.0$ , and (c)  $-1.3$ . Contour lines represent intervals in units of average pole density.  $P(001)$  and  $P(011)$  represent the pole densities at (001) and (011), respectively.

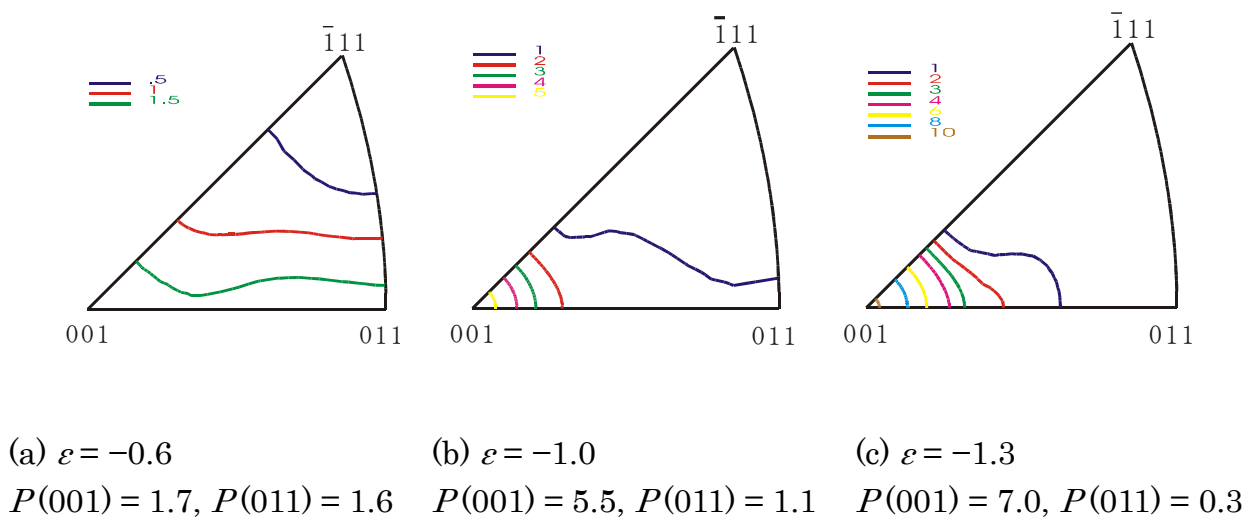


Fig. 5.4 Inverse pole figures for AA5182 after plane strain compression at 823 K and a strain rate of  $5.0 \times 10^{-4} \text{ s}^{-1}$  up to a true strain of (a)  $-0.6$ , (b)  $-1.0$ , and (c)  $-1.3$ . Contour lines represent intervals in units of average pole density.  $P(001)$  and  $P(011)$  represent the pole densities at (001) and (011), respectively.

## 5. Effect of Texture on the Bending Workability of AA5182 Alloy

Figure 5.5 shows the  $\varphi_2$  cross sections for the specimens after plane strain compression at a strain rate of  $5.0 \times 10^{-3} \text{ s}^{-1}$ . The  $\varphi_2$  values in Fig. 5.5(a)–(c) and (d)–(f) are  $0^\circ$  and  $45^\circ$ , respectively. An accumulation of orientation density is seen around  $\{001\}\langle 100 \rangle$ . A weak accumulation at  $\{011\}\langle 211 \rangle$  (brass orientation) also appears at strains of  $-0.6$  and  $-1.0$ . Cube orientation is the major component of texture independent of the strain. The density at  $\{001\}\langle 100 \rangle$  for  $\varphi_2 = 0^\circ$  is 12 times the random level at a strain of  $-0.6$ . At strains of  $-0.6$ ,  $-1.0$ , and  $-1.3$ , the density at  $\{001\}\langle 100 \rangle$  is 12, 17, and 40 times the random level, respectively. This increasing trend also appears in  $\varphi_2 = 45^\circ$ . Thus, sharp cube texture forms with increasing strain.

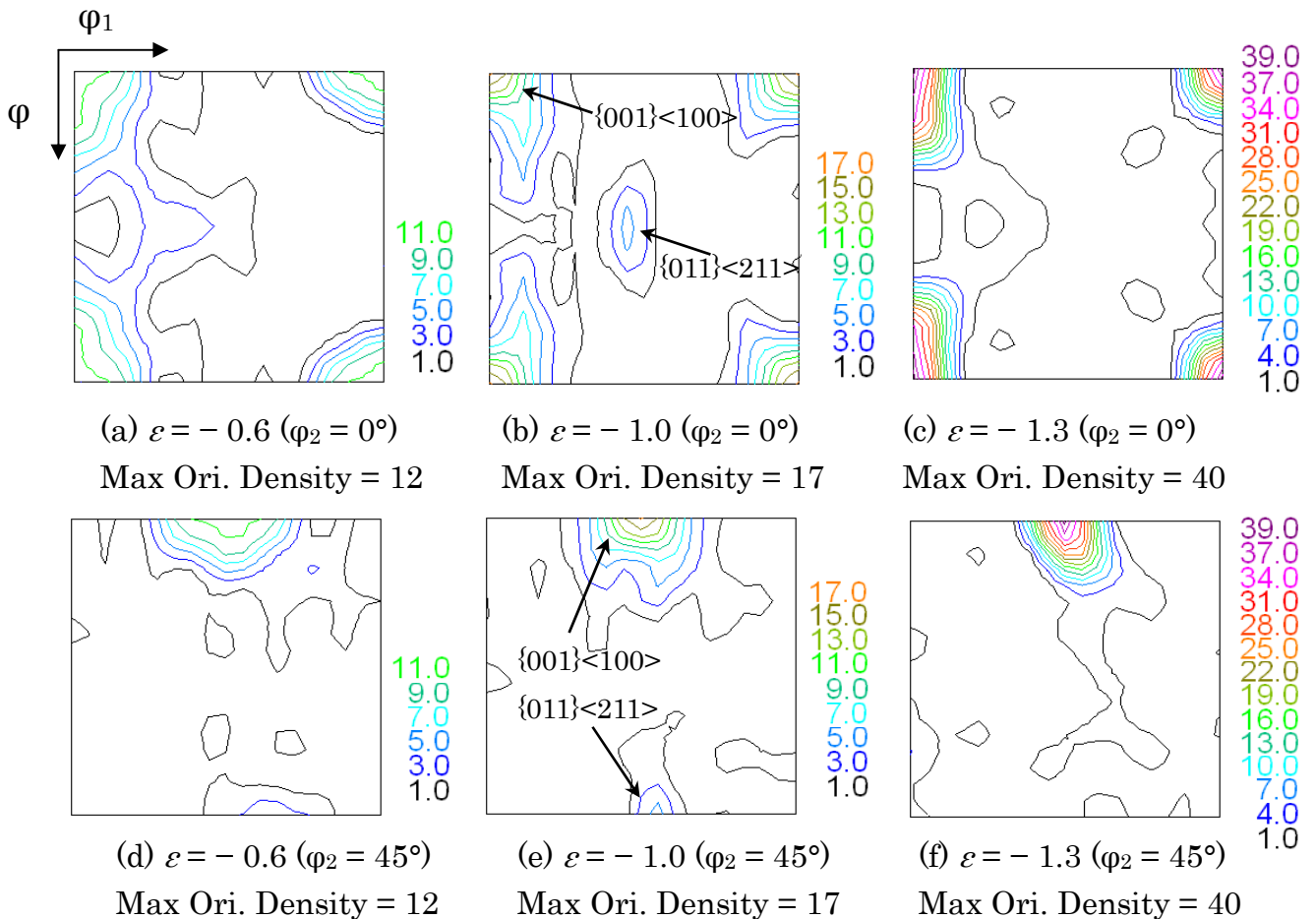


Fig. 5.5 Cross sections at (a)–(c)  $\varphi_2 = 0^\circ$  and (d)–(f)  $\varphi_2 = 45^\circ$  after plane strain compression at 823 K and a strain rate of  $5.0 \times 10^{-3} \text{ s}^{-1}$ . True strain is  $-0.6$ ,  $-1.0$ , or  $-1.3$ . “Max Ori. Density” is the maximum orientation density.



### 5.3.3 Grain structure maps

Figure 5.6 shows grain structure maps of the specimens after deformation. The maps represent measurements on the mid-plane sections. For both strain rates, the area fraction of  $\{001\}$  increases with increasing strain, whereas that for  $\{011\}$  decreases. The  $\{001\}$ -oriented grains seem to be larger than those with other orientations. The inverse pole figures corresponding to Fig. 5.6(c) and 5.6(f) in Fig. 5.3(c) and 5.4(c) show that the pole densities at (001) after deformation up to a strain of  $-1.3$  are 10.4 and 7.0 times the random level, respectively.

To examine the sharpness of the cube texture, the area fraction of cube orientation evaluated using the grain structure maps is given in Fig. 5.7. The grains with cube orientation within  $15^\circ$  of the  $\{001\}\langle 100\rangle$  orientation are shown in red. Grains with orientations close to cube orientation are shown in dark red. The deformation conditions of Fig. 5.7(a)–(f) correspond to those of Fig. 5.6(a)–(f). The black lines represent high-angle grain boundaries [misorientation angle ( $\theta$ ) of greater than  $15^\circ$ ]. At a strain of  $-0.6$ , the area fractions of cube orientation for the strain rates of  $5.0 \times 10^{-3} \text{ s}^{-1}$  and  $5.0 \times 10^{-4} \text{ s}^{-1}$  are 13% and 5% of the measured area, respectively. At a strain of  $-1.3$ , these rates increase to 54% and 51% of the measured area, respectively. As shown in Fig. 5.7(c), grains having cube texture are connected with each other. The sample shown in Fig. 5.7(c) was used for the bending test.

Figure 5.8 shows grain structure maps for the transverse direction (TD) plane obtained by EBSD for (a) an as-received specimen, (b) an annealed specimen, and (c) a specimen after plane strain compression at 823 K and a strain rate of  $5.0 \times 10^{-3} \text{ s}^{-1}$  up to a true strain of  $-1.3$ . Specimens for the bending test were prepared from the cut specimens shown in Fig. 5.8(a)–(c). Figure 5.8(d)–(g) show the grain structure maps of the specimens used for the bending test. The bottom planes of Fig. 5.8(d)–(g) are the bending surfaces. Figure 5.9 shows a schematic view of the method of preparing the bending test specimens, labeled the cube  $0^\circ$ , random  $0^\circ$ , cube  $90^\circ$ , and random  $90^\circ$  specimens.

## 5. Effect of Texture on the Bending Workability of AA5182 Alloy

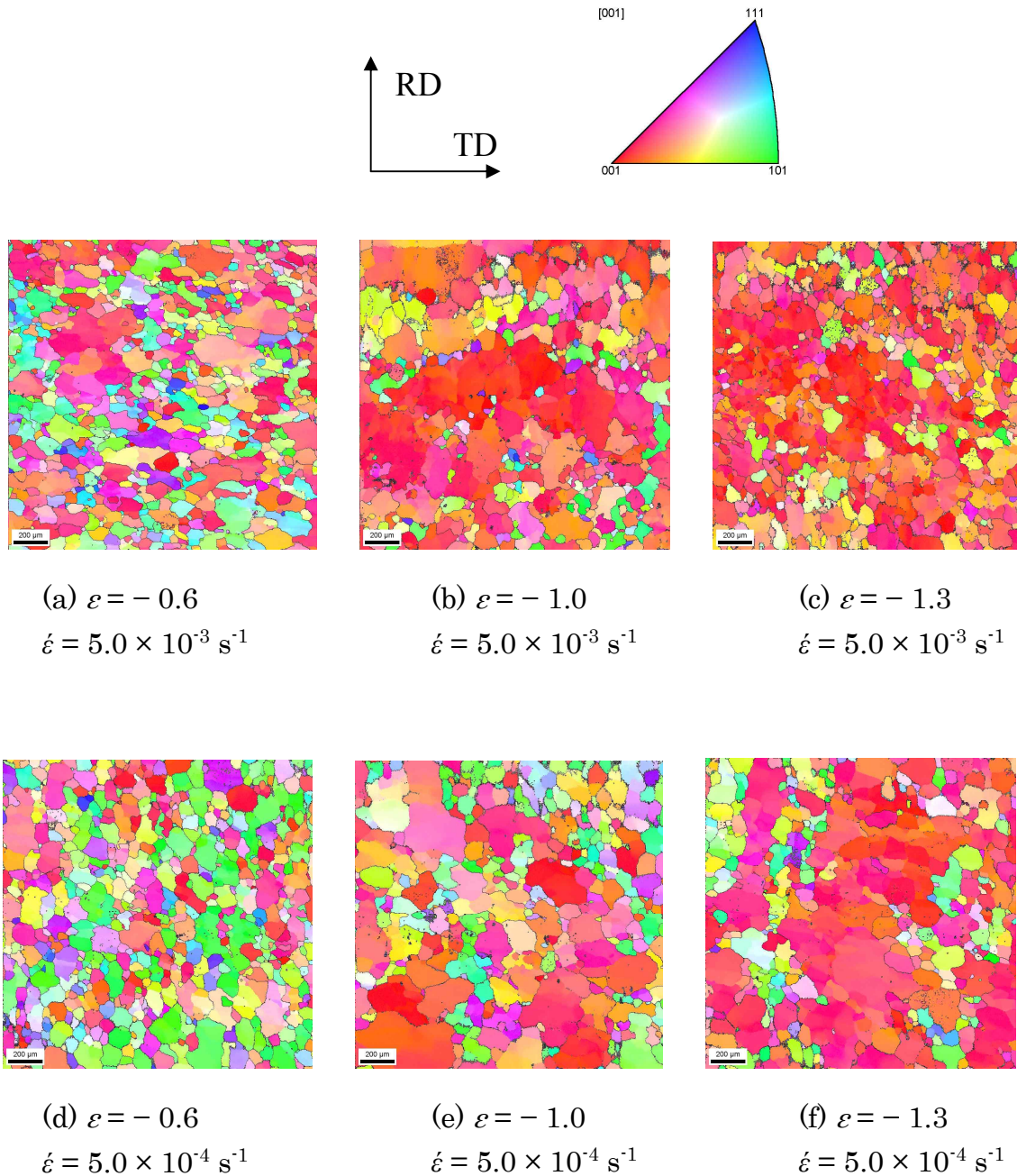


Fig. 5.6 Grain structure maps of AA5182 derived from EBSD measurements after plane strain compression at 823 K and strain rates of (a)–(c)  $5.0 \times 10^{-3} \text{ s}^{-1}$  and  $5.0 \times 10^{-4} \text{ s}^{-1}$  up to true strains of  $-0.6$ ,  $-1.0$ , and  $-1.3$ . Grain colors correspond to the orientations given above the map. Black lines represent high-angle grain boundaries with misorientation angles ( $\theta$ ) of greater than  $15^\circ$ .

## 5. Effect of Texture on the Bending Workability of AA5182 Alloy

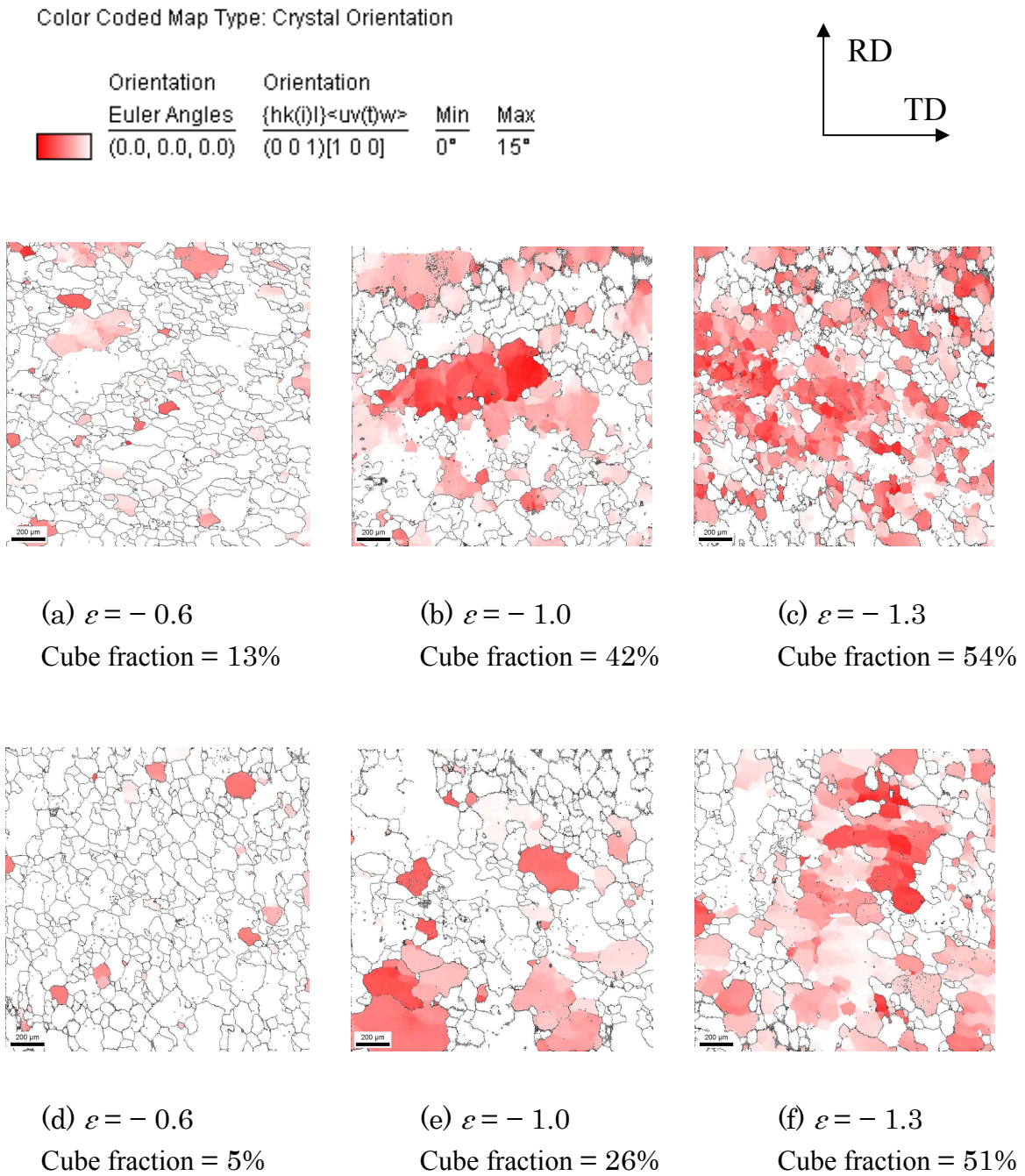


Fig. 5.7 Area fractions of cube ( $\{001\}\langle 100 \rangle$ ) orientation of AA5182 derived from EBSD after plane strain compression at 823 K and strain rates of (a)–(c)  $5.0 \times 10^{-3} \text{ s}^{-1}$  and (d)–(f)  $5.0 \times 10^{-4} \text{ s}^{-1}$  up to true strains of  $-0.6$ ,  $-1.0$ , and  $-1.3$ . Black lines represent high-angle grain boundaries with misorientation angles ( $\theta$ ) of greater than  $15^\circ$ .

## 5. Effect of Texture on the Bending Workability of AA5182 Alloy

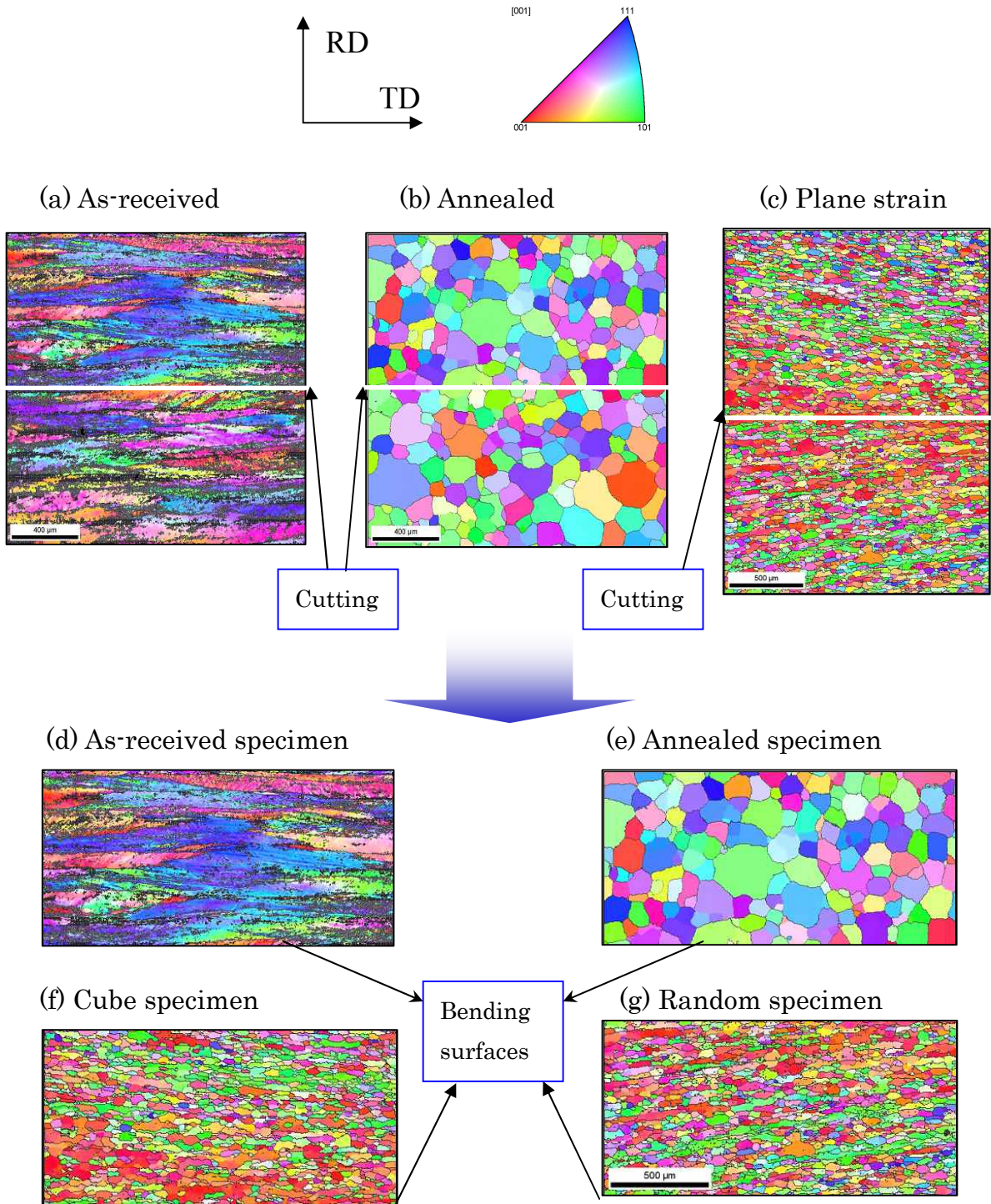


Fig. 5.8 Grain structure maps for the TD plane obtained by EBSD: (a) as-received specimen, (b) annealed specimen, and (c) specimen plane strain compressed at 823 K and a strain rate of  $5.0 \times 10^{-3} \text{ s}^{-1}$  up to a true strain of  $-1.3$ . White lines represent cutting planes. Bottom planes of (d)–(g) are the bending surfaces.

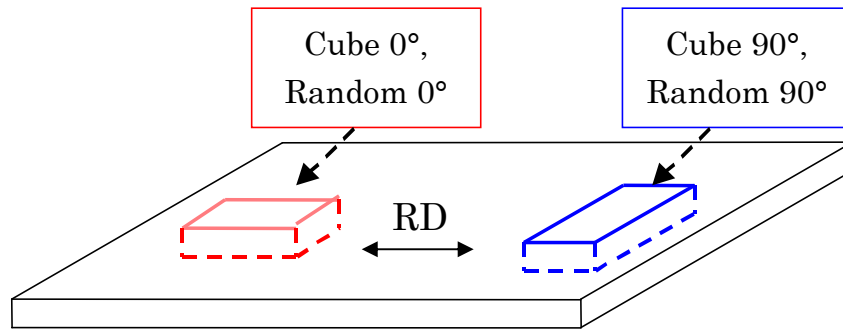


Fig. 5.9 Schematic view of method of preparing bending test specimens labeled cube 0°, random 0°, cube 90°, and random 90° specimens.

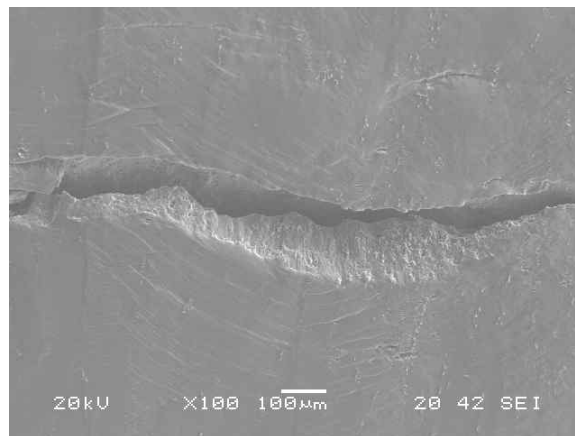
### 5.3.4 Microstructures of the bent surfaces

Figure 5.10 shows micrographs of the surfaces of the (a) as-received, (b) annealed, and (c) cube 0° specimens after a 90° bending test. Cracks appear on the bent surface in Fig. 5.10(a) but not on those in Fig. 5.10(b) and 5.10(c). Figure 5.11 shows micrographs of the surfaces of the (a) cube 0° specimen, (b) cube 90° specimen, (c) random 0° specimen, (d) random 90° specimen, and (e) annealed specimen after a 120° bending test. The cube 0° specimen exhibits the highest bendability among all the specimens, although large and/or small cracks appear on the bent surfaces.

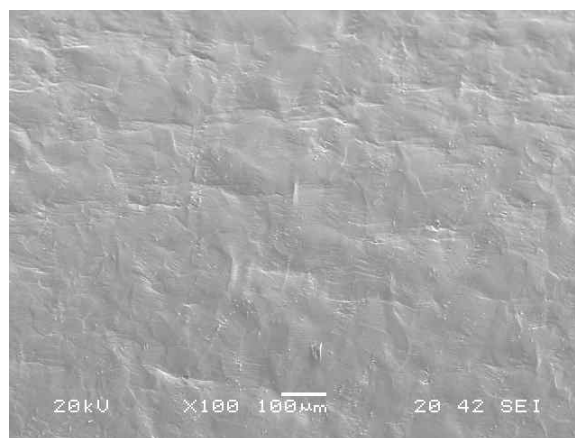
## 5. Effect of Texture on the Bending Workability of AA5182 Alloy

---

(a) As-received specimen



(b) Annealed specimen



(c) Cube 0° specimen

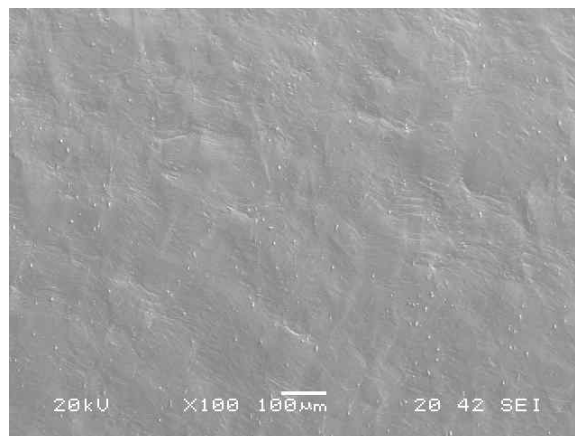
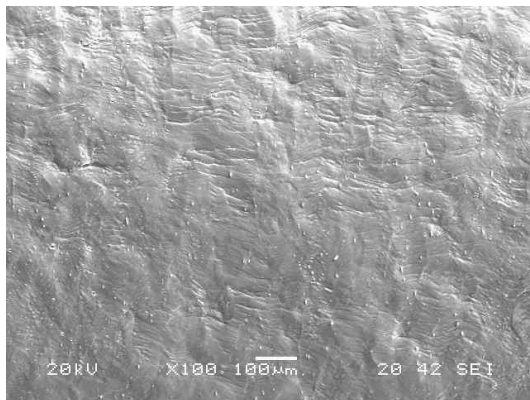


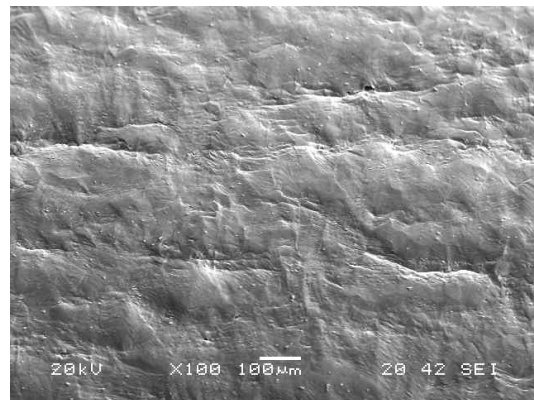
Fig. 5.10 Micrographs of surfaces of (a) as-received, (b) annealed, and (c) cube 0° specimens after 90° bending test.

## 5. Effect of Texture on the Bending Workability of AA5182 Alloy

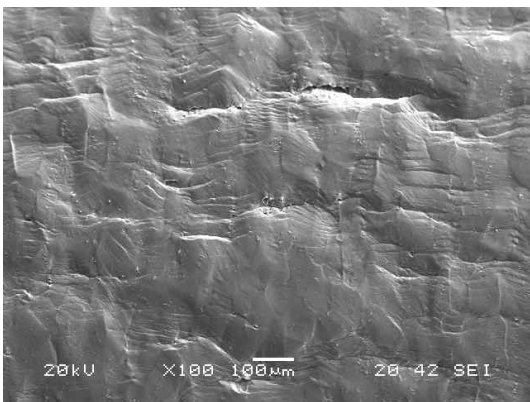
(a) Cube 0° specimen



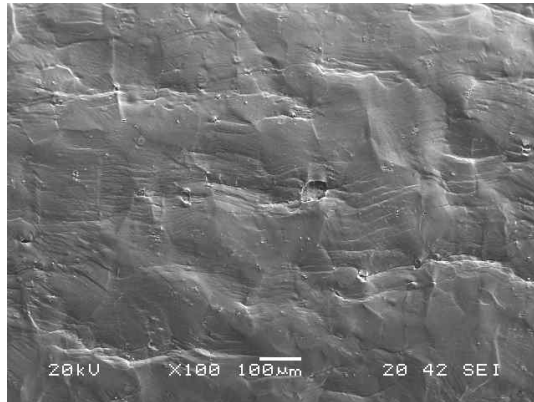
(b) Cube 90° specimen



(c) Random 0° specimen



(d) Random 90° specimen



(e) Annealed specimen

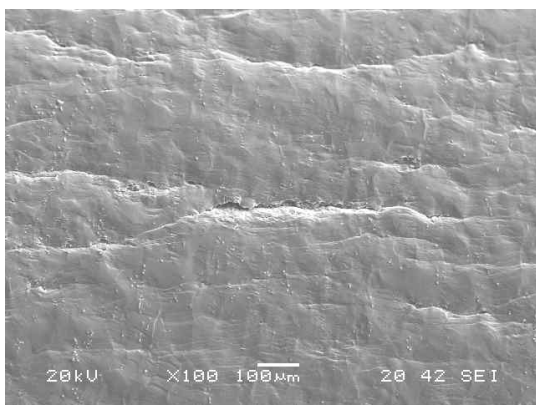


Fig. 5.11 Micrographs of surface of (a) cube 0° specimen, (b) cube 90° specimen, (c) random 0° specimen, (d) random 90° specimen, and (e) annealed specimen after 120° bending test.

### 5.4 Discussion

#### 5.4.1 Relationship between texture and bend workability

As described in chapters 3 and 4, an examination of the relationship between high-temperature uniaxial compression and texture formation in commercial aluminum alloys showed that  $\{001\}$  and/or  $\{011\}$  texture can be controlled by changing the temperature, strain rate, and strain. For AA5052 and AA5182 alloys, higher temperatures produce sharper  $\{001\}$  texture under the same flow stress. In AA5182, the highest pole density at (001) appears at 823 K and a true strain rate of  $5.0 \times 10^{-3} \text{ s}^{-1}$ . On the basis of this result, plane strain compression under these conditions was conducted to clarify the effect of the deformation mode on texture formation. The pole density at (001) was 10 times the random level for the specimen deformed up to a strain of  $-1.3$ , as shown in Fig. 5.3(c). In this case, the  $\varphi_2$  cross sections, shown in Fig. 5.5, show that the main component of texture is  $\{001\}\langle 100 \rangle$  (cube orientation). The cube fraction in this case is higher than that obtained under the other deformation conditions, as shown in Fig. 5.7.

Takeda et al. [1] investigated the relationship between the crystal orientation and bendability of Al–Mg–Si alloys by using single crystal specimens having various orientations. They found that cube and/or cube-rotated specimens have higher bendability. In the results of a  $90^\circ$  bending test given in Fig. 5.10, the cube  $0^\circ$  specimen shows the highest bendability, which coincides with the experimental results reported by Takeda et al. [1].

The relationship between the bendability and the formation of shear bands has been reported [1,2,4,5]. Shear bands did not form in the cube  $0^\circ$  specimen during the bending test, although some shear bands formed in the specimens with other orientations. Thus, the formation of shear bands can be suppressed by controlling the orientation. This suggests that the bendability of AA5182 can be improved by developing cube texture, as shown in Fig. 5.11.



5.4.2 Effect of grain structure on bendability

A comparison of Fig. 5.11(a) and 5.11(b) shows that the highest bendability appears in the cube  $0^\circ$  specimen [Fig. 5.11(a)]. Thus, the grain structure affects the bendability. Figure 5.7(c) shows that grains of cube texture are connected with each other grains. Figure 5.12(a) and (b) show schematic views of the cube  $0^\circ$  and cube  $90^\circ$  specimens, respectively, used in the bending test. As described in section 5.4.1, no shear bands appeared in the cube  $0^\circ$  specimen during the bending test. This suggests that the cube  $0^\circ$  specimen has higher bendability than the cube  $90^\circ$  specimen, because the shear bend in the former is more affected by the bending test than that in cube  $90^\circ$ .

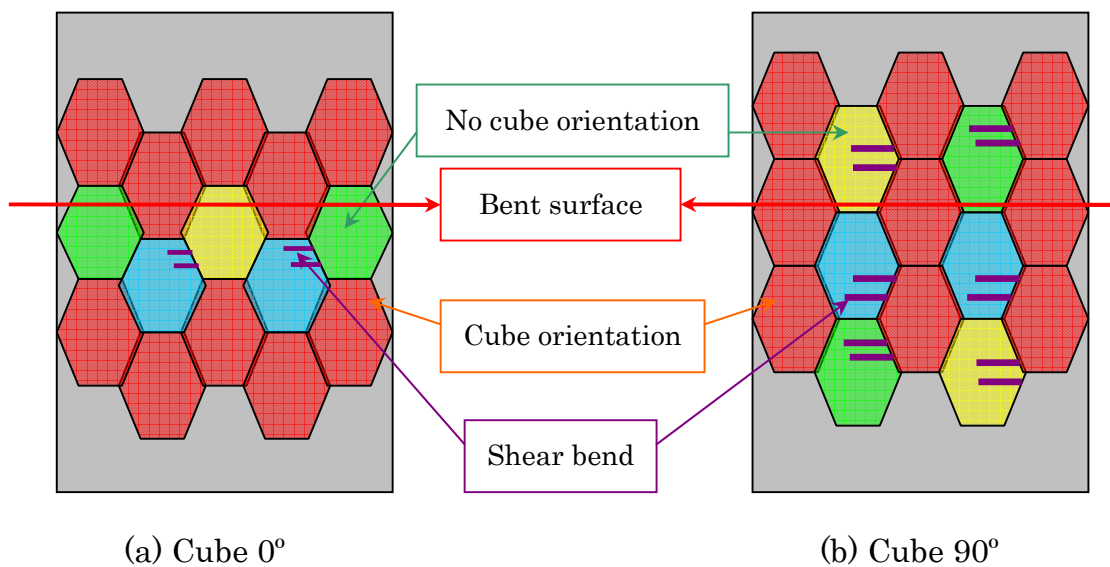


Fig. 5.12 Schematic view of bending test. Bold red line represents the bent surface. Red areas indicate grains with cube orientation; other colors indicate grains with other orientations. Purple line represents the shear band.

### 5.5 Conclusions

The relationship between bend workability and texture was experimentally investigated for AA5182 alloy. The major results are summarized as follows.

- (1) Cube texture develops in AA5182 alloy by plane strain compression under specific uniaxial compression deformation conditions
- (2) In AA5182 alloy, higher bendability appears in specimens having cube orientation. This suggests that the workability of commercial aluminum alloy can be improved by controlling the texture.
- (3) The shape of the grain structure affects the bending workability.

## References

- [1] H. Takeda, A. Hibino and K. Takata: Mater. Trans. **51 No.4** (2010) pp.614-619.
- [2] A. Hibino, T. Muramatsu, M. Saga and K. Takata: J. JILM **53** (2003) pp.534-541.
- [3] A. Hibino, T. Muramatsu, T. Komatsubara, M. Saga and K. Takata: Abstracts of the 106th Conference of the Japan Institute of Light Metals (2004) pp.89-90.
- [4] M. Asano, T. Minoda, Y. Ozeki and H. Yoshida: Mater. Sci. Forum **519-521** (2006) pp.771-776.
- [5] M. Saga, M. Kikuchi, Y. Zhu and M. Matsuo: Proc. 6th Int. Conf. On Aluminum Alloys (1998) pp. 425-430.

## Chapter 6

### Conclusions

## 6. Conclusions

---

Chapter 1 describes the importance of aluminum alloys and their deformation mechanisms. The importance of controlling {001} (cube) texture, which has been realized in binary Al–Mg alloys, in commercial aluminum alloys is also described.

The experimental procedure is described in chapter 2. The reliability of the experiments is confirmed by specifying the details of the uniaxial and plane strain compressive deformations. The EBSD measurement technique, which can be used to determine the space distribution of localized grain orientations, and the X-ray measurement technique are also introduced.

In chapter 3, the high-temperature deformation mechanism and texture formation process in AA5182 commercial aluminum alloy [1,2] are investigated. To understand the high-temperature deformation mechanism of AA5182, the texture formation process is studied experimentally by comparison with previous results for binary Al–5mass%Mg alloy.

For Al–Mg binary alloys, earlier research clearly verified that the stress exponent  $n$ , which is derived from the stress–strain curves, suggests two deformation mechanisms. One is dominated by viscous dislocation motion, which is realized by motion with the Cottrell atmosphere in a certain range of high-temperature deformation conditions. In the other, free flight dislocation motion dominates. These deformation mechanisms and the development of {001} texture are discussed using {001} texture maps. These maps, which provide information regarding texture control and the effect of grain boundary migration, are the main result of this chapter. The major findings are as follows.

- A transition in texture from {011} (compression plane) to {001} with increasing strain also occurs in AA5182. The texture in AA5182, however, is much weaker than that for a binary alloy with a similar Mg content under the same deformation conditions.
- The mean size of grains with the {001} orientation is much larger than that of all grains under the deformation conditions yielding sharp {001} texture. This indicates that the formation of {001} texture after a large amount of strain should be attributed to grain boundary migration.
- The sharpness of the {001} component cannot be given simply as a function of temperature or strain rate. To better understand the texture formation process, the {001} texture map is proposed. In this map, the texture sharpness of the {001} component is given by contours within the temperature–strain rate field with additional contours for flow stresses. The texture map facilitates

## 6. Conclusions

---

identification of the process conditions necessary for texture control.

- An examination of the  $\{001\}$  texture map reveals that higher temperatures yield a sharper  $\{001\}$  texture at the same flow stress. This also suggests the key role of grain boundary migration in the development of  $\{001\}$  texture.

AA5052 alloy contains a Mg concentration of close to 2.6mass%. To clarify the applicable range of texture-controlling techniques for commercial aluminum alloys, the texture formation process in AA5052 was examined by means of uniaxial and plane strain compression at high temperatures. Chapter 4 presents the results [3]. As mentioned above, the  $\{001\}$  fiber texture is deformed by grain boundary migration; however, unlike binary aluminum alloys, commercial aluminum alloys contain particles that suppress grain boundary migration. Hence, it is necessary to verify whether the texture is controllable at limited high temperatures. The effect of temperature, strain rate, and solute concentration on texture formation in commercial aluminum alloys is discussed using the  $\{001\}$  texture map. The major results are summarized as follows.

- The main component of the fiber texture depends on the deformation conditions in these commercial alloys.
- When  $\{001\}$  texture develops, the mean grain size for  $\{001\}$  grains is larger than that for all grains in both alloys. This suggests that  $\{001\}$  texture formation is due to grain boundary migration.
- The pole densities at (001) in the present alloys are much weaker than those of binary alloys with similar solute concentrations under the same deformation conditions. This might be attributable to the suppression of grain boundary migration.
- For the same deformation conditions, the pole densities at  $\{001\}$  in AA5182 are higher than those in AA5052 alloy.

Chapter 5 presents the relationship between texture and bending workability. The bending workability of AA5182 alloy is improved when cube texture exists in the surface. The effect of the deformation mode on texture formation is also discussed. The major results are summarized as follows.

- Cube texture develops in AA5182 alloy by plane strain compression under specific uniaxial compression deformation conditions.
- In AA5182 alloy, specimens having cube orientation exhibit higher bendability.

## 6. Conclusions

---

This suggests that the workability of commercial aluminum alloy can be improved by controlling the texture.

- The shape of the grain structure affects the bending workability.

## References

- [1] H-M. Jeong, K. Okayasu and H. Fukotomi: *Proceedings of the 4th International Conference on Recrystallization and Grain Growth (ReX & GG 4-2010)*, Sheffield, UK (2010) in press (6 pp).
- [2] H-M. Jeong, K. Okayasu and H. Fukotomi: *Mater. Trans.* **51(12)** (2010) pp. 2162–2167.
- [3] H-M. Jeong, K. Okayasu and H. Fukotomi: *Proceedings of the 12th International Conference on Aluminum Alloys (ICAA12)*, Yokohama, Japan (2010) The Japan Institute of Light Metals, pp. 125–130.

## Acknowledgements

I'm grateful to Professor Hiroshi Fukutomi for offering me the possibility to carry out my research and for his guidance and support. I also want to thank my instructors Kazuto Okayasu and Prof. Makoto Hasegawa for the guidance they have given me, as well as the pre-examiners of this thesis. I am also grateful my room mates at the Fukutomi Laboratory. I also want to thank 박규협 박사님 and 정영관 교수님 for supporting me the studying abroad in Japan.

Finally, I want to thank my parents, my brother, and my wife for their important support that helped me to get to this point.



# Appendix

## Appendix A

### Appendix A: Classification of commercial Aluminum Alloys

The examination of microstructure by optical microscopy is the primary method of evaluating alloys. It will show the effects of processing, heat treatment, fabrication, and service conditions. Examination of the microstructure is also for examination of service failures. Metallography is a simple cost-effective method to gather information about prior thermal history.

In general, the metallographic examination is accomplished by gradually increasing the magnification until the desired feature is found. At higher magnifications, it is necessary that the quality of the metallographic mount be increased. This is because at higher magnifications, the field of view and depth of field become limited.

Light microscopy is the most widely used method of examining microstructures. Generally it is useful to approximately 1500 magnification. Features greater than 0.1 mm can be resolved. This resolution shows the size and distribution of precipitates and second-phase particles. It will also show grain size and orientation.

However, light microscopy will not resolve the fine precipitates that occur during precipitation hardening. It will also not show dislocations. With special metallographic techniques and etching practice, the presence of dislocations can be inferred. To see the fine precipitates and dislocations, it is necessary to use a transmission electron microscope (TEM).

The identification of phases present in a microstructure is important. The phases present typically result from nonequilibrium conditions. They are related to the phase diagram for most conditions. This could be from casting, brazing, welding, heat-treating, or mechanical working. Generally, the composition and crystallography of a phase has already been predetermined. However, if the phase has not been previously identified, it can be identified using x-ray diffraction, microprobe, TEM, and electron diffraction or electron backscatter diffraction (EBSD) can be used for precise identification.

## Appendix A

Table A.1 Classification system for wrought aluminum alloys

Alloy	Major Constituents
1XXX	> 99% Al
2XXX	Al – Cu
3XXX	Al – Mn
4XXX	Al – Si
5XXX	Al – Mg
6XXX	Al – Mg – Si
7XXX	Al – Zn – Mg – (Cu)
8XXX	The other element (Ex, Al – Li)

Wrought and cast aluminum alloys are classified according to the alloy content. Table A.1 shows the method in which wrought alloys are classified, and Table A.2 shows the classification system for cast aluminum alloys. Because of the analogs between wrought and cast alloys, the microstructure is described for the wrought systems.

### A.1 1XXX series alloys (>99% Al)

1XXX series aluminum alloys are generally commercially pure aluminum. They are not heat treatable. It is not possible to completely eliminate iron and silicon. Fe and Si solubility is low in aluminum, so these Al-Fe and Al-Fe-Si intermetallics precipitate out of solution. In general, the volume fraction of second-phase particles is in direct relation to the amount of Fe present as a contaminant. Typically the precipitates are  $\text{FeAl}_3$ ,  $\text{Fe}_3\text{SiAl}_{12}$ ,  $\text{Fe}_2\text{Si}_2\text{Al}_9$ .

## Appendix A

Table A.2 Classification system for cast aluminum alloys

Alloy	Major Constituents
1XXX	> 99% Al
2XXX	Al – Cu
3XXX	Al – Si – Mg Al – Si – Cu Al – Si – Mg – Cu
4XXX	Al – Si
5XXX	Al – Mg
7XXX	Al – Zn – Mg – (Cu)
8XXX	Al – Sn
9XXX	The other element

### A.2 2XXX series alloys (Al – Cu)

The 2XXX Al-Cu alloys are commonly used for many applications. Generally complex additions of Mg, Mn, or other alloy additions are added for strength, or corrosion resistance. Copper is the primary alloying addition, as is present in the alloy as  $\text{Al}_2\text{CuMg}$  (if Mg is present) or  $\text{Al}_2\text{Cu}$ . Iron rich precipitates  $\text{Al}_7\text{Cu}_2\text{Fe}$  and  $(\text{Mn, Fe})_3\text{SiAl}_{12}$  are generally the only iron phases present.  $\text{Al}_7\text{Cu}_2\text{Fe}$  is the most common.

Because of the alloying content, it is necessary to heat treat these alloys close to the equilibrium solidus temperature. This results in a greater tendency to overheat, and cause incipient melting at the grain boundaries.

## Appendix A

### A.3 3XXX series alloys (Al – Mn)

Essentially, these alloys are 1100 series aluminum alloys, with Mn added. These alloys are typically used in the manufacture of automotive aluminum radiators. Mn segregates to the center of dendrite arms. If the amount of manganese is sufficiently high to cause super-saturation, then the precipitation of a manganese rich phase occurs and forms a dispersoid. This is typically  $(\text{Mn, Fe})\text{Al}_6$ . However, depending on the alloying content, another phase that can occur (although not at the center of the dendrite arms) is  $(\text{Mn, Fe})_3\text{SiAl}_{12}$ .

### A.4 4XXX series alloys (Al – Si)

These alloys are used in architectural applications and forged pistons. Because of the silicon content, it is often used as a welding, brazing, or filler alloy. The as-cast phases are Si and a solid solution of Al-Si. Iron, present as a contaminant, appears as  $\text{Fe}_2\text{Si}_2\text{Al}_9$ . These phases are shown in microstructures as needles. During homogenization, the silicon precipitates will round and coalesce. The iron-rich precipitates remain as needles.

### A.5 5XXX series alloys (Al – Mg)

The 5XXX series aluminum alloys have been used for cryogenic tanks, tractor-trailers, and armor applications. It is readily welded and shows good corrosion resistance. This alloy is non-heat-treatable.

The primary alloying addition is Mg. Mg shows a high solubility in aluminum. When the magnesium content is greater than 3.5%, the excess magnesium precipitates as  $\text{Mg}_5\text{Al}_8$ . Cr is also a common additive, and appears as a fine dispersoid of  $\text{Cr}_2\text{Mg}_3\text{Al}_{18}$ .

### A.6 6XXX series alloys (Al – Mg – Si)

This alloy system is also very commonly used. It is readily heat-treated, and shows good quench sensitivity. It is precipitate hardened using  $\text{Mg}_2\text{Si}$  as the hardening precipitate. If there is a low alloy concentration of Mg and Si, then all the  $\text{Mg}_2\text{Si}$  can be dissolved during solution heat treatment and used in the precipitation hardening reaction. But if there is excess Mg and Si, then the excess  $\text{Mg}_2\text{Si}$  will precipitate as  $\text{Mg}_2\text{Si}$  in a distinctive Widmanstätten pattern. Because the precipitates utilized to achieve hardening are so small, it is generally not

## Appendix A

possible to distinguish between the T4 and T6 tempers. Hardness and conductivity is usually the best method.

The iron-rich phases are  $\text{Fe}_3\text{SiAl}_{12}$  or  $\text{Fe}_2\text{Si}_2\text{Al}_9$ . If Mn and Cr are present, then  $\text{Fe}_3\text{SiAl}_{12}$  is stabilized.

### A.7 7XXX series alloys (Al – Zn – Mg)

The wrought alloy systems of Al-Zn-Mg, with additions of Cu, comprise the most common aluminum alloys used in aerospace. This alloy system offers the best combination of strength, fracture toughness, and corrosion resistance of any other aluminum system. It is readily heat-treated, without the strict precautions of solution heat-treating temperature causing eutectic melting.

The equilibrium phases in the Al-Mg-Zn alloys are  $\text{MgZn}_2$  ( $\eta$ ),  $\text{Mg}_3\text{Zn}_3\text{Al}_2$  (T) and  $\text{Mg}_5\text{Al}_3$  ( $\beta$ ). If the quantity of Zn<sub>4</sub>Mg, than the precipitation sequence to equilibrium  $\text{MgZn}_2$  is predominant. If there is more Mg than Zn, than the sequence to the equilibrium precipitate  $\text{Mg}_3\text{Zn}_3\text{Al}_2$  (T) predominates. If Cu is added, the order of alloying element quantity is generally Zn<sub>4</sub>Mg<sub>4</sub>Cu. If Cu<sub>4</sub>Mg, then the sequence to the S phase ( $\text{Al}_2\text{CuMg}$ ) predominates.

The iron-rich phase is typically  $\text{Fe}_3\text{SiAl}_{12}$  in homogenized structures, and  $\text{Al}_7\text{Cu}_2\text{Fe}$  in as-cast structures. If Cr is present, it forms a fine dispersoid that hinders recrystallization during hot-working. Other dispersoids such as Zr are also used to increase the recrystallization temperature.